NASA Contractor Report 178156 -- Volume I

(NASA-CR-178156) VISCOUS WING THEORY DEVELOPMENT. VOLUME 1: ANALYSIS, METHOD AND RESULTS Final Report (Grumman Aerospace Corp.) 127 p CSCL 01A

N87-10043

Unclas
G3/02 44358

Viscous Wing Theory Development, Volume I -- Analysis, Method, and Results

R.R. Chow, R.E. Melnik, F. Marconi, J. Steinhoff

Grumman Corporate Research Center

Bethpage, NY 11714-3580

Contract NAS1-16858

October 1986

National Aeronautics and
Space Administration

Langley Research Center
Hampton, Virginia 23665-5225

REPORT RE-725

VISCOUS WING THEORY DEVELOPMENT
VOLUME I - ANALYSIS, METHOD AND RESULTS

OCTOBER 1986

prepared by

R.R. Chow, R.E. Melnik, F. Marconi, J. Steinhoff
Fluid Mechanics Directorate

Grumman Corporate Research Center
Bethpage, New York 11714-3580

Final Report on Contract No. NAS1-16858

prepared for

Langley Research Center
National Aeronautics and Space Administration
Hampton, Virginia 23665-5225

Approved by: Richard A. Schuing, V.P.
Director, R&D Center

CONTENTS

CONTENTS (contd)

ILLUSTRATIONS

TABLES

1. SUMMARY

In this report, we have described a method for the computation of viscous transonic flows over 3-D wings using a zonal approach to treat the viscid-inviscid interactions. The chord Reynolds number was considered large and the boundary layer was assumed to be predominantly turbulent. For the inviscid flow computation, a parabolic coordinate mapping was used in conjunction with a finite volume formulation of the conservative full potential equation. A new numerical-AFZ scheme was developed for the 3-D inviscid flow solution to replace the SLOR scheme. A special far field asymptotic boundary condition was derived that gave more accurate results and better convergence performance. In addition, a second order artificial viscosity is used in the supersonic zone rendering the computation formally second-order everywhere except at the captured shocks. For the 3-D boundary layer calculation, the integral method of Myring-Smith-Stock was extensively modified and made suitable for our interaction calculation. The wing thickness effect was taken into account and the viscous wake solution was computed beyond the trailing edges. The interaction calculation was formulated with a set of coupling conditions that included the proper source flux distribution due to the surface boundary layers on the wing, the flux jump distribution due to the viscous wake and the viscous wake curvature effect. Transpiration boundary conditions were used for the inviscid flow boundary conditions for the coupled calculations. In addition, a method was devised so that the results of the trailing edge strong interaction solution in our 2-D viscous airfoil analysis could be adapted for the normal pressure correction near the trailing edge region. The wake surface (that is, a fictitious surface imbedded in the viscous wake) was floated such that the converged solution coincides with the inviscid flow stream surface. A computer program was written to perform calculations including all the above mentioned effects in a fully automated manner. A standard case of calculation is represented by data inputs of wing geometry, section ordinates, freestream Mach number, angle of attack and mean chord Reynolds number. Three versions of the source language code of the computer program were prepared. One scalar version is to be used on the IBM-3081 computer, and two vectorized versions are to be used for the computers Cyber-205 and Cray-1S. For engineering requirements, a typical case of

calculation for a viscous solution usually takes about 5 minutes of CPU computing time on a Cray-1S computer. Details of the program can be found in Volume 2 of this report - "GRUMWING User's Manual". The viscous program has been test run on the Lockheed Wing A - a transonic supercritical transport wing, and on the Lockheed Wing B - a high subsonic cruise fighter wing. In addition, many check calculations have been carried out with the basic AFZ inviscid code. These include computations over an ONERA-M6 wing modified to include a large degree of wing twist, and calculations for a more complex swept wing designed at Grumman Aerospace Corporation.

2. INTRODUCTION

There has been steady progress in the computation of inviscid transonic flows in the decade following the original contribution of Murman and Cole in 1971. Recent developments (reviewed in Ref. 1-3) have led to fast, reliable and accurate methods for solving the full potential flow equation using ADI and multigrid techniques for transonic flows over airfoils, wings and relatively complex wing-body combinations. Major advances have also been made in the solution of the full Euler equations using multigrid and Runge-Kutta techniques. The availability of these codes coupled with advances in computers has revolutionized the aerodynamic design process so that computational methods currently have a central role in aerodynamic design.

It is of course well known that viscous effects are important in most aerodynamic flows of interest, particularly at transonic speeds, and must be included in the theoretical formulation to be useful for practical design applications. Recent applications of inviscid codes to transonic wing design reported in the papers of Ref. 4 showed the inadequacies of purely inviscid methods for practical wing design at transonic speeds. At the high Reynolds numbers of interest in most aerodynamic problems the flow field is essentially inviscid with viscous effects confined to thin layers near the surface and in the wake. In these problems viscous effects can be taken into account through a zonal approach based on an iterative solution of the combined inviscid and boundary layer equations, including other local regions of strong viscid-inviscid iteration where necessary. An alternative approach is that of directly solving the full or parabolized approximation of the Reynolds averaged equations numerically. While offering the prospect of providing the most accurate and general method for solving viscous flow problems, Navier-Stokes solvers have not yet led to a practical methods for aerodynamic design. This is due to the Navier-Stokes solver's large computing requirements and expense and the inadequacies of the turbulence models available for finite difference formulations. In contrast, zonal type methods have proved practical for aerodynamic design, particularly when simple integral methods are used for the boundary layer solution. Integral methods are attractive for viscid-inviscid interaction calculations not only because they greatly reduce the computing requirements but also because they are much

more flexible than finite difference methods in adapting turbulence models to fit the physics in various subregions of complex turbulent flows (see discussion by Kline in Ref. 5). Such methods have proved particularly effective for computing viscous transonic flow over airfoils and are widely used throughout the aeronautical community.

The objective of the present work is to develop a zonal type method for viscous transonic flow over 3-D wings. Our approach is to apply the same viscous/inviscid interaction techniques previously developed for our GRUMFOIL code (Ref. 6,7) for airfoils.

In a zonal type approach the flow is divided into an outer inviscid region and thin, inner viscous regions near the airfoil and wake. The viscous layers are further subdivided into weak interaction zones comprising most of the boundary layer and wake where the standard boundary layer equations apply and small local strong interaction regions near shock waves and the trailing edge where the boundary layer approximations breaks down due to the presence of relatively large normal pressure gradients. The viscous effects on the outer inviscid flow are accounted for through viscous coupling conditions that appear as boundary conditions on the inviscid flow. The ultimate basis for a zonal type approach is a large Reynolds number asymptotic limit. To be complete in the sense of including all the leading order terms the matching conditions should account for 1) displacement effects on the airfoil or wing, 2) displacement effects due to the wake and 3) wake curvature effects due to the momentum defect across the wake and 4) normal pressure gradient effects in the strong interaction zones at trailing edges and shock waves.

Nearly complete zonal type methods have recently been developed for subsonic and transonic flow over airfoils by Melnik (Ref. 6-8) et al, Collyer and Lock (Ref. 9), and LeBalleur (Ref. 10). All these methods employed a potential flow approximation for the inviscid flow and integral methods for the boundary layer solution. They accounted for all the weak interaction effects due to the boundary layer and wake but only the GRUMFOIL code of Melnik et al accounted for strong interaction effects at the trailing edge. None of the methods accounted for strong interaction effects near shock waves.

In turbulent flow, the shock wave penetrates into the boundary layer and generates large normal pressure gradients leading to a breakdown of the standard boundary layer formulation. Although a simple boundary layer

description cannot give an accurate prediction of the local details of such an interaction, comparison with experiments (Ref. 6, 8, and 11) indicates that it does seem to give a good prediction of the overall thickening of the boundary layer across the shock wave and a good prediction of the boundary layer integral properties downstream of the interaction. Fortunately, this seems to be sufficient to achieve good predictions of airfoil section characteristics even under high-lift supercritical conditions. On the other hand, because normal pressure gradient effects near trailing edges can produce significant global results through their influence on the Kutta condition, they should be accounted for, particularly when there is a significant degree of rear loading on the airfoil.

A similar method was developed by Whitfield et al (Ref. 11 and 12) using an Euler equation solver for the inviscid flow. Their method only accounted for the displacement effect of the boundary layer and wake and ignored the wake curvature and strong interaction effects. Although the use of the Euler equations for the inviscid solution might be an improvement for strong shock waves ($M_{LOCAL} > 1.3$), the overall method may be less accurate than the potential flow methods discussed above because of the neglect of the wake curvature and trailing edge interaction effects in their viscous flow formulation. For further discussion of developments in zonal methods for airfoils see the recent reviews in Ref. 10 and Ref. 12-15.

Our overall approach to the wing problem addressed in this report has been to extend the viscous flow formulation used in the GRUMFOIL code for airfoils to three dimensions. For the inviscid flow, the full potential equation for transonic flow over 3-D wings is employed. A finite volume formulation based on Jameson's FL027 code was used to solve the full potential equation in conservation form. A modified "C" type mesh was employed to allow the wake streamline to be aligned with the grid thus giving a more accurate implementation of wake coupling conditions than used in the 2-D GRUMFOIL code. A new approximate factorization (AFZ) scheme was formulated to accelerate convergence. We also introduced a more accurate asymptotic far field boundary condition and a fully second order artificial viscosity into the program. The inviscid code is designated FL047. The new laminar and turbulent boundary layer method used in the present work has its origin in Stock's method (Ref. 16) but has been extensively modified for interactive

calculations. Stock's method uses a fully 3-D integral boundary layer method with a lag entrainment method adopted from the work of Green (Ref. 17).

The viscous flow method employs a fully 3-D form of the wing surface boundary layer and wake displacement thickness coupling conditions using a transpiration velocity formulation. The wake curvature condition is implemented using a quasi-2-D strip formulation that accounts only for the pressure variation across the wake that is generated by the streamwise component of the curvature of the wake surface. This approximation should be useful for the wing flow field under consideration where the primary component of the wake curvature is in the streamwise direction. The spanwise component of curvature can be expected to be large only near the wing tip, and it is only in this region that we showed significant departures from the simple strip approximation employed in the present method. We also employ a simple 2-D strip approximation to justify the use of the same trailing edge correction as employed in the GRUMFOIL code. Since gradients in the spanwise direction are small compared to the gradients in the streamwise direction, this should also be a good approximation except near the wing tip and root sections. With these approximations, the present code accounts for all the primary viscous interaction aspects except those arising from the shock boundary layer interaction. As proved for the airfoil calculations we expect this simple boundary layer treatment of shock wave-boundary layer interactions to be adequate for the prediction of wing section characteristics for the reasons discussed above.

Several other methods have recently been developed (Ref. 18-22) for computing viscous transonic flow over wings and wing-body combinations. In common with the present method, they all employ a modified version of Green's lag entrainment method for the boundary layer solution and all, except Samant and Wigton (Ref. 22), use a potential flow approximation for the inviscid flow. Samant and Wigton (Ref. 22) use the Jameson FL057 (Ref. 23) method for solving the full Euler equations in the inviscid flow. Firmin (Ref. 18) and Waggoner (Ref. 19) use a transonic small disturbance approach for the inviscid flow which is less accurate than the full potential flow approximation employed in the present method as well as in Streett's (Ref. 20) and Wigton and Yoshihara's (Ref. 21) method. All of the methods, including the present one, account for the displacement thickness effect both on the wing surface

and in the wake, except for Waggoner's and Samant and Wigton's methods which neglect all wake effects. Only Streett's and the present method account for the wake curvature effect and only the present method includes the trailing edge interaction effect. The corrections to the coupling conditions that arise from the local trailing edge interaction solution are particularly important for a correct implementation of the wake curvature effect. The procedure used for the wake curvature terms in Streett's method, which ignores the trailing edge interaction, employs a single mean of the curvatures of the upper and lower surfaces of the wake. This undoubtedly leads to a significant underestimate of the wake curvature effect. Nevertheless, computations presented in Streett's paper indicated that the effect of the wake curvature coupling conditions were fairly large. These results and those obtained earlier for airfoils (Ref. 8) clearly demonstrated the importance of including the wake curvature terms in the coupling conditions.

We believe the viscous flow method employed in the present work represents the most complete implementation of a zonal type approach to viscous flow over wings achieved to date.

Acknowledgement. The authors wish to express their appreciation to Mr. D. Roman for his contributions to the development of the inviscid portion of the computer program used in this work.

3. VISCOUS WING THEORY - BACKGROUND

3.1 INTRODUCTORY REMARKS - INVISCID FLOW

In the last few years, extensive progress has been made in inviscid transonic flow computations. Three dimensional transonic, inviscid flow fields can now be computed over wings and wing-fuselage combinations using newly developed "finite volume" computer codes which solve the transonic full potential equations. For cases where the shocks are not so strong that extensive boundary layer separation or entropy production at the shock takes place, accurate predictions of lift and drag can be obtained (Ref. 24). Just as important as accuracy, these finite volume techniques are flexible, being able to handle fairly complex geometries, and can be matched to turbulent boundary layer computing methods as reported here and in Ref. 20.

In Subsection 4.1, we describe a simple but efficient "AFZ" approximate factorization scheme which can converge to a solution much faster than relaxation methods. The scheme requires no more computer storage than relaxation schemes, however, and, as is in those schemes, data is only required in a fixed plane-by-plane sequence. Therefore, if necessary, a disk or similar mass storage device can efficiently be used.

Other factorization schemes have been reported for the 3-D transonic problem (Ref. 25, 26, and 27). In Ref. 25, two 3-D data arrays must be stored, however, and more complicated data manipulations are required due to the presence of an additional factor. The "SIP" scheme of Ref. 26 requires much more storage and data manipulations. The scheme of Ref. 27 is applied to a nonconservative finite difference scheme, rather than a finite volume one. In our work, the AFZ scheme is applied to the 3-D conservative, full potential, finite volume formulation of Ref. 24.

Another approach to solving the inviscid equations involves using a factorized or a relaxation method for reducing high frequency errors, together with a multigrid scheme. Good results, comparable to ours, in terms of convergence rates, have been presented in Ref. 28 and 29 for successive line over relaxation (SLOR) with multigrid. These schemes require about 30% more total storage than ours due to the extra grids used. Also, the use of auxiliary storage such as a disk appears to be more difficult due to the

required intergrid transfer operations. However, multigrid methods may be less sensitive to extreme grid stretching than our method.

An alternative to solving the potential equations for the inviscid flow involves the Euler equations. These require, however, at least five times as much storage and several times as many computations per point per iteration as potential flow methods. Also, although recent progress has been made on speeding up convergence (Ref. 30), they require at least several times as many iterations to converge and almost an order of magnitude more total computational cost.

Some of the initial work on the AFZ method was done with J. Benek and A. Jameson (Ref. 31).

3.2 3-D BOUNDARY LAYER & VISCOUS WAKE THEORY

The subject of 3-D boundary layers is a very large and important area of research in aerodynamics. It has been of continued interest to aerodynamicists for the past several decades. Examples of recent developments can be found in the book "Three-Dimensional Turbulent Boundary Layers" (Ref. 35). Significant progress has been made on computing attached 3-D boundary layers solution on wings. Although 3-D boundary layer separation remains a very difficult problem to solve, the phenomenon has become much better understood through the study of the development of the characteristics of the system of partial differential equations for boundary layers (Ref. 36 and 37). The study of boundary layer separation on wings is particularly important in the transonic flow regime as it is very often caused by the interaction with the inviscid shocks on the upper surface of the wings.

Methods of solving the 3-D boundary layer equations fall into two main categories; finite difference schemes which predict flow properties at each of the mesh points across the layer, and integral methods which predict only the skin friction and certain integral properties of the boundary layer. For turbulent flow, both categories involve a good deal of empiricism and both are currently underdeveloped particularly when the flow is separated. There have been many investigations made of 3-D boundary layers on wings. Among those using finite difference formulations are the recent studies of Cebeci et al (Ref. 38) and McLean et al (Ref. 39). Both studies used eddy viscosity modeling. McLean et al made an interaction study by coupling the boundary

layer solution to the inviscid flow. The McLean procedure did not account for important wake effects and required too much computer time for it to be an effective wing design tool. Our 2-D viscous airfoil study indicates that there is always a strong wake curvature effect for subsonic trailing edges. It is our belief that this phenomenon is also important in the 3-D viscous wing problem and should be included in the theoretical formulation.

Integral boundary layer techniques have several advantages over the finite difference methods. They are usually easy to apply, the computations are fast, and the results are not overly sensitive to the choice of the turbulence models used. Myring (Ref. 40) has developed a fairly complete momentum integral prediction method for 3-D boundary layers in incompressible flow. The continuity equation (i.e., the entrainment equation) and the two Reynolds averaged momentum equations in directions parallel to the surface are used to derive a system of first-order partial differential equations for the momentum thickness along the mainstream direction, the shape factor, and the streamline deviation angle β (the angle between the external streamline and the limiting streamline at the wall). The global physical quantities (e.g., the momentum thickness in the transverse direction) are then implicitly dependent upon the deviation angle β. Myring's work has been extended by Smith (Ref. 41) to 3-D compressible turbulent boundary layer flow over an insulated surface. To improve the turbulence calculation, Green et al (Ref. 17) has developed a highly successful prediction method for 2-D compressible turbulent boundary layers and wakes. A one equation lag-entrainment method was developed to incorporate nonequilibrium "history" effects into the integral entrainment method. This method was used in our 2-D GRUMFOIL code.

The work of Smith and Green et al was combined by Stock (Ref. 16) to provide a 3-D extension of the compressible lag entrainment method. Stock's method also incorporates an integral method for 3-D laminar boundary layers. The laminar boundary layer formulation (Ref. 42) uses five equations, namely, continuity, two momentum equations along the surface and their respective first-order moment equations, to determine five flow parameters including the displacement thickness and the momentum thickness in the mainstream direction. The laminar integral is based on one-parameter Falkner-Skan velocity profile in the main stream direction and a two-parameter polynomial velocity profile for the cross flow.

Since we follow the same formulation as that of Smith and Stock, the derivation of the governing equations is not given in this report. However, certain modifications and extension of their work which are necessary for viscid-inviscid computations are discussed. These include, the derivation of the full metric coefficient taking into account the wing thickness and the variation of the wake shape, the extension of the calculation to 3-D viscous wakes and the derivation of the source distribution from the boundary layer solution for the transpiration boundary conditions.

It is important to mention that the resulting 2-D (coordinates along the surface) partial differential equations for turbulent flow governing the surface shape factor (H), the momentum thickness along the main stream direction (θ_{11}), and the streamline deviation angle β are of hyperbolic type with distinct characteristic curves (see Ref. 40 and 41). Similar conclusion can also be drawn for the equations for the laminar boundary layer. Therefore, the problem for the solution for the system of partial differential equation as an initial value problem is well posed provided proper initial conditions can be prescribed. We shall discuss this more in Subsection 4.2 of this report.

3.3 "ZONAL" APPROACH TO SOLUTIONS OF 3-D VISCOUS FLOW ON WINGS

From the discussions made in the two previous sections, our inviscid AFZ method for the 3-D potential flow solution and the integral methods for the boundary layer analysis comprise the necessary elements for the viscid-inviscid interactive analysis for the viscous flow about wings. Our boundary layer method follows Stock's (Ref. 16) treatment of the laminar and turbulent boundary layer computation on wings with our improvement that the wing thickness effect is taken into account. In addition, the complete 3-D viscous wake is computed to take into account the wake thickness effect for viscous interaction. In the present work, the transpiration coupling conditions are used for the displacement effect and the wake curvature condition along the wake streamline is determined from the iterative solution of the inviscid flow. In addition, a local 2-D trailing edge strong interaction solution is included, and imbedded in the global solution. The derivations of these conditions are given in Subsection 4.3 of this report.

4. NUMERICAL METHODS

4.1 INVISCID COMPUTATIONAL PROCEDURE

4.1.1 Basic Equations for 3-D Inviscid Flow

The basic equation describing irrotational, inviscid compressible flow can be written

$$\partial_x(\rho u) + \partial_y(\rho v) + \partial_z(\rho w) = 0 \qquad (4.1.1)$$

where ∂_x, ∂_y, and ∂_z represent partial differentiation with respect to Cartesian x, y, and z. It should be pointed out here that the notations used in describing the numerical techniques employed in computing the inviscid flow (Subsection 4.1) are different from those used for the viscous flow formulation (Subsections 4.2 and 4.3).

When the velocity is related to a potential by

$$\vec{q} = \begin{pmatrix} u \\ v \\ w \end{pmatrix} = \vec{\nabla}\phi + \vec{q}_\infty \qquad (4.1.2)$$

and the isentropic relation is used for the density

$$\rho = \left[1 + \frac{\gamma-1}{2} M_\infty^2 (1-q^2)\right]^{\frac{1}{\gamma-1}} \quad , \qquad (4.1.3)$$

we have a single partial differential equation to solve for the single variable, ϕ. In the above γ is the ratio of specific heats, q^2 and ρ are normalized by their free stream values and M_∞ is the Mach number of the free stream.

Equations (4.1.1) to (4.1.3) are transformed to a computational space with coordinates (X,Y,Z) by application of coordinate mappings according to the method described in Ref. 24. This consists of introducing parabolic coordinates $(\tilde{X},\tilde{Y})$ in spanwise planes (z = constant) by the transformation

$$(\tilde{X} + i\tilde{Y}) = \sqrt{[x-x_0(z)] + i\,[y-y_0(z)]}$$

$$\tilde{Z} = z$$

where $x_0(z)$, $y_0(z)$ define a singular line just inside the wing leading edge. The effect of the transformation is to unwrap the wing about the singular line to form a shallow bump, $\tilde{Y} = S(\tilde{X},\tilde{Z})$. The bump is then removed by a shearing transformation,

$$X' = \tilde{X},\ Y' = \tilde{Y} - S(\tilde{X},\tilde{Z}),\ Z' = \tilde{Z}$$

(see Fig. 1). A far field stretching is then used to define final computational variables X, Y, and Z.

If the transformations are represented by a Jacobian matrix

$$H = \begin{pmatrix} \partial_X x & \partial_Y x & \partial_Z x \\ \partial_X y & \partial_Y y & \partial_Z y \\ \partial_X z & \partial_Y z & \partial_Z z \end{pmatrix} \tag{4.1.4}$$

Eq (4.1.1) may be written in terms of transformed variables:

$$L_0(\phi) = \partial_X(\rho h U) + \partial_Y(\rho h V) + \partial_Z(\rho h W) = 0 \tag{4.1.5}$$

where

$$h = \det(H),$$

U, V, and W are contravariant velocities:

$$\begin{pmatrix} U \\ V \\ W \end{pmatrix} = H^{-1} \begin{pmatrix} u \\ v \\ w \end{pmatrix} \tag{4.1.6}$$

and the physical velocities are given in terms of derivatives of the potential in the transformed space:

$$\begin{pmatrix} u \\ v \\ w \end{pmatrix} = (H^T)^{-1} \begin{pmatrix} \partial_X \phi \\ \partial_Y \phi \\ \partial_Z \phi \end{pmatrix} + \begin{pmatrix} u_\infty \\ v_\infty \\ w_\infty \end{pmatrix} \tag{4.1.7}$$

4.1.2 Boundary Conditions

Initially, freestream conditions were set on the outer boundaries in the form $\phi = 0$ on $Y = Y_M$ and $\phi_X = 0$ on the surfaces $X = X_M$ and $X = -X_M$ (Fig. 1). These surfaces are far behind the wing in the physical space and are separated by the wake ($Y = 0$, $Z < Z_T$) shed from the trailing edge of the wing. The condition $\phi_X = 0$ requires that the streamwise tangential derivative of ϕ be zero at the wake in the far field. All boundaries are at a finite distance from the wing in the procedure used here so that it was felt that more accurate boundary conditions could be derived by assuming that the Prandtl-Glauert equation is valid at these boundaries and solving for the reduced velocity potential. The solution can be written formally as;

$$\phi \sim \phi_{LIFT} + 0\left(\frac{x}{R^3}\right) + 0\left(\frac{1}{R^3}\right)$$

where

$$\phi_{LIFT} = \frac{y}{4\pi} \iint_{W.S.} \frac{\frac{\partial \phi(\xi,\zeta)}{\partial \xi}}{(z-\zeta)^2+y^2} \left[1 + \frac{(x-\xi)}{R}\right] d\xi \, d\zeta$$

$$R = \left\{(x-\xi)^2 + \beta^2[(z-\zeta)^2 + (y-\eta)^2]\right\}^{1/2}$$

$$\beta^2 = 1 - M_\infty^2$$

ξ, η, ζ = surface coordinates of the wing (see Fig. 2).

where the integration is carried out over the wing surface (w.s.) The wing thickness integral of the order $0\left(\frac{x}{R^3}\right)$, and the volume integral of the order $0\left(\frac{1}{R^3}\right)$ are neglected in the far field compared to ϕ_{LIFT}. On the boundaries considered here (see Fig. 2), it is seen that, when $(y-\eta)^2 \ll 1$, then $(x-\xi)^2 \gg 0$. Also when $x \simeq 0(\xi)$, it follows that on the boundary, that $|y| \gg |\eta|$, irrespective of the values of z and ζ. A very good approximation for $\frac{(x-\xi)}{R}$ is then

$$\frac{(x - \xi)}{R} = \frac{(x - \xi)}{\{(x-\xi)^2 + \beta^2[y^2 + (z - \zeta)^2]\}^{1/2}} .$$

Further expansion to $O(\frac{\xi}{x})$ allows us to express ϕ_{LIFT} as:

$$\phi_{Far\ Field} = \phi_{LIFT} = \phi_I + \phi_{II}$$

with

$$\phi_I = \frac{y}{4\pi} \int_{-b/2}^{+b/2} \frac{(1 + \pi_1)\Gamma(\zeta)d\zeta}{(z - \zeta)^2 + y^2} \qquad (4.1.8a)$$

and,

$$\phi_{II} = \frac{y}{4\pi} \int_{-b/2}^{+b/2} \frac{d\zeta}{(z-\zeta)^2 + y^2} \pi_2 \{JUMP(x\phi)_{T.E.} - \tilde{\Gamma}(\zeta)\} \qquad (4.1.8b)$$

where

$$\pi_1 = x\{x^2 + \beta^2[y^2 + (z - \zeta)^2]\}^{-1/2}$$

$$\pi_2 = \{x^2 \{ x^2 + \beta^2[y^2 - (z-\zeta)^2] \}^{-3/2} - \{ x^2 + \beta^2[y^2 + (z-\zeta)^2] \}^{-1/2}\}$$

$$\Gamma(\zeta) = \oint \frac{d\phi}{d\xi}(\xi,\zeta)d\xi = \Delta\phi(\zeta) \quad (KUTTA)$$

$$\tilde{\Gamma}(\zeta) = \oint \phi(\xi,\zeta)d\xi$$

It can be shown that the expression for ϕ_I approaches the relation given by Klunker (Ref. 32) only for $x \to +\infty$ and differs from it otherwise. When $x \to -\infty$ $\phi_{LIFT} \to 0$ which is the correct behavior for the reduced potential in this limit. Although the code has been written to include both the ϕ_I and ϕ_{II} terms in the far field boundary conditions we have so far made extensive runs with only the first term included. The results obtained to date indicate that for a value of BOUND = .9 (i.e., on the boundary about 4 chords from the wing), using ϕ_I alone is quite sufficient. The computed lift results are

consistently higher than those satisfying free stream velocity at the boundary, indicating the importance of the effect of the far field boundary conditions. Also, the convergence rate is better than that achieved using the original freestream conditions previously discussed. Details of computed results will be discussed in Subsection 5.1 of this report.

The boundary condition on the surface $Z = Z_M$ (Fig. 1) is $\phi = 0$. A symmetry condition is used on $Z = 0$ (i.e., ϕ is reflected) since the flow is symmetric there.

The surface $Y = 0$ in the computational space contains the wing for $-X_{T.E.} < X < X_{TE}$ and $Z < Z_T$. The velocity tangency condition $V = 0$ is imposed here by setting $\phi_Y = 0$ on the wing surface. The wing trailing edge is mapped to two lines, $X = X_{TE}$ and $X = -X_{TE}$, $Z < Z_T$ in this plane, so that the wake from the wing trailing edge is mapped to two parts of the surface: $X > X_{TE}$ and $X < -X_{TE}$, $Z < Z_T$. Across these surfaces the normal velocity V and the pressure (p) are forced to be continuous so that both p and V must match at the two computational points corresponding to the same physical location. Since p is a function of q^2 alone in potential flow, and V and W are small compared to U (i.e., the coordinate surface is approximately aligned with the free stream) continuity of pressure is, to a good approximation, enforced by requiring continuity of U. This, in turn, requires continuity of ϕ_X. Since, for a lifting wing ϕ is not continuous across the trailing edge it is not continuous across these surfaces.

There are two options for positioning the wake in the computer code. The standard one involves keeping it fixed as the solution converges so that, in general, there will be (continuous) flow through it. The second option involves allowing the wake to follow the local velocity. With the latter the wake is still mapped to part of the $Y = 0$ surface and the mesh is iteratively adapted to the flow. This mapping requires that the height (Y value) of the wake be a single valued function of X and Z, which precludes its rolling up. The equations for this option are described in Subsection 4.1.5. Off the wing tip in the $Y = 0$ plane ($Z > Z_T$, all X) continuity of V and ϕ_X is enforced but no discontinuity of ϕ is allowed. The potential is then matched at points which coincide in the physical plane.

Two exceptional lines occur in the $Y = 0$ plane where special conditions are applied. The first is the line corresponding to the mapping singularity X

$= 0$ for $Z_T < Z < Z_M$. There, $\partial_X^2\phi + \partial_Y^2\phi = 0$ is enforced. The other corresponds to the wing tip, $Z = Z_T$, $-X_{TE} < X < X_{TE}$. There the physical vortex sheet would start to roll up. Since the computation constrains the sheet to start behind the wing and disallows roll up, an additional condition is required to avoid a singularity in V. It should be pointed out that this flat vortex sheet constraint is not inherent in the assumption of potential flow. The existence of a potential is consistent with the appearance of rolled up trailing vortex sheets or vortices at wing tips. Both these phenomenon can be modelled in full potential flow. The condition we impose (at the wing tip in the code) is that $\partial_Y^2\phi = 0$ all along this line, which insures that V is a local maximum. Thus far, the use of this condition has proved necessary in flows with highly loaded wing tip sections.

4.1.3 Discretization

The finite volume scheme of Ref. 24 is used to discretize Eq (4.1.5). Two staggered grids are used (see Fig. 3a). On one, ρ, u, v, w, U, V, W, H and h are defined; on the other, x, y, z, X, Y, Z, ϕ, and $L(\phi)$ are defined. The nodes of each grid are at the centers of the cells of the other, and a box scheme is used to compute the derivatives in Eq (4.1.4), (4.1.5), and (4.1.7a). For a variable f,

$$\delta_X f \Big|_{i+\frac{1}{2},j+\frac{1}{2},k+\frac{1}{2}} = [f_{i+1,j+1,k+1} + f_{i+1,j,k+1} + f_{i+1,j+1} + f_{i+1,j,k}$$

$$- f_{i,j+1,k+1} - f_{i,j,k+1} - f_{i,j+1,k} - f_{i,j,k}]/4$$

Similar expressions can be written for the Y and Z derivatives.

The indices i, j, k are used for the computational coordinates X, Y, and Z which are normalized such that

$$\Delta X = \Delta Y = \Delta Z = 1$$

Using these relations, all the partial derivatives in Eq (4.1.4), (4.1.5) and (4.1.7) are replaced by finite differences and the equations become finite difference equations.

The wing surface bisects the flux balance cell such that four cell corners are above the surface and four image corners below. The values of U and W below the surface occuring in the discrete version of Eq (4.1.5) are set equal to those above, and the values of V set equal to the negative of the values above. This is described, in 2-D, in Fig. 3b. Across the wake the same flux balance is used as in the interior. The values of U, V, and W at the image corners on one side are taken to be the values above the surface on the other side. This defines the equations on one side of the wake in the computational plane and ensures that V is continuous to second order at convergence. On the other side of the wake values of ϕ are used equal to values at corresponding points on the first side, with a constant discontinuity (in each Z plane). The value of this discontinuity is determined at the trailing edge points in each plane. This enforces continuity of pressure as described above.

The same procedure is used beyond the wing tip where there is no discontinuity. The far field boundary conditions are evaluated by numerically integrating Eq (4.1.8) with the jump in potential given at the trailing edge of each Z = constant section for $Z < Z_T$.

The basic finite volume scheme leads to an odd-even decoupling of solutions. If a small term is added to the left hand side ($L_o(\phi)$) of Eq (4.1.5), this problem can be eliminated. First, $L(\phi)$ is expanded:

$$L(\phi) \approx A\, \partial_X^2 \phi + B\, \partial_Y^2 \phi + C\, \partial_Z^2 \phi + \text{other terms.}$$

The coefficients A, B, and C can be found from the nonconservative quasilinear formulation:

$$A = \rho h(g_{1,1} - U^2/a^2)$$

$$B = \rho h(g_{2,2} - V^2/a^2)$$

$$C = \rho h(g_{3,3} - W^2/a^2)$$

where $g_{i,i}$ are the diagonal elements of $(H^T H)^{-1}$ and a is the local speed of sound. The recoupling terms are then

$$L_{rec}(\phi) = \delta_{XY}(A+B)\delta_{XY}\phi + \delta_{YZ}(B+C)\delta_{YZ}\phi + \delta_{ZX}(C+A)\delta_{ZX}\phi$$

$$+ \delta_{XYZ}(A+B+C)\delta_{XYZ}\phi$$

Here,

$$\delta_{XY}f\Big|_{i+\frac{1}{2},j+\frac{1}{2},k+\frac{1}{2}} = [f_{i+1,j+1,k+1} - f_{i,j+1,k+1} - f_{i+1,j,k+1} + f_{i,j,k+1}$$

$$+ f_{i+1,j+1,k} - f_{i,j+1,k} - f_{i+1,j,k} + f_{i,j,k}]/2$$

etc, and

$$\delta_{XYZ}f = [f_{i+1,j+1,k+1} - f_{i,j+1,k+1} - f_{i+1,j,k+1} + f_{i,j,k+1}$$

$$- f_{i+1,j+1,k} + f_{i,j+1,k} + f_{i+1,j,k} - f_{i,j,k}]$$

It can be seen that $L_{rec}(\phi)$ is of second order with respect to the terms in $L_o(\phi)$.

For stability in the supersonic zone, either a first order or a second order artificial viscosity can be used. The first order form is less accurate but results in faster, more reliable convergence to a solution in general.

For the first order form a switching function is first defined:

$$s = \max(0,\ 1 - M_c^2/M^2)$$

where

$$M^2 = q^2/a^2$$

and M_c is a switching Mach number, slightly less than 1 ($\approx .95$). Then,

$$P = \mu(U^2\delta_X{}^2 + \frac{UV}{4}\delta_{XY}\phi + \frac{WU}{4}\delta_{ZX}\phi)$$

$$Q = \mu(V^2\delta_Y^2\phi + \frac{VW}{4}\delta_{YZ}\phi + \frac{UV}{4}\delta_{XY}\phi)$$

$$R = \mu(W^2\delta_Z^2\phi + \frac{WU}{4}\delta_{ZX}\phi + \frac{VW}{4}\delta_{YZ}\phi$$

$$\mu = c\rho h^2/a^2$$

where c is a constant and the second order difference operators are as defined previously, with, in addition,

$$\delta_x^2 f = f_{i+1,j,k} - 2f_{i,j,k} + f_{i-1,j,k}$$

etc.

In terms of these quantities, for flow with U and W positive and V negative, the artificial viscosity term is

$$L_{vis}\phi = P_{i,j,k} - P_{i-1,j,k} + Q_{i,j,k} - Q_{i,j-1,k} + W_{i,j,k} - W_{i,j,k-1}$$

(a negative V implies flow in the increasing j direction).

This is first order compared to $L_0(\phi)$. If this artificial viscosity option is chosen, the complete equation to be solved for the potential, ϕ, at each point is

$$L_0(\phi) + L_{rec}(\phi) + L_{vis}(\phi) = 0$$

In order to achieve second order accuracy in the supersonic zone $L_{vis}\phi$ is replaced by (again for U and W positive and V negative);

$$L_{vis}\phi = (P_{i,j,k} - \varepsilon_{i,j,k}P_{i-1,j,k}) - (P_{i-1,j,k} - \varepsilon_{i-2,j,k}P_{i-2,j,k})$$

+ similar terms for Q and R.

The local parameter $\varepsilon_{i,j,k}$ is included for stability at shocks. $\varepsilon_{i,j,k} = 1$ forces the scheme with $L_{vis}\phi$ added to be second order, while $\varepsilon_{i,j,k,} = 0$ forces $L_{vis}\phi$ to the first order form defined previously. In the work of Ref. 33 it is shown that the scheme had to be first order near shocks for stability. Hence, the form

$$\varepsilon_{i,j,k} = \max(0, (1 - \nu_2 - \nu_3 \lambda))$$

is used, where ν_2 and ν_3 are adjustable parameters and $\lambda \equiv \rho_{i,j,k} - \rho_{i-1,j,k}$ is used to detect the shock. This is small in the smooth parts of the flow and large near the shocks. To use the first-order option in the code, $\nu_2 = 1$ and $\nu_3 = 0$. For the second-order option, $\nu_2 = 0$ and $\nu_3 = 4$. We have found significant differences in the flow field in the supersonic zone between the first and second order schemes. For the second order scheme, the shocks are captured over fewer mesh points. Results using the first and second order schemes will be compared in Subsection 5.1 of this report.

4.1.4 AFZ Scheme

The basic idea behind the AFZ scheme is to solve a set of implicit equations in each constant Z-plane, for a correction to ϕ. Since no implicit equations are solved in the Z direction, the 3-D array of ϕ values can be stored on disk and only several X-Y planes of data need be stored in the computer at any one time.

During the iteration of sweep number n+1, when updating plane number k, values of ϕ are available corresponding to iteration n+1 in plane k-1 since it has just been updated. Only unupdated (level n) values are available in planes k and k+1. It was decided to make use of the available updated values in computing the residual at plane k, as is done in successive-line-overrelaxation (SLOR) where updated values in the previous line are used and implicit equations are solved along each line. It is most efficient to compute contravariant velocities once each iteration between each plane and use them in computing $L_0(\phi)$ for both planes on either side. To directly incorporate updated values of ϕ into each $L_0(\phi)$ computation, it would be necessary to abandon this approach and recompute these velocities, using them only once for each $L_0(\phi)$ computation. This would almost double the number of required calculations. An alternative which was chosen involved adding the correction multiplied by an appropriate constant to $L_0(\phi)$ computed using only old values at each plane. Our scheme thus had the form

$$N_{XY}\ \delta\phi^n = \alpha\omega L(\phi^n) + \alpha\omega\tilde{C}E_z^-\ \delta\phi^n, \qquad (4.1.9)$$

$$\phi^{n+1} = \phi^n + \delta\phi^n$$

where N_{XY} is an operator in the XY plane, α may be an operator, ω is a relaxation factor and E_z^- is the shifting operator:

$$E_z^- \delta\phi_k = \delta\phi_{k-1}$$

If $L(\phi^n)$ is a Laplacian,

$$L_L(\phi) = A\delta_X^2\phi + B\delta_Y^2\phi + C\delta_Z^2\phi$$

then choosing $\tilde{C} = C$ would make the right hand side, at plane k, equal to

$$\alpha\omega[A\delta_X^2\phi_k^n + B\delta_Y^2\phi_k^n + C(\phi_{k-1}^{n+1} - 2\phi_k^n + \phi_{k+1}^n)]$$

which is $\alpha\omega\, L_L(\phi)$ computed using the latest available values of ϕ. For our nonlinear case we used a similar approach for determining $\tilde{C}$.

The operator N_{XY} was chosen from successful 2-D ADI schemes (Ref. 34):

$$N_{XY} = (\alpha_X - \delta_X A \delta_X)(\alpha_Y - \delta_Y B \delta_Y) \quad .$$

The values of A and B are given by the expansion of $L_o(\phi)$, described previously. Also, α_X and α_Y are numbers at low speed, and, following the approach of Ref. 34, become operators for supersonic flow. They also include a part to approximate $L_{vis}(\phi)$ in addition to $L_o(\phi)$.

For flow in the $\pm X$, $+Y$ direction,

$$\alpha = \alpha_o + \alpha_1\delta_X^{\mp} + \alpha_2\delta_Y^-$$

where

$$\alpha_o = \max(\beta_o, \beta_1) \ ,$$

$$\beta_o = P_1\, \Delta z\, r(Z)\, \max(0,\ 1 - q^2/a^2)$$

$$\beta_1 = 2\, P_1\, r(Z)\, \tilde{C}$$

$$\alpha_1 = P_4\, P_1\, \Delta z\, r(Z)\, \min\,(1, q^4/a^4)\, f(U)$$

$$\alpha_2 = P_5 \, P_1 \, \Delta z \, r(Z) \min \, (1, \, q^4/a^4) \, .$$

In the above, Δz is the difference in physical z values between planes, f(U) is 1 except near the point where U changes sign, C is an expansion coefficient described previously, P_1 - P_5 are constants for each iteration and

$$r(Z) = 1 + Z/Z_{\text{wing tip}} \, .$$

We also use

$$\tilde{C} = P_2 \, \alpha_0$$

except at the root plane (Z = 0), where

$$\tilde{C} = P_2 \, \alpha_0/1.1 \quad .$$

The relaxation factor ω is given by

$$\omega = P_3 \, (1 + 1/r(Z)) \quad .$$

Also, to approximate first order artificial viscosity terms

$$\alpha_X = \alpha - \delta_X^{\mp} \, \mu \, U^2 \delta_X^2$$

$$\alpha_Y = \alpha - \delta_Y^{+} \, \mu \, V^2 \delta_Y^2$$

where μ is defined previously. To approximate second order artificial viscosity, we use

$$\alpha_X = \alpha - \delta_X^{\mp} \, \mu U^2 (1 + \varepsilon) \delta_X^2$$

$$\alpha_Y = \alpha - \delta_Y^{+} \, \mu V^2 (1 - \varepsilon) \delta_Y^2$$

where ε is defined above.

The form for α_0 was chosen to become small when the local Mach number approached 1, which is required for stability. However, modal analysis showed that, in far field regions, where the grid is stretched in X and Y, but not in Z, there is a lower bound on α_0 for stability (for elliptic flow). The

functions β_0 and β_1 represent these two competing requirements. The parameters α_1 and α_2 were designed to become small for low speed flow so that α would then be a number instead of an operator. Finally, it was found that the minimum α for stability increased with increasing Z. The function r(Z) was accordingly included to improve convergence. The use of 1/r(Z) in the formula for ω results in a relative under-relaxation for larger values of Z, which further increases stability and improves convergence.

The solution sequence consists of a set of cycles. In each cycle,there are K sweeps through the field, in which values of P_1 are cycled and set equal to P_1^o, eP_1^o, $e^2P_1^o$, ... $e^{K-1}P_1^o$. All other parameters are kept constant. Best results were found for K = 4 and e = 1/2, for fine grid transonic calculations. In each sweep, the factorized equations (4.1.9) are solved plane-by-plane starting from the wing root, for corrections, $\delta\phi$, which are added to ϕ. In each plane, first,

$$(\alpha_\chi - \delta_\chi A \delta_\chi)\tilde{\phi} = \alpha\omega L(\phi^n) + \alpha\omega\tilde{C}\bar{E}_Z\delta\phi^n \qquad (4.1.10)$$

is solved row-by-row for a temporary 2-D variable $\tilde{\phi}$. Then,

$$(\alpha_\gamma - \delta B \delta_\gamma)\delta\phi = \tilde{\phi} \qquad (4.1.11)$$

is solved column-by-column for the correction, $\delta\phi$. The third order operator terms in α_γ are all in one direction, since the Y-velocity always has the same sign so that there are four diagonals in the equivalent matrix Eq (4.1.11) for $\delta\phi$, instead of the three that would occur if only α were used instead of α_γ. Thus, a four-diagonal solver, which is only slightly more complicated than a three-diagonal one is required. For the solution of (4.1.10), a five-diagonal solver is required since, in the mapped plane, the flow changes direction along the line being solved, and derivatives in both directions occur. Again, this does not require much more computation than a tridiagonal solution.

4.1.5 Fitted Wake Calculation

In each span station (z-const) a "C" mesh is generated. The inner-most coordinate line partly lies on the wing surface. The rest of the line lies between the trailing edge and the downstream boundary (see Fig. 4).

The grid points are labeled with indices i, j, and k corresponding to computational X, Y, and Z coordinates. Our concern will be lines B-A and D-E. We will want them to follow the wake streamline from the trailing edge (t.e.) to the downstream boundary. Points along these lines will be denoted $(x,y) = (x^+_{i,k}, y^+_{i,k})$ or $(x^-_{i,k}, y^-_{i,k})$ with $z = z_k$, independent of i. We define $i = 1$ at the t.e. and $i = N$ downstream. Points on line B-A are denoted by (+) and on line D-E by (-).

We set $x^+_{i,k} = x^-_{i,k}$, and determine $\delta_{ik} = y^+_{i,k} - y^-_{i,k}$ from a computed wake thickness. Then, denoting the mean value

$$y_{i,k} = \frac{1}{2}\left(y^+_{i,k} + y^-_{i,k}\right),$$

and

$$x_{i,k} = x^+_{i,k} = x^-_{i,k},$$

the condition that the median wake line follow the wake streamline is that

$$\frac{v_{i,k}}{u_{i,k}} = \frac{y_{i+1,k} - y_{i,k}}{x_{i+1,k} - x_{i,k}} \qquad (4.1.12)$$

where $u_{i,k}$ and $v_{i,k}$ are mean physical velocities defined in plane k:

$$u_{i,k} = \frac{1}{2}\left(u^+_{i,k} + u^-_{i,k}\right)$$

$$v_{i,k} = \frac{1}{2}\left(v^+_{i,k} + v^-_{i,k}\right)$$

During each iteration, for which new values of the potential function, ϕ, are computed, a displacement $\Delta y_{i,k}$ is computed such that Eq (4.1.12) is satisfied. These displacements are then added to each node corresponding to the same i and k for the next potential iteration. The formula used for computing the $\Delta y_{i,k}$'s is

$$\Delta y_{i+1,k} = \omega\left[\frac{v_{i,k}}{u_{i,k}}\left(x_{i+1,k} - x_{i,k}\right) - \left(y_{i+1,k} - y_{i,k} - \Delta y_{i,k}\right)\right]$$

where ω is a relaxation factor (presently set to 1).

The physical velocities $u^{\pm}_{i,k}$, $v^{\pm}_{i,k}$ are computed from the metric and velocity potential ϕ values at surrounding points:

$$u = (\delta_Y y \delta_X \phi - \delta_X y \delta_Y \phi)/h + \cos \alpha \quad ,$$

$$v = (-\delta_Y x \delta_X \phi + \delta_X x \delta_Y \phi)/h + \sin \alpha \quad ,$$

$$h = \delta_Y y \delta_X x - \delta_X y \delta_Y x.$$

In the above, for $u^{+}_{i,k}$ and $v^{+}_{i,k}$, the differences are computed by

$$\delta_X F = \frac{1}{2} (F^{+}_{i+1,\ k+1} - F^{++}_{i,k} + F^{+}_{i+1,k} - F^{+}_{i,k}),$$

$$\delta_Y F = \frac{1}{2} (F^{+}_{i+1,\ k} + F^{++}_{i,k} - F_{i+1,k} - F^{+}_{i,k})$$

where superscripts (++) denote quantities on the line above those denoted by (+). Similar equations with (+) changed to (-) are used to compute $u^{-}_{i,k}$, $v^{-}_{i,k}$. The velocities are normalized to unity in the free stream and α denotes the angle of attack.

During each iteration a boundary value problem is solved (approximately) for the potential ϕ, regarding the boundary lines B-A and D-E as fixed. The corrections are then added to the coordinate so that these lines follow the t.e. streamline, which moves from iteration to iteration. The boundary conditions on ϕ are that pressure is equal on the top and bottom of the lines and normal flux through the lines is conserved. These are boundary conditions since the lines are mapped to two segments of the outer boundary of the computational domain (Fig. 4). Hence, after each ϕ iteration fluid is flowing through the lines. This is then corrected by moving the coordinate system using the computed corrections.

The wake lines bisect a set of cells which have velocities defined on the corners, and values of ϕ and x and y defined in the centers (Fig. 5). To second order in cell mesh size, balance of the fluxes in the cells requies that the normal flux be continuous through the wake line. This flux balance relation is just what is imposed in the interior of the domain. Hence, by

extending it to the boundary cells the velocity boundary condition is enforced along line A-B.

The other condition is a force balance, imposed by specifying ϕ along line D-E. This is used to determine ϕ_s, the derivative along the line. The isentropic equation for the pressure, which is used to set a relation for ϕ_s, is

$$p = \frac{1}{\gamma M_\infty^2}\left[1 + \frac{\gamma-1}{2} M_\infty^2 (1-\hat{q}^2)\right]^{\gamma/\gamma-1} \tag{4.1.13}$$

where

$$\hat{q}^2 = u^2 + v^2 = (\phi_n + q_n^\infty)^2 + (\phi_s + q_s^\infty)^2 \tag{4.1.14}$$

In the above, $q_{n,s}^\infty$ are the normal and tangential components of the free stream velocity with respect to the line.

A pressure $(p_{i,k}^+)$ is first computed along A-B. Then, a desired pressure, $(p_{i,k}^-)$ is computed for each point along D-E, using a force balance relation. Also, a normal velocity, $q_n = \phi_n + q_n^\infty$, is also computed at each point. Equations (4.1.13) and (4.1.14) are then solved for a desired ϕ.

At present, we are only implementing a simplified version of this relation: if $q_n^2 << q_s^2$, then

$$p = \frac{1}{\gamma M_\infty^2}\left[1 + \frac{\gamma-1}{2} M_\infty^2 (1 - q_s^2)\right]^{\gamma/\gamma-1} + O(q_n^2/q_s^2) \tag{4.1.15}$$

Also, in this approximation the flow on the upper and lower sides of the wake are in the x-y plane. Hence the curvature in the flow direction is the same on both sides and the pressure relation, neglecting viscous effects, is just

$$p_{i,k}^+ = p_{i,k}^-$$

Using approximation (4.1.15) we then have

$$q_{s\ i,k}^+ = q_{s_{i,k}}^-$$

or

$$\phi^{+}_{s_{i,k}} = \phi^{-}_{s_{i,k}}$$

Thus, $\phi^{-}_{i,k} = \phi^{+}_{i,k} + \Gamma_k$, where Γ_k is a constant computed at the t.e. in each plane after each iteration.

Presently, we are implementing a curvature calculation with the assumption that the flow is entirely in each x-y plane. Although the inviscid pressure balance relation does not require this curvature effect, the viscous corrections do. At each point along the wake midway between the coordinate points we have the unit normal (see Fig. 6a):

$$\hat{n}_{i+1/2,k} = (-(y_{i+1,k} - y_{i,k}), (x_{i+1,k} - x_{i,k}))/DS_{i+1/2,k}$$

where

$$DS_{i+1/2,k} = [(x_{i+1,k} - x_{i,k})^2 + (y_{i+1,k} - y_{i,k})^2]^{1/2}$$

The radius of curvature, R, can be defined by

$$R_{i,k} = \frac{\Delta S_{i,k}}{\Delta\theta_{i,k}} + O(\Delta\theta^2)$$

where

$$\Delta S_{i,k} = [(x_{i+1,k} - x_{i-1,k})^2 + (y_{i+1,k} - y_{i,k})^2]^{1/2}$$

and $\Delta\theta_{i,k}$ is the angle between normals $\hat{n}_{i+1/2,k}$, $\hat{n}_{i-1/2,k}$:

$$\Delta\theta_{i,k} = \cos^{-1}(\hat{n}_{i+1/2,k} \cdot \hat{n}_{i-1/2,k}).$$

Although we have not implemented a general curvature calculation, which would be required when the flow has a large spanwise velocity component, we give the formulation here. Considering two lines,

$$(i,k-1) \rightarrow (i,k+1)$$

and

$$(i-1,k) \rightarrow (i+1,k)$$

we can define a vector normal to the wake surface (see Fig. 6b):

$$\vec{n}_{i,k} = (\vec{r}_{i+1,k} - \vec{r}_{i,k-1}) \times (\vec{r}_{i+1,k} - \vec{r}_{i-1,k}).$$

This is second order accurate if the mesh is smoothly varying.

We will define curvature in a coordinate system consisting of $\vec{n}_{i,k}$, $\delta_i \vec{r}_{i,k} \equiv (\vec{r}_{i+1,k} - \vec{r}_{i,k})$, and $\vec{S}_{i,k} \equiv \vec{n}_{i,k} \times \delta_i \vec{r}_{i,k}$.

We now take normals, as before, midway between points i+1,k and i,k, and between i,k and i-1,k:

$$\vec{n}_{i+1/2,k} = (\vec{r}_{i+1,k} - \vec{r}_{i,}) \times (r_{i,k+1} - \vec{r}_{i,k-1})$$

$$\vec{n}_{i-1/2,k} = (\vec{r}_{i,k} - \vec{r}_{i-1,k}) \times (\vec{r}_{i,k+1} - \vec{r}_{i,k-1})$$

The scalar product then gives the relative angle at i,k for radial lines intersecting (i+1,k) → (i-1,k):

$$\Delta S^i_{i,k} = \cos^{-1}[(\vec{n}_{i+1/2,k} \cdot \vec{n}_{i-1/2,k})/(|\vec{n}_{i+1/2,k}||\vec{n}_{i-1/2,k}|)]$$

The distance between the mid points,

$$\Delta S^i_{i,k} = |\vec{r}_{i+1,k} - \vec{r}_{i-1,k}|/2$$

then is used to get the radius of curvature:

$$R^i_{i,k} = \frac{\Delta S^i_{i,k}}{\Delta \theta^i_{i,k}} + O(\Delta\theta^2)$$

The radius of curvature along the line (i,k+1) → (i,k-1), $R^k_{i,k}$ can then be computed in exactly the same way by interchanging the two lines. The radius of curvature in the normal direction ($S_{i,k}$) can then be computed:

$$R^s_{i,k} = (R^k_{i,k} - R^i_{i,k} \cos \beta_{i,k})/\sin \beta_{i,k}$$

where

$$\beta_{i,k} = \cos^{-1}[\delta_i \vec{r}_{i,k} \cdot (\vec{r}_{i,k+1} - \vec{r}_{i,k-1})/(|\delta_i \vec{r}_{i,k}||\vec{r}_{i,k+1} - \vec{r}_{i,k-1}|)$$

We have tested the AFZ code with the fitted trailing wake on a number of wings. A typical transport type configuration in shown in Fig. 7a. Shown in the figure is a 3-D view of the wing and the isobars on the upper surface of the wing for an angle of attack of 1.5° (upper half of the figure) and 0° (lower half). Both cases are at a free stream Mach number of .82. At 1.5° angle of attack one can see two shocks at the root section which merge at about midspan. Figure 7b shows a 3-D view of the wing and the trailing wake. Figure 7c compares the convergence of lift for calculations with and without the fitted wake. The figure shows the same convergence rates while the final lifts are slightly different. For this case (freestream Mach number of .82 and angle of attack of 1.5°) the converged C_L = .588 for the fitted wake calculation while the calculation without tracking the wake gave C_L = .590.

4.2 SOLUTION OF 3-D BOUNDARY LAYER & WAKE

In this section, we discuss briefly the numerical procedure for obtaining the solution of the 3-D boundary layer and wake by the integral method of Myring-Smith-Stock. We shall stress the modifications and improvements whenever they occur but neglect the detailed derivation of the governing equations. Since the solution procedures for the laminar and turbulent boundary layers are identical, only the latter is discussed. The governing differential equations for the integral laminar boundary layers can be found in the report of Stock (Ref. 42). The notations for the coordinates used in this section and the subsequent ones in this report are redefined and different from those used in Subsection 4.1 of the inviscid flows.

4.2.1 Coordinate System & Governing Equations

A curvilinear nonorthogonal surface coordinate system (x,y) coinciding with the wing surface and the wake is chosen for the differential equations. The coordinate x is along the chord direction while the coordinate y is along the constant percentage chord line as shown in Fig. 8. Shown also are the

velocity components u, v along x, y, respectively, $\tilde{\lambda}$ is the angle between x, y axes at any point on the surface, $\tilde{\alpha}$ is the angle between the external streamline and x axis. If the Cartesian coordinates (X,Y,T) of the wing and the wake are given, the unique transformation

$$\begin{aligned} X &= X(x,y) \\ Y &= Y(x,y) \\ T &= T(x,y) \end{aligned} \tag{4.2.1}$$

exists, from which the metric coefficients, h_1, h_2, g of the curvilinear system can be derived, where,

$$\begin{aligned} h_1^2 &= \left(\frac{\partial X}{\partial x}\right)^2 + \left(\frac{\partial Y}{\partial x}\right)^2 + \left(\frac{\partial T}{\partial x}\right)^2 \\ h_2^2 &= \left(\frac{\partial X}{\partial y}\right)^2 + \left(\frac{\partial Y}{\partial y}\right)^2 + \left(\frac{\partial T}{\partial y}\right)^2 \\ g &= \left(\frac{\partial X}{\partial x}\right)\left(\frac{\partial X}{\partial y}\right) + \left(\frac{\partial Y}{\partial x}\right)\left(\frac{\partial Y}{\partial y}\right) + \left(\frac{\partial T}{\partial x}\right)\left(\frac{\partial T}{\partial y}\right). \end{aligned} \tag{4.2.2}$$

Further reduction suitable for numerical implementation leads to

$$\begin{aligned} h_1 &= \left(\frac{\partial X}{\partial x}\right)\left[1 + \left(\frac{\partial T}{\partial X}\right)^2\right]^{1/2} \\ h_2 &= \left(\frac{\partial Y}{\partial y}\right)\left[\left(\frac{\partial X}{\partial Y}\right)^2 + 1 + \left(\frac{\partial T}{\partial Y}\right)^2\right]^{1/2} \\ g &= \left(\frac{\partial Y}{\partial y}\right)\left(\frac{\partial X}{\partial x}\right)\left[\left(\frac{\partial X}{\partial Y}\right) + \left(\frac{\partial T}{\partial X}\right)\left(\frac{\partial T}{\partial Y}\right)\right]. \end{aligned} \tag{4.2.3}$$

The term $\frac{\partial X}{\partial Y}$ is related to the sweep of the coordinate line y while $\frac{\partial T}{\partial X}$ and $\frac{\partial T}{\partial Y}$ are the slopes of the wing/wake surface. Since the boundary layer equations will involve x, y derivatives of h_1, h_2, and g, the curvature terms

$\frac{\partial^2 T}{\partial X^2}$, $\frac{\partial^2 T}{\partial Y^2}$ can affect significantly the solution of the boundary-layer equations.

Denoting the velocity components along the nonorthogonal curvilinear coordinate system (x,y,z) (z being normal to the wing/wake surface) as (u,v,w) (see Fig. 8), respectively, the boundary-layer momentum integral equations as given by Myring are, along the x direction,

$$\frac{1}{h_1}\frac{\partial \Theta_{11}}{\partial x} + \Theta_{11}\left\{\frac{(2-M^2)}{h_1}\frac{1}{u_e}\frac{\partial u_e}{\partial x} + \frac{1}{q}\frac{\partial}{\partial x}\left(\frac{q}{h_1}\right) + k_1\right\} + \frac{1}{h_2}\frac{\partial \Theta_{12}}{\partial y}$$

$$+ \Theta_{12}\left\{\frac{(2-M^2)}{h_2}\frac{1}{u_e}\frac{\partial u_e}{\partial y} + \frac{1}{q}\frac{\partial}{\partial y}\left(\frac{q}{h_2}\right) + k_3\right\} + \Delta_1\left\{\frac{1}{h_1}\frac{1}{u_e}\frac{\partial u_1}{\partial x} + k_1\frac{u_1}{u_e}\right\}$$

$$+ \Delta_2\left\{\frac{1}{h_2}\frac{1}{u_e}\frac{\partial u_1}{\partial y} + k_2\frac{v_1}{u_e} + k_3\frac{u_1}{u_e}\right\} + \Theta_{22}k_2 = \frac{C_{f1}}{2} \qquad (4.2.4)$$

and along the y direction,

$$\frac{1}{h_1}\frac{\partial \Theta_{21}}{\partial x} + \Theta_{21}\left\{\frac{(2-M^2)}{h_1}\frac{1}{u_e}\frac{\partial u_e}{\partial x} + \frac{1}{q}\frac{\partial}{\partial x}\left(\frac{q}{h_1}\right) + \ell_3\right\} + \frac{1}{h_2}\frac{\partial \Theta_{22}}{\partial y}$$

$$+ \Theta_{22}\left\{\frac{(2-M^2)}{h_2}\frac{1}{u_e}\frac{\partial u_e}{\partial y} + \frac{1}{q}\frac{\partial}{\partial y}\left(\frac{q}{h_2}\right) + \ell_2\right\} + \Delta_1\left\{\frac{1}{h_1}\frac{1}{u_e}\frac{\partial v_1}{\partial x} + \ell_1\frac{u_1}{u_e} + \ell_3\frac{v_1}{u_e}\right\}$$

$$+ \Delta_2\left\{\frac{1}{h_2}\frac{1}{u_e}\frac{\partial v_1}{\partial y} + \ell_2\frac{v_1}{u_e}\right\} + \Theta_{11}\ell_1 = \frac{C_{f2}}{2} \qquad (4.2.5)$$

where M is the Mach number at the edge of the boundary layer and C_{f1} and C_{f2} are the skin-friction coefficients in the x and y directions respectively. The velocity components in the x, y directions at the edge of the boundary layer are denoted by u_1, v_1 and the resultant velocity at the boundary-layer edge is denoted by u_e where

$$u_e^2 = u_1^2 + v_1^2 + \frac{2g}{h_1 h_2}u_1 v_1 \quad .$$

The momentum integral thicknesses Θ_{11}, Θ_{12}, Θ_{21}, and Θ_{22} and the mass integral thicknesses Δ_1 and Δ_2 together with the quantities k_1, k_2, k_3, ℓ_1, ℓ_2, ℓ_3 and q as functions of the metric coefficients h_1, h_2, g are given in Appendix A of Ref. 41.

The entrainment or the integral form of the continuity equation assumes the form,

$$\frac{1}{\rho_e u_e q}\left[\frac{\partial}{\partial x}\left\{\frac{\rho_e q}{h_1}\left(u_1\delta - u_e\Delta_1\right)\right\} + \frac{\partial}{\partial y}\left\{\frac{\rho_e q}{h_2}\left(v_1\delta - u_e\Delta_2\right)\right\}\right] = \frac{1}{u_e}\left[\frac{u_1}{h_1}\frac{\partial\delta}{\partial x} + \frac{v_1}{h_2}\frac{\partial\delta}{\partial y} - w_1\right] = F \tag{4.2.6}$$

where ρ_e is the density at the boundary-layer edge and δ denotes the boundary layer thickness. F is the entrainment coefficient, i.e., the *nondimensional* rate of change of mass flow in the boundary layer. The entrainment equation is used to provide an independent relation in this procedure by prescribing the entrainment coefficient as a function of the local boundary layer properties. In the lag entrainment method employed here, this information is supplied through a separate differential equation for the entrainment coefficient F derived from an approximation to the turbulent kinetic energy equation.

From the entrainment equation, one can derive a useful expression for the source velocity distribution, that is, the normal velocity outflow due to the presence of the boundary layer,

$$m = \frac{1}{\rho_e q}\left[\frac{\partial}{\partial x}\left(\frac{\rho_e q u_e \Delta_1}{h_1}\right) + \frac{\partial}{\partial y}\left(\frac{\rho_e q u_e \Delta_2}{h_2}\right)\right] \tag{4.2.7}$$

Another useful form of the entrainment equation is,

$$\frac{\partial}{\partial x}\left(\frac{\rho_e q u_1 \delta^*}{h_1}\right) + \frac{\partial}{\partial y}\left(\frac{\rho_e q v_1 \delta^*}{h_2}\right) = \frac{\partial}{\partial x}\left(\frac{\rho_e q u_e \Delta_1}{h_1}\right) + \frac{\partial}{\partial y}\left(\frac{\rho_e q u_e \Delta_2}{h_2}\right) \tag{4.2.8}$$

which allows the displacement thickness δ^* to be computed when the integral quantities Δ_1 and Δ_2 are known.

Equations (4.2.4), (4.2.5), and (4.2.6) form the foundation for the basic equations, and in addition, we adopt along the direction of the stream tube

lag-entrainment model equation of Green (Ref. 17) for the entrainment coefficient F. However, for a closed system, the total number of unknowns must be reduced to four. The integral thicknesses Θ_{11}, Θ_{12}, Θ_{21}, Θ_{22} Δ_1, Δ_2 (i.e., the unknowns) can be expressed in terms of the corresponding expressions denoted by θ_{11}, θ_{12}, θ_{21}, θ_{22} δ_1, δ_2, $\tilde{\lambda}$ and $\tilde{\alpha}$. These quantities, except for $\tilde{\lambda}$ and $\tilde{\alpha}$, are defined in terms of velocity components in the directions along and normal to the local external streamlines. The quantity $\tilde{\alpha}$ is the angle between the x-axis and the external streamline and $\tilde{\lambda}$ is the angle between the x and y axes. Then by further introducing an empirical cross flow velocity profile, we finally can reduce the system of four equations for the four unknowns, namely, $\bar{H}$, the equivalent incompressible shape factor, θ_{11}, the momentum thickness defined with the main stream direction velocity, F, the entrainment coefficient and γ, a cross flow boundary layer parameter equal to or implicitly related to the wall limiting streamline angle β relative to the external streamline, dependent upon whether the empirical cross flow profile of Mager (Ref. 43) or Johnston (Ref. 44) is used.

The equations are completed by an expression relating skin friction, C_f, to the boundary layer variables θ_{11}, $\bar{H}$, and the external conditions. First, we note that the components C_{f1} and C_{f2} along x and y directions can be expressed in terms of the skin friction magnitude, C_f and the angles $\tilde{\lambda}$, $\tilde{\alpha}$, and β by the relations,

$$C_{f1} = C_f \left\{\frac{\sin(\tilde{\lambda} - \tilde{\alpha}) - \cos(\tilde{\lambda} - \tilde{\alpha}) \tan(\beta)}{\sin \tilde{\lambda}}\right\}$$

$$C_{f2} = C_f \left\{\frac{\sin(\tilde{\alpha}) + \cos(\tilde{\alpha}) \tan(\beta)}{\sin \tilde{\lambda}}\right\} . \qquad (4.2.9)$$

Following Smith we use the Ludwieg-Tillmann relation for the skin friction magnitude, C_f, modified for compressible flow according to Eckert's reference temperature concept, viz,

$$C_f = .246 \left(\frac{\rho_e u_e \theta_{11}}{\mu^*}\right)^{-.268} \left(\frac{T_e}{T^*}\right) 10^{-.678\bar{H}} \qquad (4.2.10)$$

where $T^*/T_e = 1 + .13\ M^2$ for adiabatic flow in air and the coefficient of viscosity μ^* is evaluated at the temperature T^* by

$$\left(\frac{\mu^*}{\mu_e}\right) = \left(\frac{T^*}{T_e}\right)^{.89} .$$

The final form of Eq (4.2.4), (4.2.5), and (4.2.6) together with the lag-entrainment differential equation for the entrainment coefficient F, can be expressed in the form,

$$A_{ij} \frac{\partial u^j}{\partial x} + B_{ij} \frac{\partial u^j}{\partial y} = C_i \qquad (4.2.11)$$

and $u^j = \begin{bmatrix} \theta_{11} \\ \bar{H} \\ \gamma \\ F \end{bmatrix}$

The characteristics of the quasilinear system of four partial differential equations and their solution are discussed in the following subsections.

4.2.2 Characteristics & Compatibility Equations

The equation for the entrainment coefficient F in Eq (4.2.11) is of the form,

$$\frac{DF}{Dt} = \psi$$

where

$$\frac{D}{Dt} = \left(\frac{u_1}{h_1} \frac{\partial}{\partial x} + \frac{v_1}{h_2} \frac{\partial}{\partial y}\right)$$

The x and y derivatives of F at any point can be computed and are decoupled from the derivatives of θ_{11}, $\bar{H}$, and γ. Furthermore, the characteristic curve for F is the external inviscid streamline. Equations for θ_{11}, $\bar{H}$, and γ are coupled, viz,

$$a_{ij} \frac{\partial v^j}{\partial x} + b_{ij} \frac{\partial v^j}{\partial y} = \phi_i \qquad (4.2.12)$$

with $v^j = \begin{bmatrix} \theta_{11} \\ \bar{H} \\ \gamma \end{bmatrix}$, $a_{ij} \neq b_{ij} \neq \phi_i \neq 0$ for $i = 1,2,3$. Multiplying each component of Eq (4.2-12) by μ_i and summing, we have,

$$(\mu_1 a_{11} + \mu_2 a_{21} + \mu_3 a_{31})\left(\frac{\partial \theta_{11}}{\partial x} + \lambda \frac{\partial \theta_{11}}{\partial y}\right)$$
$$+ (\mu_1 a_{12} + \mu_2 a_{22} + \mu_3 a_{32})\left(\frac{\partial \bar{H}}{\partial x} + \lambda \frac{\partial \bar{H}}{\partial y}\right) \qquad (4.2.13)$$
$$+ (\mu_1 a_{13} + \mu_2 a_{23} + \mu_3 a_{33})\left(\frac{\partial \gamma}{\partial x} + \lambda \frac{\partial \gamma}{\partial y}\right) = (\mu_1 \phi_1 + \mu_2 \phi_2 + \mu_3 \phi_3)$$

with

$$\lambda = \frac{\mu_1 b_{11} + \mu_2 b_{21} + \mu_3 b_{31}}{\mu_1 a_{11} + \mu_2 a_{21} + \mu_3 b_{31}} = \frac{\mu_1 b_{12} + \mu_2 b_{22} + \mu_3 b_{32}}{\mu_1 a_{12} + \mu_2 a_{22} + \mu_3 a_{32}} = \frac{\mu_1 b_{13} + \mu_2 b_{23} + \mu_3 b_{33}}{\mu_1 a_{13} + \mu_2 a_{23} + \mu_3 a_{33}} \qquad (4.2.14)$$

The system of homogeneous equations Eq (4.2.14) has nontrivial solution for μ_1, μ_2, and μ_3 if and only if,

$$\mathrm{Det}|b_{ij} - a_{ij}\lambda| = 0 \qquad (4.2.15)$$

The solution for λ from the cubic equation has been studied rather extensively (Ref. 40) in conjunction with the development of the integral methods of 3-D turbulent boundary layers. At any point (x,y), λ is the tangent of the angle between the characteristic line and the x-axis. For incompressible flow, the form of the characteristic equation is particularly simple as shown by Myring. It was shown that for a well behaved boundary layer Eq (4.2.15) possesses three distinct real roots, therefore the system of differential equations is totally hyperpolic. The three characteristic lines lie between the external streamline and the limiting wall streamline of the boundary layer flow. Numerical solutions of Eq (4.2.15) carried out by us have shown that this property is also true for compressible flow. It has been shown by Cousteix and Houdeville in Ref. 36 that the behavior of solutions to the 3-D turbulent boundary layer equations is strongly effected by the hyperbolic character of the governing partial differential equations and by the nature of

the associated characteristic curves in the plane of the wing. As noted by them, when solved in the direct mode with the pressure distribution prescribed, the equations admit weak solutions in which the characteristics of the same family may intersect each other on certain singular lines. The singular lines are analogous to shock waves across which the displacement thickness and other boundary layer properties are discontinuous. Such solutions have no physical significance and should not be identified with the separation lines observed in 3-D boundary layer separation. The jumps in displacement thickness leads to large (actually unbounded) values of the transpiration velocity which will act, through viscid/inviscid interaction mechanisms, to significantly alter the inviscid flow and streamline pattern near such singular curves. Since discontinuous solutions of this type cannot be self-consistent solutions of the coupled viscid/inviscid equations, it is clear that the interaction must eliminate the characteristic crossings and the associated discontinuities from the solution. One can speculate that the singular crossing curves are transformed through a strong local interaction, to an envelop of streamlines that could be identified with the locus of the 3-D separation. Cousteix and Houdeville also proposed an inverse method for avoiding the discontinuous solutions of the direct problem. In their method, which was aimed at noninteracting type computations, they proposed specifying two integral thicknesses and computing the pressure distribution as part of the solution of the boundary layer equations.

Unfortunately, although inverse methods may be useful for avoiding the shock line jumps in 3-D boundary layer solutions, they do not eliminate all problems faced in computing separated 3-D boundary layers. Indeed the major difficulty in computing such flows seems to be associated with the turning of the limiting streamlines and characteristics to a direction perpendicular to the marching direction and not with the formation of discontinuous weak solutions. In these cases the curved streamlines seem to form a "sonic" envelope across which the solution cannot be continued. This is so mainly because the flow upstream of such envelopes do not lie in the domain of dependence of the initial data line from which the solution was initiated. Although the details are far from understood, it seems clear that such envelopes are likely to be relocated in some way to 3-D separation lines. The computation of 3-D boundary layers in these circumstances is extremely difficult because of the need to supply initial data some place downstream of

the envelope and it is not at all clear at present how this can be done. Because of the uncertainty in how to proceed in such cases, in our approach we employ a standard direct method to treat the viscid/inviscid coupling.

If we assume there exists a solution of Eq (4.2.15) for the eigenvalues $\lambda = \lambda_i$ for i = 1,2,3, at any point (x,y_n) on the wing surface or in the wake, it follows that Eq (4.2.13) can be expressed in the form,

$$(a_{11} + \mu_{2i}a_{21} + \mu_{3i}a_{31})\left(\frac{\partial\theta_{11}}{\partial x} + \lambda_i \frac{\partial\theta_{11}}{\partial y}\right) + (a_{12} + \mu_{2i}a_{22} + \mu_{3i}a_{32})\left(\frac{\partial\bar{H}}{\partial x} + \lambda_i \frac{\partial\bar{H}}{\partial y}\right)$$

$$+ (a_{13} + \mu_{2i}a_{23} + \mu_{3i}a_{33})\left(\frac{\partial\gamma}{\partial x} + \lambda_i \frac{\partial\gamma}{\partial y}\right) = \phi_1 + \mu_{2i}\phi_2 + \mu_{3i}\phi_3 \qquad (4.2.16)$$

where,

$$\mu_{2i} = [-(b_{11} - a_{11}\lambda_i)(b_{32} - a_{32}\lambda_i) + (b_{12} - a_{12}\lambda_i)(b_{31} - a_{31}\lambda_i)]/D_i$$

$$\mu_{3i} = [-(b_{21} - a_{21}\lambda_i)(b_{12} - a_{12}\lambda_i) + (b_{11} - a_{11}\lambda_i)(b_{22} - a_{22}\lambda_i)]/D_i$$

and

$$D_i = (b_{21} - a_{21}\lambda_i)(b_{32} - a_{32}\lambda_i) - (b_{31} - a_{31}\lambda_i)(b_{22} - a_{22}\lambda_i)$$

for i = 1,2,3.

Equations (4.2.16) are the compatibility equations of the hyperbolic equations in their "normal characteristic form". The solution of Eq (4.2.16) could be carried out most naturally with a "λ type-scheme" (Ref. 45). For interior points, $y = y_n$, the y derivatives of θ_{11} $\bar{H}$ and γ associated with each λ_i factor are evaluated using values of θ_{11} etc. at (x, y_{n+1}) and (x, y_n) when $\lambda_i < 0$ and using values at (x,y_n) and (x, y_{n-1}) when $\lambda_i > 0$, where $y_{n+1} > y_n > y_{n-1}$. The x-derivatives of θ_{11}, $\bar{H}$, and γ then are computed using Eq (4.2.16) and new values of θ_{11}, $\bar{H}$, and γ are obtained by an explicit marching scheme. There is a fundamental problem that arises with any method of integration associated with the implementation of the boundary conditions. The integration domain lies between the wing root and tip stations. It is seen that when $\lambda_i > 0$ at $y = y_{\text{wing root}}$ or when $\lambda_i < 0$ at $y = y_{\text{wing tip}}$, boundary conditions are required to supplement the compatability equations, Eq (4.2.16) at these stations. According to the rules in Kreiss

(Ref. 46), the total number of boundary conditions and compatibility equations should be equal to the order of the system of equations. The number of boundary conditions required at $y = y_{\text{wing root}}$, for example, is exactly the number of roots for which $\lambda_i > 0$. It is not clear at this stage how to properly determine these conditions. Our study indicates that computed results are very sensitive to the boundary conditions prescribed at the wing root and tip. For numerical convenience, in our method we employ zero spanwise gradient conditions. These conditions are non-physical and lead to errors in the region lying in the domain of dependence of the wing tip or body juncture points. Further study is clearly called for to determine correct procedures for setting these boundary conditions.

4.2.3 Numerical Integration of Boundary Layer Equations

In view of the difficulty in imposing boundary conditions in the λ-scheme, a less accurate but reliable numerical integration scheme is adopted for the solution of the system of Eq (4.2.11). The same procedure is also used to integrate the laminar boundary layer equations. The method, first used by Smith, solves, first, at a constant x line, for the x derivatives of θ_{11}, $\bar{H}$, γ, and F. Then a two-level explicit integration scheme is used for integration in the x-direction. A local C.F.L condition is imposed to determine the maximum integration step Δx. The y derivatives of the dependent variables θ_{11}, $\bar{H}$, γ, and F are evaluated in such a way that the rules of domain of dependence and region of influence are not violated. Since the characteristic lines lie either on (as in the case of characteristics for F) or within an angle bounded by the external inviscid streamline (with an angle of inclination $\tilde{\alpha}$ with respect to the x-axis) and the limiting wall streamline (with an angle of inclination of $\tilde{\alpha} + \beta$ with respect to the x-axis), the use of these two directions to predict the directional bias of the disturbances always produces a conservative estimate of the step size to be used. We denote by (x, y_n) the location of the point where the y derivatives are to be evaluated and by (x, y_{n-1}), (x, y_{n+1}) the two neighboring points where $y_{n+1} > y_n > y_{n-1}$. The y derivative $\frac{\partial \bar{H}}{\partial y}\Big|_{x,y_n}$ (or, similarly for the other derivatives $\frac{\partial \theta_{11}}{\partial y}\Big|_{x,y_n}$, $\frac{\partial \gamma}{\partial y}\Big|_{x,y_n}$, $\frac{\partial F}{\partial y}\Big|_{x,y_n}$) is determined according

to the signs of the angles $\tilde{\alpha}$ and $\tilde{\alpha} + \beta$. If both $\tilde{\alpha}$ and $\tilde{\alpha} + \beta$ are positive, a backward difference of the form

$$\frac{\partial \bar{H}}{\partial y}\Big|_{x,y_n} = \frac{(\bar{H})_{x,y_n} - (\bar{H})_{x,y_{n-1}}}{y_n - y_{n-1}}$$

is used. If both $\tilde{\alpha}$ and $\tilde{\alpha} + \beta$ are negative, a forward difference of the form

$$\frac{\partial \bar{H}}{\partial y}\Big|_{x,y_n} = \frac{(\bar{H})_{x,y_{n+1}} + (\bar{H})_{x,y_n}}{y_{n+1} - y_n}$$

is used. And if $\tilde{\alpha}$ and $\tilde{\alpha} + \beta$ are of opposite sign, a central difference of the form

$$\frac{\partial \bar{H}}{\partial y}\Big|_{x,y_n} = \frac{(\bar{H})_{x,y_{n+1}} - (\bar{H})_{x,y_{n-1}}}{y_{n+1} - y_{n-1}}$$

is used. For the wing tip points, all the y derivatives are set equal to zero unless both $\tilde{\alpha}$ and $\tilde{\alpha} + \beta$ are positive and in this case a backward difference formula is used. For the wing root points, all the y derivatives are set equal to zero unless both $\tilde{\alpha}$ and $\tilde{\alpha} + \beta$ are negative and a forward difference formula is then used.

The integration can be started with either laminar boundary layer equations or turbulent boundary layer equations at or near the leading edge lines of the wing. Because the integration must follow the flow direction, the starting point must necessarily be downstream of the forward stagnation line. For calculations with a laminar boundary layer start, one must either impose the location of transition to turbulent flow or use a natural transition criterion to fix the transition position. In the present code we assign the transition point locations unless the laminar boundary layer solutions indicates separation, in which case we assign transition to the point of laminar separation. When transition occurs, the momentum thickness θ_{11} is assumed to be continuous across transition and the shape factor, $\bar{H}$, is assigned a value of 1.45 (an alternative to this is to assign a local jump in the value of $\bar{H}$ equal to $\Delta\bar{H}_{Transition}$ as determined by experiments (Ref. 47)).

The 3-D boundary layer integration is extended into the wake in a manner similar to the 2-D calculation of Green et al. The skin friction C_f is set equal to zero, and the dissipation length used in Green's formulation is set equal to half of that of the boundary layer value. Since Johnston's (Ref. 44) cross flow profile cannot admit a zero friction solution, only Mager's (Ref. 43) crossflow profile can be used in the wake. In this case, $\gamma = \beta$.

Since the information of the characteristic lines is helpful in understanding the boundary layer flow behavior, the eigenvalues from the solution of Eq (4.2.15) are computed at each step of integration. For example, a very large value of λ or appearance of imaginary roots of Eq (4.2.15) usually indicates the incipient breakdown of the computation.

4.2.4 Special Considerations

Since the solution procedure of the boundary layer equations as described in the previous sections is only an intermediate step of reaching the converged solution of the viscid-inviscid interaction, one does not always have a smooth inviscid pressure distribution for each cycle of the boundary layer computation. It is important in our iterative method to establish a procedure for preventing a breakdown of the boundary layer computation from the appearance of an unphysical intermediate inviscid pressure distribution. Our numerical experiments indicate that a computational breakdown associated with large inviscid pressure gradients is often started by a rapid local growth of the shape factor H. When this happens we set a maximum cutoff value of 2.4 for H and set the local y derivatives of the dependent variables equal to zero. The computed boundary layer solution of the shape factor H usually reaches a maximum at the trailing edge and drops off gradually going downstream into the wake. Occasionally, the computed value of H may drop to below 1 far downstream in the wake. These physically unrealistic values lead to numerical difficulties in the far field. To avoid such problems, we set a lower bound of $H = 1.05$ in the far field and continue the wake computation using a strip boundary layer approximation with all spanwise derivatives set to zero.

Additional numerical difficulties may also arise because the streamwise momentum thickness, θ_{11}, may occasionally drop below zero on the wing surface. The basic code would usually break down at such points because of appearance of a logarithm of θ_{11} in the computation of the skin friction from

the Ludwieg-Tillman formula. We have found, that in these cases the solution can usually be continued downstream using a strip boundary layer approximation with all spanwise derivatives set to zero. The program has been setup to do this if negative values of θ_{11} should arise at any stage of the computation.

As mentioned in Subsection 4.2, we compute the metric coefficients $h_1(x,y)$, $h_2(x,y)$ and $g(x,y)$ taking full account of the wing thickness and wake curvature. This more accurate treatment of the geometry turns out to be important near leading and trailing edges and acts to provide smoother, more accurate boundary layer solutions in these regions. To demonstrate this, we have computed two boundary layer solutions, one with our full metric coefficients expressions and the other with the metric coefficients for a corresponding flat wing. The computations are for the Lockheed Wing A at a Mach number $M_\infty = .796$, angle of attack $\alpha = 1.94$ and reference Reynolds number of 5 million. The two solutions for the shape factor, H, are shown in Fig. 9. It is seen that there are significant differences in the two solutions with the one using the full metric coefficients expressions showing milder gradients and a much lower peak value towards the trailing edge as compared with that of the flat wing solution. This behavior is generally true for the solution of all the other dependent variables.

4.3 ITERATIVE SOLUTION TO VISCID-INVISCID INTERACTION ANALYSIS

The inviscid and boundary layer solution procedures described in Subsections 4.1 and 4.2, must be modified to accomodate the matching conditions coupling the viscid and inviscid flows. In this subsection, we describe how the viscous coupling conditions are incorporated into the solution of the inviscid equations and we also outline the interative procedure used to solve the coupled viscid/inviscid equations.

4.3.1 Transpiration Coupling Conditions for Inviscid Flow Boundary Conditions

The boundary conditions for the finite volume formulation of the inviscid flow analysis need to be modified in order to take into account the boundary layer displacement and viscous wake effects. Transpiration boundary conditions are used in the present work. In 3-D flow, the surface source velocity, m, is related to the displacement thickness, δ^*, by the entrainment relation, Eq (4.2.7), which can be written in the form,

$$m = \left(\frac{u_1}{h_1}\right)\left(\frac{\partial \delta^*}{\partial x} + P\delta^* + \frac{h_1}{h_2}\frac{v_1}{u_1}\frac{\partial \delta^*}{\partial y}\right) \qquad (4.3.1)$$

where

$$P = \frac{h_1}{q}\frac{\partial}{\partial x}\left(\frac{q}{h_1}\right) + \frac{1}{u_1}\frac{\partial u_1}{\partial x} + \frac{v_1}{u_1}\frac{h_1}{q}\frac{\partial}{\partial y}\left(\frac{q}{h_2}\right)$$

$$+ \frac{h_1}{h_2}\frac{1}{u_1}\frac{\partial v_1}{\partial y} - \frac{M^2}{u_e}\left(\frac{\partial u_e}{\partial x} + \frac{h_1}{h_2}\frac{v_1}{u_1}\frac{\partial u_e}{\partial y}\right)$$

The displacement thickness, δ^*, is defined by

$$\delta^* = \int_0^{\delta} \frac{(\rho_e u_e - \rho U)}{\rho_e u_e}\, dz$$

where ρU is the mass flux in the boundary layer in the external flow direction. The external quantities at the boundary layer edge, are Mach number (M), density (ρ_e), and the total velocity (u_e). The velocity components u, v, are components of u_e along x, y, the boundary layer nonorthognal curvilinear coordinates. The quantities h_1, h_2, are the metric coefficients and q is equal to

$$q = [h_1^2 h_2^2 - g^2]^{1/2}$$

The displacement thickness is determined as part of the boundary layer solution as described in Subsection 4.2. From Eq (4.3.1), therefore, the source, m, can be computed at each step of the boundary layer integration. The boundary conditions for the inviscid flow require the values of m at the midpoints of the inviscid mesh, which can be obtained by interpolation. Since the finite volume formulation is being used for the inviscid flow analysis, m is to be converted into M, its corresponding contravariant flux vector across the body surface. The scaling factor between m and M is quite complex and is not given here. It can be shown that for 2-D problem, $M = m \cdot ds$, where ds is the arc length between the two nodal points of the inviscid mesh. With the known distribution of the sources and its equivalent source jump in the wake (the difference of sources from top and bottom of the wake), the inviscid flow boundary conditions are modified as follows.

Referring to Fig. 10, the velocity potential, G, at the span station Z = Z_K of the inviscid flow is to be computed. The value of G at Z = Z_{K+1} is lagged and computed from the previous iterate. The contravariant fluxes are to be computed at cell centers. On the boundary, A and E are the last points of the wake across the sheet, B and D are the trailing edge points and C is the leading edge point. On the wing surface (i.e., D - C - B) the reflection condition of the normal component of the contravariant fluxes, VM and VP, of the inviscid flow computation is modified due to the sources generated by the boundary layer,

$$VM(I) + VP(I) = \frac{1}{2}(\rho_M + \rho_P) \cdot M \qquad (4.3.2)$$

where ρ_M and ρ_P are the densities computed at the two cells near the boundary and between the two space stations. The tangential components of the contravariant fluxes UM(I) = UP(I), WM(I) = WP(I) etc remain the same as those of the noninteractive computation. On the wake (i.e., from E to D and from B to A) the flux conditions are not changed from the noninteractive computation because the image conditions have to be imposed, viz:

$$\begin{aligned} UM(I) &= - UP(M) \\ VM(I) &= - VP(M) \\ UM(M) &= - UP(I) \\ VM(M) &= - VP(I) \quad \text{etc} \end{aligned} \qquad (4.3.3)$$

where I and M are the respective image points across the wake sheet. The adding (or subtracting) of sources, however, is reflected in the mass flux balance equation (the continuity equation). Therefore, the residual formula evaluated at the nodes both on the wing and wake surfaces are modified to account for the mass injection from the boundary layer. Particular attention is paid to points D and B where there are source contributions both from the wing side and the wake side of the trailing edge.

4.3.2 Wake Curvature Effects

In Subsection 4.1, we described the procedure for adjusting the mesh to follow the wake stream surface of the inviscid solution. In the inviscid computation, the wake surface was updated at each cycle of the inviscid iteration. In the viscous computation it was found to be more efficient to update the wake position before each boundary layer computation rather than at

each inviscid cycle. In the viscous computation the wake position is defined in terms of a wake angle, $\tilde{\beta}$,

$$\tan \tilde{\beta} \Big|_{Z=Z_K} = \frac{dY}{dX}\Big|_{Z=Z_K} = \frac{\bar{V}}{\bar{U}} \Big|_{Z=Z_K}$$

where X, Y are the Cartesian wake coordinates, $\tilde{\beta}$ is the wake line angle with respect to X-axis at constant $Z = Z_K$, $\bar{U}$ and $\bar{V}$ are the inviscid velocity components, averaged between the top and bottom of the wake surface, along X and Y-axes, respectively.

The wake curvature effect terms are imposed in the following manner. Referring to Fig. 10, let the row of computation nodes at the wake, above the wake and below the wake at a spanwise station, $Z = Z_K$, be denoted by (I,KY,K), (K,KY-1,K), (I,KY+1,K), respectively, and let (M,KY,K) etc. be the image nodes across the wake. The Kutta condition and the wake curvature condition can be imposed according to the following formulae, for the surface wake nodes,

$$G(M,KY,K) = G(I,KY,K) + CIRC(K) + \Gamma \tag{4.3.4}$$

and for the image wake nodes,

$$G(M,KY+1,K) = G(I,KY-1,K) + CIRC(K) + \Gamma \tag{4.3.5a}$$

$$G(I,KY+1,K) = G(M,KY-1,K) - CIRC(K) - \Gamma \tag{4.3.5b}$$

The function G is the reduced velocity potential, CIRC(K) is the trailing edge velocity potential jump determined by the Kutta condition and Γ, the circulation, is equal to the jump in velocity potential across the wake. The circulatory function, Γ, is determined by the matching conditions coupling the viscid and inviscid flows. Within standard boundary layer theory it can be written in the form,

$$\Gamma(s)\Big|_{Z=Z_K} = -\left[\int_{\tilde{\beta}_{te}} \bar{Q}(\tilde{\delta}^* + \tilde{\theta}_{11})d\tilde{\beta}\right]_{Z=Z_K} \tag{4.3.6}$$

where $\bar{Q}$ is the average surface value of the outer inviscid velocity in the chordwise direction, $\tilde{\delta}^*$ and $\tilde{\theta}_{11}$ are the respective sums of the upper and lower displacement and momentum thicknesses, respectively. Our method incorporates corrections to the standard coupling conditions to account for strong interaction effect at trailing edges. These corrections modify the standard expression for Γ given above, as described in the following section.

4.3.3 Trailing Edge Corrections

In our method we incorporate strong interaction effects at trailing edges into our basic viscid-inviscid coupling procedures. We follow closely the procedures developed for the 2-D airfoil problem as described in Ref. 6. In that work a local asymptotic solution is developed which describes the strong interaction effect at trailing edges. Through the use of this solution, modifications to the classical coupling conditions are developed to take into account normal pressure gradient effects across the boundary layer in the trailing edge region. The theory of Ref. 6 was for a strictly 2-D flow. In the present work, we adapt the 2-D corrections of Ref. 6 to the wing problem considered in this study using a quasi-2-D approximation. In this approach, we simply apply the 2-D corrections to the full 3-D form of the classical coupling conditions assuming the flow is 2-D in streamwise planes. The use of a 2-D strip approximation is justified because the flow gradients normal to the trailing edge are asymptotically larger compared to gradients in the spanwise direction and the local analytic solution will be 2-D under these circumstances except the near wing tip and body juncture stations. To be consistent for swept trailing edges, the quasi-2-D theory should be applied in a direction normal to the trailing edge. However, for simplicity we apply the theory in the streamwise direction. Since the corrections are relatively small we believe the simple theory will be adequate except, perhaps, for very highly swept trailing edges.

In the modified theory, corrections are applied to the standard coupling conditions to account for normal pressure gradient effects. The corrections are applied to 1) the source velocity on the wing surface, 2) the jump in source velocity in the wake and 3) the jump in pressure or velocity potential (i.e., Γ) across the wake. In addition, the surface pressure computed from the inviscid solution is corrected to account for the pressure drop across the boundary layer in the trailing edge region. The corrected boundary

conditions, following from Ref. 6, are written in the form:

Source velocity:

$$m(s,Z_K) = m_\sigma(s,Z_K)\ [\sqrt{(s-s_{te})}\ K(s,Z_K)] \qquad \text{wing section} \qquad (4.3.7a)$$

$$[m(s,Z_K)] = [m^+(s_{te},Z_K)\ \bar{K}^+(s,Z_K)\ -m^-(s_{te},Z_K)\bar{K}^-(s,Z_K)] + m_w(s,Z_K)$$

$$\text{wake} \qquad (4.3.7b)$$

Wake Circulation:

$$\Gamma(s)|_{Z=Z_K} = -\left[\int_{\tilde{\beta}_{te}} \bar{Q}\ (\tilde{\delta}^* + \tilde{\theta}_{11})\ \sqrt{(s-s_{te})}\ J_w(s)d\tilde{\beta}\right]_{Z=Z_K} \qquad (4.3.7c)$$

where m_σ (s, Z_K) and m_w(s, Z_K) are the classical expressions for the source velocity on the wing at section Z = Z_K and the jump in source velocity in the wake, m^+ (s_{te}, Z_K) and m^- (s_{te}, Z_K) are the values of the corrected source velocities on the upper and lower surfaces of the wing section at the trailing edge, s is the arc length along the wing section and wake. The functions K(s, Z_K), $\bar{K}(s,Z_K)$ and $J_w(s)$ are given in terms of universal functions from the local trailing edge solution in Ref. 6. The corrected pressure distribution in the wake is given by an expression of the form

$$P_e(s,Z_K) = P_e^+(s,Z_K) - \frac{\Lambda}{1+\Lambda}\ [\ P\ ] \qquad (4.3.8)$$

where $P_e(s,Z_K)$ is the corrected pressure distribution on the wake, $P_e^+(s,Z_K)$ is the inviscid solution for the pressure on the upper surface of the wake and [P] is the difference in pressure across the wake from the inviscid solution. The jump in pressure in the inviscid solution is caused by the wake boundary condition imposing the jump in velocity potential, Γ, across the wake. The quantity Λ is also given in terms of universal functions in Ref. 6. The expression for the pressure distribution on the wing section surface is written in the form,

$$P_e(s,\ Z_K) = P_e(s,\ Z_K) - [\ p\ ]_{te}\ \bar{I}(s,\ Z_K) - \rho_e Q_e^2\ p_\sigma(s,\ Z_K) \qquad (4.3.9)$$

where $P_e(s, Z_K)$ and $P_e(s, Z_K)$ are the corrected and inviscid surface pressure distributions respectively, $[\ P\ ]_{te}$ is the jump in inviscid pressure across the wake evaluated at the trailing edge. The quantity $\bar{I}(s, Z_K)$ is a universal function given from the local trailing edge solution and $p_\sigma(s, Z_K)$ is the pressure correction determined from the classical boundary layer theory as described in Ref. 6.

4.3.4 Global Iteration Strategy for the Interaction Solution

The solution procedure for the global iteration is carried out in the following steps,

I. Obtain the inviscid 3-D solution using the AFZ scheme, compute the surface velocities and surface flow angles.

II. Compute the corrected surface velocities and surface flow angles as indicated in the previous subsection.

III. Obtain the 3-D boundary layer and wake solution using the modified surface velocities and flow angles from the previous step.

IV. Compute the coupling condition as follows:

1. Compute the surface source velocity distribution and its contravariant equivalent from the boundary layer solution.

2. Compute the floating wake surface coordinates using the inviscid velocities, and obtain the equivalent shear function used in the inviscid parabolic coordinate mapping.

3. Compute the wake jump condition from the updated wake coordinates.

V. Go to step I.

There are two sets of relaxation factors assigned to the calculations, the P_i, i = 1,2,3, for the inviscid solutions and the relaxation factors V_i, i = 1,2,3,4, for the boundary layer source flux on the wing, the viscous wake source flux, the floating wake coordinates and the velocity potential jump for the wake curvature effect. The chosen values of P_i are based solely upon the best convergence behavior of the inviscid calculation. The values of V_i range from .5 to 1. Since the inviscid AFZ scheme requires four sweeps per one outer cycle of iteration, the boundary layer calculations are updated after

multiples of four sweeps of the inviscid iteration. Eight sweeps of inviscid iterates are chosen between boundary layer calculations for our computations.

Our experience indicates that the inviscid part of the program is quite robust and convergence has been achieved for quite a broad range of test cases including wings of practical interest. The major requirement for a successful convergence calculations for the viscous wing program during a global iteration is the avoidence of boundary layer computation breakdown. For a modern transonic wing with large trailing edge camber and wing twist, large inviscid pressure gradients can cause a breakdown of the boundary layer computation at the outset. Since viscous effects generally smooth out these large pressure gradients, such breakdowns in the initial stages of the computation do not necessarily imply that a converged solution cannot be obtained. Some practical techniques can be used to achieve convergence. For example, if the computational problem is the result of too strong an inviscid shock locally, the iteration can be initiated at a lower freestream Mach number to achieve an intermediate convergence, then the Mach number is progressively increased to the desired value. On the other hand, if the difficulty in obtaining a boundary layer solution is due to the complexity of the camber variation and wing twist, it is desirable to start the iteraction at a low angle of attack which is then increased to the desired value. These techniques shall be implemented in future versions of the code.

With a given wing geometry, a given case requires the specification of the free stream Mach number M_∞, the angle of attack, α, and the reference Reynolds number Re_{ref}. Numerical computation is performed with an assigned mesh and sets of relaxation parameters P_i and V_i. In addition, the boundary layer transition location needs to be assigned. An improperly assigned transition location can lead to erroneous results, as shall be discussed in detail in the next section. A typical converged interaction calculation for a supercritical flow case takes about 10 to 20 boundary layer cycles of computation dependent on the relative difficulty of the case. Normally it takes about eight cycles of boundary layer computation to reduce the maximum inviscid residual to less than 10^{-5}.

The convergence history of a typical case run for the Lockheed Wing A is shown in Fig. 11. The free stream Mach number used was $M_\infty = .82$, the angle of attack $\alpha = 1.5°$, reference Reynolds number $Re_{ref} = 18 \times 10^6$, and grid

distribution (160 x 16 x 32). The wing root circulation value and the total number of supersonic points are plotted as a function of iteration numbers. The CPU time required for the total thirty cycles of boundary layer calculations is about eight minutes using a Cray-1S computer.

5. RESULTS

5.1 NUMERICAL RESULTS - INVISCID FLOW

Results for the ONERA M6 wing of Fig. 12 are illustrated in Fig. 13 through 22. For $M_\infty = .923$, $\alpha = 0$, the computed C_p distribution is given in Fig. 13. It can be seen that there is a large supersonic zone with shocks extending over the length of the wing. A comparison with experiment near mid-span is given in Fig. 14. From Fig. 15 it can be seen that the solution is well converged after 32 iterations. Figure 16 compares the convergence history of the average residual for two variations of the present AFZ method with a relaxation (SLOR) method. The development of the supersonic zone for the three methods is shown in Fig. 17. Figure 16 seems to indicate that SLOR exhibits a faster convergence at the beginning of the iteration. This effect is even more pronounced in the lifting case to be considered later (Fig. 21). The convergence of SLOR slows down significantly after the first 50 iterations while the AF schemes maintain a steady and rapid convergence rate. The advantages of the AF scheme shows up even more clearly when considering the convergence of the global aspects of the solution such as the number of supersonic points (Fig. 17) and the lift (Fig. 22).

Figures 18 through 22 give results for the same wing (Fig. 12) at $M_\infty = .84$ and $\alpha = 3.06°$. Figure 18 shows the upper and lower surface pressures. It can be seen that the two shocks (one near the leading edge, the other further back) come together as the wing tip is approached. Figure 19 shows a comparison with experimental surface pressures, at a spanwise section near mid-span. Figure 20 shows the convergence in surface pressure. Figure 21 shows the convergence history in terms of average residual. Again it seems that SLOR has a faster initial convergence rate, but considering Fig. 22 (development of lift) the advantage of the AF schemes is obvious.

The computation of the inviscid transonic flow about transport type wings like the ONERA M6 is relatively straightforward. This is because these wings are characterized by high aspect ratios, low sweep, small twist and similar airfoil sections. The 3-D effects in the flow field about these types of wings are minimal. The results of Fig. 23 and 24 are intended to demonstrate the capability of the inviscid code for computing the flow about highly 3-D

wings. Figure 23a shows a 3-D view of a low aspect ratio, highly swept and twisted wing. The flow field about this wing was computed at a free stream Mach number, $M_\infty = .9$ and an angle of attack, $\alpha = 8°$. The surface pressure distribution at three sections are shown in Fig. 23b, 23c, and 23d. Figure 23b shows the root airfoil section and the corresponding surface pressure. The section lift at this station is small because of the lower relative incidence. Figure 23c shows computed results at the mid-span section. The section load here is higher than that at the root although the section is twisted down relative to the root. This effect is due to the upwash from the root section caused by the large sweep of the wing. This effect is even more pronounced at the tip section (Fig. 23d) where the large relative incidence (due to upwash) causes a strong shock at the leading edge.

Figure 24a shows the planform and surface isobars for another wing. This wing was also run at a Mach number of $M_\infty = .9$ and $\alpha = 8°$. The isobars clearly show a two shock pattern before the crank in the trailing edge. The leading edge and trailing edge shock waves interact near the wing tip. Figure 24b shows the airfoil section and surface pressure at the root of the wing. Figure 24c shows the mid-span section where the two shocks can be seen clearly. Figure 24d shows the tip section after the two shocks have interacted. The leading edge camber of the outboard sections of this wing is shown in Fig. 24d. The effect of leading edge camber, in eliminating strong leading edge shocks, is demonstrated dramatically by comparing Fig. 24d and 23d. Both these wings are highly 3-D and heavily loaded at their tips. These conditions usually require adjustments in the parameters of the AFZ inviscid code. For these more difficult cases the iteration procedure should be underrelaxed somewhat, particularly for fine grids. The fact that converged solutions could be achieved in these very difficult cases indicates the soundness of our basic AFZ scheme.

A comparison of convergence rates using the two far field boundary conditions mentioned in Subsection 3.1 is shown in Fig. 25. In the figures the solid line was computed using the expansion of the Prandtl-Glauert equation (Eq 3.1.8) the dashed line was computed using the original condition $\phi = 0$ upstream and $\phi_\chi = 0$ far downstream. Figure 25a shows how convergence is improved using the new far field condition. Figure 25b shows that the lift is increased significantly with the new condition. The computed lift using our

Prandtl-Glauert far field boundary condition Eq (3.1.8) seems less sensitive to the location of the far field boundary (i.e., less sensitive to the parameter BOUND). The results of Fig. 25 were computed with a BOUND of .95 which places the outer boundary about 6 cords from the wing.

Figure 26 shows a comparison of computed results using the first and second order artificial viscosities. Figure 26a shows these convergence rates. The figure shows that the convergence is slowed using the second order scheme. Figures 26b-26j shows sectional surface pressure distributions from the root to tip. The figures show that the pressure distributions are all sensitive to the choice of the artifical viscosity formula. The shock in the second-order results is sharper (for example, see Fig. 26g) and the suction peak near the leading edge is significantly reduced. The lift is increased from C_L = .635, first order, to C_L = .665, second order.

5.2 VISCOUS INTERACTION RESULTS

In this subsection, we present results computed from the viscous wing program. The computer program developed for the present program is designated GRUMWING. The present version of the code is a pilot code which we expect to further develop into a production code. The inviscid results presented earlier in this Section were computed with the inviscid option of the GRUMWING program. Details of this program are given in the user's manual included as the second volume of the report.

The results presented in this section were obtained for the Lockheed Wings A and B described in the report of Hinson and Burdges (Ref. 48). Of particular significance in their work is the fact that special attention had been paid to the effects of the fuselage on wing pressure data so that meaningful comparisons can be made for an analysis method with wing alone. Shown in Fig. 27 and Fig. 28 are the wing planform and wing airfoil sections for the Wing A and the Wing B, respectively. Wing A is a transonic wing of transport type. It has an aspect ratio of 8, and quarter chord sweep of 25°. Wing B is a fighter type wing designed for transonic cruise. It has an aspect ratio of 3.8, and quarter chord sweep of 30°. The nominal test Reynolds number for the experiments based on the mean aerodynamic chord was Re = 6 x 10^6 for Wing A and Re = 10 x 10^6 for Wing B.

5.2.1 Boundary Layer Transition Assignment

It has been known that inappropriately selected transition points can lead to unrealistic results even when the computation proceeds without any apparent difficulty. In this section we show results of computations with varying transition point locations that give some indications of the sensitivity of the solution to the choice of transition point location.

In order to demonstrate the effects of the transition point locations on the solution, computations were carried out for a variety of transition locations for the Lockheed Wing A at $M_\infty = .82$, $\alpha = 1°$, $Re = 5 \times 10^6$ using a (160 x 16 x 32) grid. Shown in Table 1 are the transition results for runs using assigned transition locations of 0, 2.5, 5, 7.5, and 10% chord, on the upper and lower surfaces. For the last case laminar separation occurs on the upper surface at 8.2% chord. For this case, the transition specification is overridden and transition is set at the laminar separation point. For all cases, turbulent separation occurred on the lower surface which is physically unrealistic and is due to the assignment of the transition point too far forward on the lower surface. To show this, four runs were made for the same Mach number, angle of attack, reference Reynolds number and transition point location (10% chord) on the upper surface. Calculations were run with transition locations on the lower surface of 20, 40, 60, and 80% chord. Results are shown in Table 2. It is seen that all four cases end up with transition on the upper surface set at 8.2% chord (laminar boundary layer separation) induced by the large suction peak in the pressure distribution. The turbulent boundary layer on the upper surface remains attached. The solution on the bottom surface separates at 88.2% when the transition point is set at 20% chord. For transition point at 40% the flow remains fully attached. In the remaining two cases of assigned transition at 60 and 80% chord, the transition occurs naturally at 47.8% chord due to laminar boundary layer separation resulting in identical solutions with no turbulent separation.

From the above discussion, it is clear that the solutions can be sensitive to the transition point location, particularly when the transition point on the lower surface is set far forward. For a typical transonic wing geometry, the transition point on the upper surface should be set just down stream of the suction peak. For the lower surface, if the computation is made

for wind tunnel data comparisons, the separation point should be set at the location where the boundary layer is tripped, otherwise, the transition location should be set at far enough downstream of the leading edge to insure natural transition.

5.2.2 Reynolds Number Dependence of Viscous Wing Solution

Computations were made to study the Reynolds number dependence of the theoretical solutions. The computations are for the wing A at $M_\infty = 0.82$ and $\alpha = 1.5°$. Reference Reynolds numbers for the seven cases were, 5M (5 million), 8M, 10M, 12M, 14M, and 16M, respectively. The runs above Re = 10M required smaller integration steps in the boundary layer solution in order to avoid unrealistic results associated with the momentum thickness becoming negative. The results for the lift variation with Reynolds number are shown in Fig. 29. There is a strong Reynolds number effect for $Re < 8 \times 10^6$. The lift levels off quite rapidly beyond 10M indicating that the results of free flight chord Reynolds number in the 100M - 200M range can be extrapolated from the present results. The inviscid, large Reynolds number limit for the lift coefficient in this case is $C_L = .637$ as determined from an inviscid calcualtion. These results show that very large Reynolds numbers are required to approach the inviscid limit and that viscous effects will be very important even at flight Reynolds numbers.

5.2.3 Solution for Pressure & Section Lift Distributions & Comparison with Experiment

In this section, we compare solutions for the pressure distribution, lift, and drag with experimental data for Lockheed Wings A and B. The pressure distributions given here are the composite pressure as given by Eq (4.3.8) and (4.3.9). The freestream Mach number, M_∞, and chord Reynolds numbers were matched with those of Lockheed test cases. The boundary layers were tripped at 5% chord from the leading edge. Since the effective angles of attack of the wind tunnel test are subjected to major uncertainties due to wall interference, we carried the computations out at an angle of attack chosen to closely match experimental values of total lift.

For the Wing A run, the free stream Mach number M_∞ was .82, the angle of attack α was set to 2°, the reference Reynolds number Re_{ref} was six million and a grid of 160 x 16 x 32 was used. In addition to a 5% chord tripped boundary layer run, a natural transition run was made for comparison.

Furthermore, an inviscid run was also made for the same M_∞ and α. Nothing special was required to achieve a converged solution. The maximum inviscid residual was down to less than 10^{-5} after about 10 cycles of boundary layer computations or ninety inviscid fine grid sweeps. At this point the inviscid pressure was accurate to within 10^{-4} and CPU time was about three minutes on a Cray-1S computer. Of this about 2 minutes of CPU time was for the computation of the inviscid solution. The convergence history of the total number of supersonic points and the wing root section circulation are shown in Fig. 30. The position of the floating wake was the last quantity to converge. Figure 31 shows the convergence history of the last point of the wake at the wing root section as a function of boundary layer iteration. The converged wake at this section is shown in Fig. 32.

The results show that for the natural transition case, the transition occurred at 8.1% chord on top of the wing and 50% chord on the bottom surface. The results for the forces are shown in Table 3. It is seen that the wing lift coefficients, C_L, and drag coefficients, C_D, for the two transition calculations are relatively close to each other. The two transition calculations gave different boundary layer solutions and hence different friction drags. This will be discussed in the next section. The C_L for the viscous solution (tripped boundary layer) was .536 as compared with the inviscid value of .749. The experimental value of C_L was .53 at a nominal angle of attack of 2.9° (compared to the $\alpha = 2°$ used in the comutation).

Results for section pressure distributions (for the tripped boundary layer case) are shown in Fig. 33a - 33e for η = .15, .30, .50, .70, and .95, respectively, where η is the sectional distance from the wing root normalized with the half span. Shown also are the inviscid pressure distributions at the same free stream Mach number (M_∞ = .82) and angle of attack ($\alpha = 2°$) as well as the experimental results. It is seen that the viscous effect at this Reynolds number (6M) is quite strong. Shock location is shifted upstream and shock strength becomes much weaker resulting in a much lower lift. The viscous effect on the bottom wing surface is relatively small. The reasons for the poor agreement of the pressure distribution with the data on the lower surface near the trailing edge are not understood at this time. The comparisons for span load distributions for the same case are shown in Fig. 34. We note again the vast differences between the viscous and inviscid

solution for the section lift distribution. The isobar plots for the converged viscous solution are shown in Fig. 35. Pressure distributions on the wing and wake for the top and the bottom surfaces are displayed. Because of the viscous effects, the shock patterns differ greatly from those in the inviscid solution. The lambda type shock pattern is clearly exhibited. The bottom surface shows relatively smooth flow patterns with no shock waves. The pattern is "2-D" like on the lower surface except near the wing tip region.

For the Wing B runs, the free stream Mach number was $M_\infty = .9$, the Reynolds number Re_{ref} was 10 million and the boundary layers were tripped at 5% chord to match the experimental values. The computation grid was (128 x 16 x 32). Two angles of attack $\alpha = 3°$ and $\alpha = 3.5°$ were run in order to compare with the nominal experimental value of $\alpha = 3.9°$. The results for section lift distributions at $\eta = .2, .4, .6, .8,$ and .95 and wing loadings are shown in Table 4. Because of higher Reynolds number, it is seen that the lift results for the viscous flow calculation differ by only about 10% from the inviscid values. The experimental value of C_L was .49 at a nominal angle of attack of $\alpha = 3.9°$. Sectional pressure distributions for both the viscous and inviscid calculations at $\alpha = 3.5°$ are shown in Fig. 36a - 36e for $\eta = .2, .4, .6, .8,$ and .95, respectively. The span load distribution for the same case is shown in Fig. 37. The overall viscous effects are small as compared to the Wing A computations which is consistent with the difference in Reynolds numbers in these two cases.

5.2.4 Boundary Layer & Wake Solutions

In this section, we present solutions for some of the boundary layer quantities from the results of the converged viscid-inviscid interaction solution. For Wing A calculations at $M_\infty = .92$, $\alpha = 2°$ and $Re_{ref} = 6 \times 10^6$, two solutions are presented, one for tripped transition (5% chord) and one for natural transition. The results for the displacement thickness δ^*, the momentum thickness θ_{11}, the skin friction C_f and the shape factor H at the mid span station are given in Fig. 38 - 41, respectively. In the natural transition case, the transition point on the upper surface occurred at 8.1% chord. The two solutions on the upper surface are virtually identical. On the bottom surface, natural transition occurred at 50% chord compared to the 5% location of the fixed transition case. The solutions on the lower surfaces differ significantly. The displacement and momentum thicknesses are much

smaller in the natural transition runs as shown in Fig. 39. The comparison of the skin friction results shown in Fig. 40, indicates that natural transition will result in a smaller friction drag due to a larger area of the wing surface covered by laminar flow.

The isocline results for the tripped transition run are shown in Fig. 42a - 42f. Both the top and the bottom wing and wake surface plots are shown. The isoclines for the surface velocity are shown in Fig. 42a. This velocity is the converged interaction "inviscid solution" with trailing edge strong interaction corrections. It is seen that the contours are quite similar to those of the isobar results shown in Fig. 35. On the top wing surface, the lambda shock structure is restricted to about 40% of the half span region from the wing root. In this region, the boundary layer exhibits more 3-D effects. On the bottom wing surface, the spanwise variations of the solution is relatively small. The wing tip effects are apparent as shown in the results of surface velocity angle $\tilde{\alpha}$ in Fig. 42b. Relatively large gradients are seen near the tip and towards the trailing edge and into the wake. It is also seen that the contours of the surface velocity angle in the wake for the top and the bottom surfaces are quite similar indicating that the viscous wake in this case does not have a very complicated 3-D structure. The boundary layer solutions for the displacement thickness δ^*, the momentum thickness θ_{11}, the shape factor H and the limiting wall streamline angle β are shown in Fig. 42c - 42f, respectively. The displacement thickness δ^* has a rather curious wake distribution on the top surface where a moderate gradi-ent in the spanwise direction is shown near the wing root region. This reflects the fact that more realistic wing root boundary conditions are probably required. This aspect is beyond the scope of the present study. From our experience, the shape factor H is the most sensitive part of the boundary layer calculation. At early stages of the interation, there is relatively large spanwise gradient for H near the intersection of the two shocks. Boundary layer computations can break down if the shocks are too strong. At a later stage, the spanwise gradient gradually decreases as the viscous effect sets in and shocks become weaker. The converged results for H is shown in Fig. 42e. The distribution of the limiting wall streamline deviation angle β from the external inviscid streamline is shown in Fig. 42f.
The variation of β is relatively mild except near the outboard and trailing edge region on the bottom surface, where most of the spanwise flow occurs.

6. CONCLUSIONS

The principle conclusions of this report are:

- The approximate factorization scheme (AFZ) used in the inviscid calculation presented in this report is as efficient as any state-of-the-art scheme available today. Inclusion of the Prandtl-Glauert far field boundary condition made the scheme faster and more reliable. Extending the method to second-order accuracy in the supersonic zone affected the solution significantly in critical areas (i.e., leading edge and wing tip). The assumption of irrotational flow does introduce some inaccuracies, particularly for strong shocks. The use of the Euler equations may be an alternative but their solution would require more computing time and memory. In addition, the Euler equations may introduce additional computational difficulties.

- The 3-D boundary layer equations resulting from the integral method formulation are very complex. There is room for improvement in the solution method of these equations. The lack of a complete set of physical boundary conditions at the tip and root sections forces us to use arbitrary zero gradient conditions at these stations and this introduces errors on the wing in the region of influence of these points. For high aspect transport wings, errors introduced in these regions are small and the consequences are not too important for engineering purposes. However, this will not be the case for highly swept, low aspect ratio fighter type wings.

- The results indicate that the wing loadings are strongly controlled by the inviscid solutions which are affected by the grid resolution and distribution.

- The "direct mode" boundary layer analysis as employed in the present study has a suprisingly large region of validity. While the "inverse mode" boundary layer analysis has proved very successful in 2-D studies with small separated region, the method has yet to be explored in 3-D boundary layers. Three-dimensional boundary layer separation is inherently more complex and very likely cannot be adequately treated by extension of the 2-D inverse methods.

- The present investigation has demonstrated that the "zonal" approach is a practical procedure for computing viscous flows over realistic wings at transonic speeds. Results are qualitatively good in many cases although many areas of improvement are required to achieve accuracies comparable to our 2-D viscous airfoil codes, GRUMFOIL.

7. REFERENCES

1. Caughey, D.A., "The Computation of Transonic Potential Flows," Annual Review of Fluid Mechanics, Vol 14, pp 261-283, 1982.

2. Hall, M.G., "Advances and Shortcomings in the Calculation of Inviscid Flows with Shock Waves," Numerical Methods in Aeronautical Fluid Dynamics, Roe, P.L., editor, Academic Press, pp 31-60, 1982.

3. Jameson, A., "The Evolution of Computational Methods in Aerodynamics," Princeton University Report MAE No. 1608, May 1983; also published in ASME Journal of Applied Mechanics, Vol 50, Dec 1983, pp 1052-1070.

4. Nixon, D., Editor, "Transonic Aerodynamics,"Progress in Astronautics and Aeronautics, Vol 81, published by the American Institute of Aeronautics and Astronautics, Inc, 1982.

5. Kline, S.J., "Closure on Universal or Zonal Modeling - The Road Ahead," The 1980-91 AFOSR-HTTM-Stanford Conference on Complex Turbulent Flows: Comparison of Computation and Experiment, Vol. II - Taxonomies, Reporter's Summaries, Evaluation and Conclusions, Kline, S.J., Cantwell, B.J. and Lilly, G.M., editors, Stanford University, Stanford, CA, 14-18 Sept 1981.

6. Melnik, R.E., Chow, R.R., Mead, H.R., and Jameson, A., "An Improved Viscid/Inviscid Interaction Procedure for Transonic Flow Over Airfoils," NASA CR-3805, 1985.

7. Melnik, R.E., Mead, H.R., and Jameson, A., "A Multi-Grid Method for the Computation of Viscid/Inviscid Interaction on Airfoils," AIAA Paper No. 83-0234, presented at AIAA 21st Aerospace Sciences Meeting, Reno, NV, Jan 1983.

8. Melnik, R.E., "Turbulent Interactions on Airfoils at Transonic Speeds - Recent Developments," AGARD Conference on Computation of Viscous-Inviscid Interactions, AGARD-CP-291, 29 Sept - 1 Oct 1980.

9. Collyer, M.R. and Lock, R.C., "Prediction of Viscous Effects in Steady Transonic Flow Past an Airfoil," Aeronautical Quarterly, Vol XXX, pp 485-505, Aug 1979.

10. LeBalleur, J.C., "Strong Matching Methods for Computing Transonic Viscous Flow Including Wakes and Separations - Lifting Airfoils," La Recherche Aerospatiale, English edition, No. 1981-3, pp 21-45, 1981.

11. Whitfield, D.L., Thomas, J.L., Jameson, A. and Schmidt, W., "Computation of Transonic Viscous-Inviscid Interacting Flow," Second Symposium on Numerical and Physical Aspects of Aerodynamic Flows, Cebeci, T., editor, California State University, Long Beach, CA, Jan 1983.

12. Whitfield, D.L. and Thomas, J.L., "Transonic Viscous-Inviscid Interaction Using Euler and Inverse Boundary-Layer Equations," Viscous Flow computational Methods, third Volume in the series on recent advances in numerical methods in fluids, Habashi, W.G., editor, Pineridge Press Ltd, 1983.

13. Lock, R.C. and Firmin, M.C.P., "Survey of Techniques for Estimating Viscous Effects,"Numerical Methods in Aeronautical Fluid Dynamics, Roe, P.L., editor, Academic Press, pp 337-430, 1982.

14. LeBalleur, J.C., "Calcul des Ecoulements a Forte Interaction Visqueuse au Moyen de Methodes de Couplage," AGARD Conference on Computation of Viscous-Inviscid Interactions, AGARD-CP-291, 29 Sept - 1 Oct 1980.

15. Lock, R.C., "A Review of Methods for Predicting Viscous Effects on Airfoils and Wings at Transonic Speeds," AGARD Conference on Computation of Viscous-Inviscid Interactions, AGARD-CP-291, 29 Sept - 1 Oct 1980.

16. Stock, H.W., "Integral Method for the Calculation of Three-Dimensional, Laminar and Turbulent Boundary Layers," NASA Technical Memorandum NASATM75320, July 1978. (Translation of "Integralverfahren Zur Berechnung Drieidimensionaler, Laminarer Und Turbulenter Grenzschicten," Cimier GMBH, Friedrickshafer, West Germany, Report 77/51B, Oct 1977).

17. Green, J.E., Weeks, D.J. and Bromen, J.W.F., "Prediction of Turbulent Boundary Layers and Wakes in Compressible Flows by a Lag Entrainment Method", RAE Technical Report 72231, Dec 1972.

18. Firmin, M.C.P., "Calculation of Transonic Flow Over Wing/Body Combinations with An Allowance for Viscous Effects," AGARD Conference on Computation of Viscous-Inviscid Interactions, AGARD-CP-291, 29 Sept - 1 Oct 1980.

19. Waggoner, E.G., "Transonic Three-Dimensional Viscous-Inviscid Interaction for Wing Body Configuration Analysis," AIAA Paper preprint AIAA-82-0163, 20th Aerospace Sciences Meeting, Orlando, FL, 11-14 Jan 1982.

20. Streett, C.L., "Viscous-Inviscid Interaction for Transonic Wing-Body Configurations Including Wake Effects," AIAA Journal, Vol 20, No. 7, pp 915-923, July 1982.

21. Wigton, L.B., and Yoshihara, H., "Viscous-Inviscid Interactions With a Three-Dimensional Inverse Boundary Layer Code," Second Symposium on Numerical and Physical Aspects of Aerodynamic Flows, California State University, Long Beach, CA, 17-20 January 1983.

22. Samant, S.S. and Wigton, L.B., "Coupled Euler/Integral Boundary Layer Analysis in Transonic Flow," AIAA Paper No. 83-1806, presented at AIAA Applied Aerodynamics Conference, Danvers, MA, July 1983.

23. Jameson, A. and Baker, T.J., "Solution of the Euler Equations for Complex Configurations," AIAA Paper No. 83-1929, presented at AIAA Computational Fluid Dynamics Conference, Danvers, MA, July 1983.

24. Jameson, A. and Caughey, D.A., "A Finite-Volume Method for Transonic Potential Flow Calculations," Proceedings AIAA 3rd Computational Fluid Dynamics Conference, Alburquerque, NM, pp 35-54, June 1977.

25. Holst, T., "An Implicit Algorithm for the Conservative Transonic Full-Potential Equation Using an Arbitrary Mesh," AIAA Journal, Vol 17, No. 10, pp 1038-1045, Oct 1979.

26. Sankar, N.L., Malone, J. and Tassa, Y., "A Strongly Implicit Procedure for Steady Three-Dimensional Transonic Potential Flows," Proceedings, AIAA Journal, Vol 20, No. 5, pp 598-605, May 1982.

27. Baker, T.J. and Forsey, C.R., "A Fast Algorithm for the Calculation of Transonic flow Over Wing/Body Combinations," AIAA 5th Computational Fluid Dynamics Conference, Palo Alto, CA, pp 189-198, June 1981.

28. Caughey, D.A., "Multi-grid Calculations of Three-Dimensional Transonic Potential Flows," AIAA paper 83-0374, presented at AIAA 21st Aerospace Sciences Meeting, Reno, NV, Jan 1983.

29. Shmilovich, A., and Caughey, D.A., "Application of the Multi-Grid Method to Calculations of Transonic Potential Flow About Wing-Fuselage Combinations," NASA Conference Publication 2202, Oct 1981.

30. Jameson, A., Schmidt, W., and Turkel, E., "Numerical Solutions of the Euler Equations by Finite Volume Methods Using Runge-Kutta Time-Stepping Schemes," AIAA Paper 81-1259, AIAA 14th Fluid and Plasma Dynamics Conference, Palo Alto, CA, June 1981, AIAA Paper 81-1259.

31. Benek, J., Steinhoff, J., and Jameson, A., "Application of Approximate Factorization to Three-Dimensional Transonic Flow Calculations," AIAA Paper 81-1026-CP, Palo Alto, CA, June 1981.

32. Klunker, E.B., "Contribution to Methods for Calculating the Flow About Lifting Wings at Transonic Speeds - Analytic Expressions for the Far Field," NASA TDN-6530, 1971.

33. Caughey, D.A. and Jameson, A., "Basic Advances in the Finite-Volume Method for Transonic Potential Flow Calculations," Symposium on Numerical and Physical Aspects of Aerodynamic Flows, Cebeci, T., editor, published by Springer-Verlag, 1982.

34. Ballhaus, W.F., Jameson, A. and Albert, J., "Implicit Approximate-Factorization Schemes for the Efficient Solution of Steady Transonic Flow Problems," AIAA Journal, Vol. 16, No. 6, pp 573-579, June 1978.

35. Fernholz, H.H. and Krause, E., editors "Three-Dimenisonal Turbulent Boundary Layers,"International Union of Theoretical and Applied Mechanics Symposium Proceedings, Berlin, Germany, 29 March - 1 April, 1982.

36. Cousteix, J. and Houdeville, R., "Singularities in Three-Dimensional Turbulent Boundary-Layer Calculations and Separation Phenomena," AIAA Journal, Vol 19, No. 8, Aug 1981.

37. Formery, M. and Delery, J., "Finite Difference Method for Inverse Mode Computation of a Three-Dimensional Turbulent Boundary Layer," La Recherche Aerospatiale, No. 1981-5, English edition, pp 11-21, 1981.

38. Cebeci, T., Kamps, K. and Ramsey, J.A., "A General Method for Calculating Three-Dimensional Compressible Laminar and Turbulent Boundary Layers on Arbitrary Wings," NASA CR-2777, Jan 1977.

39. McLean, J.D. and Randall, J.L., "Computer Program to Calculate Three-Dimensional Boundary Layer Flows Over Wings with Wall Mass Transfer," NASA CR-3123, May 1979.

40. Myring, D.F., "An Integral Prediction Method for Three-Dimensional Turbulent Boundary Layers in Incompressible Flow," RAE Technical Report 70147, Aug 1970.

41. Smith, P.D., "An Integral Prediction Method for Three-Dimensional Compressible Turbulent Boundary Layers," ARE Technical Report 72228, Dec 1972.

42. Stock, H.W. and Horton, H.P., "Ein Integralverfohren Zur Berechnung Dreidinensionaler, Laminarer Kompressibler, Adiabater Grenzschicten," Doiner Wehrtechnische Forshung, Rufo 4, July 1979.

43. Mager, A., "Generalization of Boundary Layer Momentum Integral Equations to Three-Dimensional Flows, Including Those of Rotating Systems," NACA Report No. 1067, 1952.

44. Johnston, J.P., "Three-Dimensional Turbulent Boundary-Layers," MIT Gas Turbine Lab Report No. 39, 1957.

45. Moretti, G., "The λ-Scheme," Computers and Fluids, Vol 7, pp 191-205, 1979.

46. Kreiss, H-O., "Initial Boundary Value Problems for Hyperbolic Equations," Communications of Pure and Applied Mathematics, Vol 23, pp 277-298, 1970.

47. Schlichting, H., Boundary Layer Theory, English Translation by Kestin, J., 4th Edition, p 580, 1960.

48. Hinson, B.L. and Burdges,K.P., "Acquisition and Application of Transonic Wing and Far-Field Test Data for Three-Dimensional Computational Method Evaluation," AFOSR TR-80-0421, 0422, March 1980.

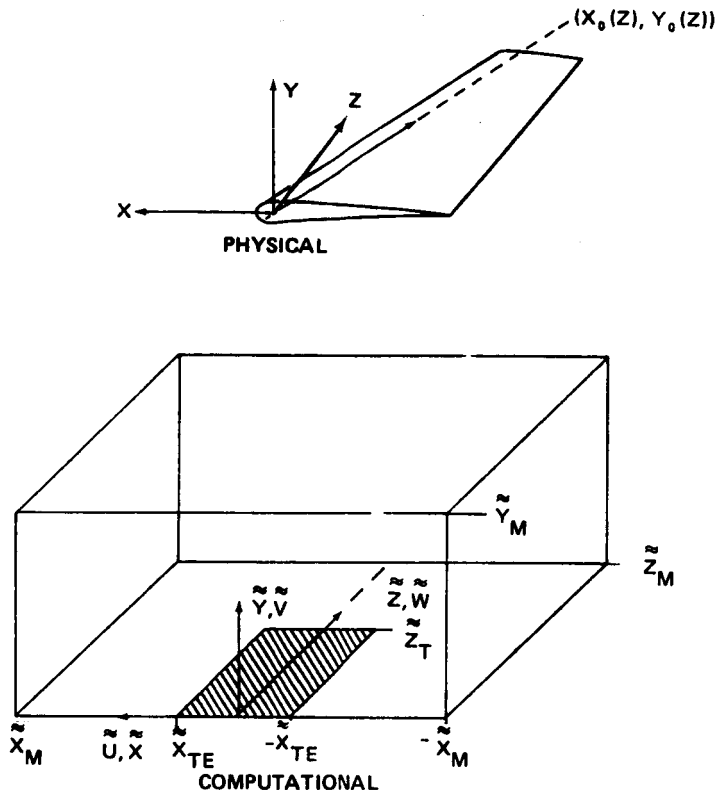

Fig. 1 Coordinate Systems

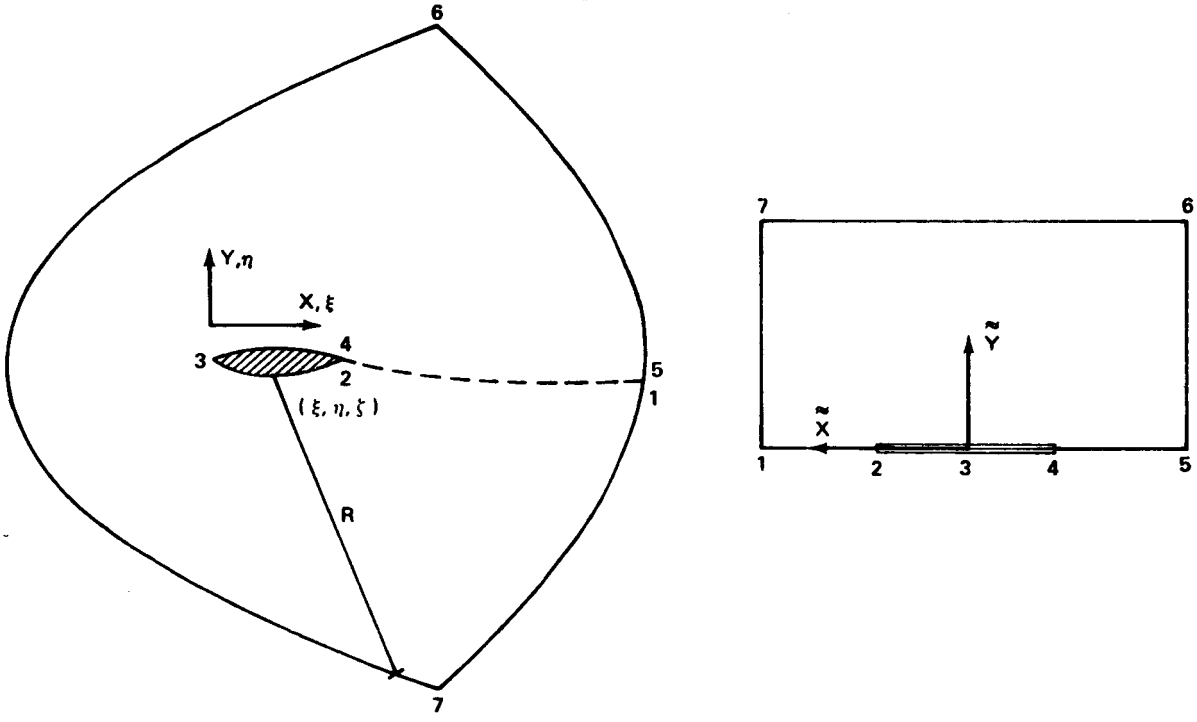

Fig. 2 Boundary of C-Mesh in Z = Constant Plane

$$L(\phi) = 0$$

$$L(\phi) = \frac{\partial}{\partial X}(\rho hU + P) + \frac{\partial}{\partial Y}(\rho hV + Q) + \frac{\partial}{\partial Z}(\rho hW + R)$$

$$h = \det(H)$$

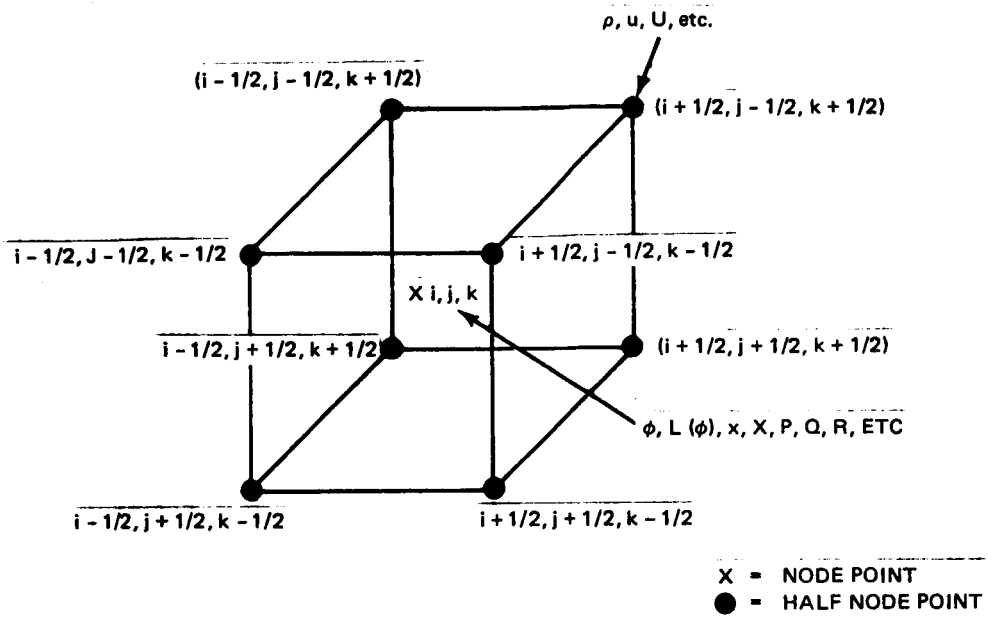

a) 3-D Computational Cell

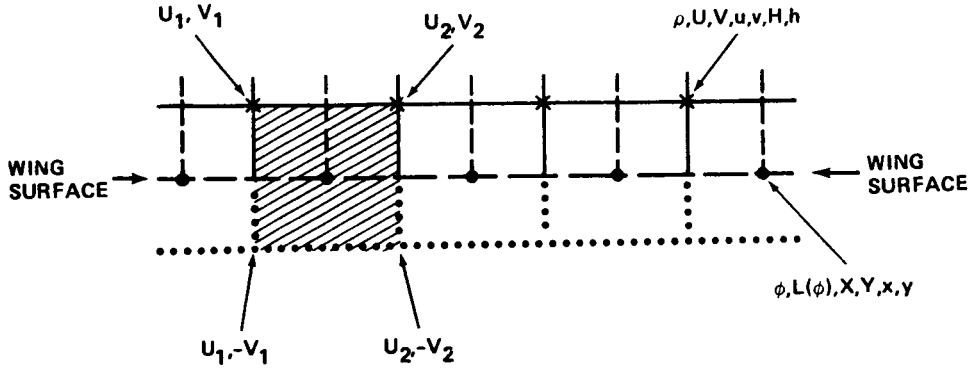

b) 2-D Boundary Conditions

Fig. 3 Finite Volume Formulation

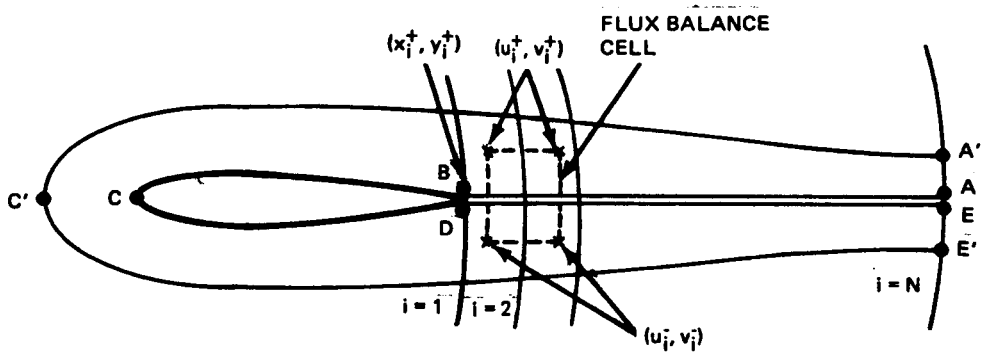

Fig. 4 Fitted Wake Coordinates - Physical Plane

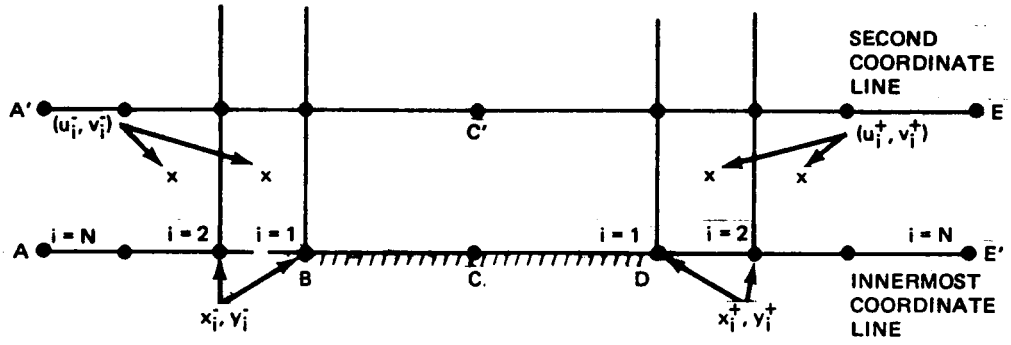

Fig. 5 Fitted Wake Coordinates - Computational Plane

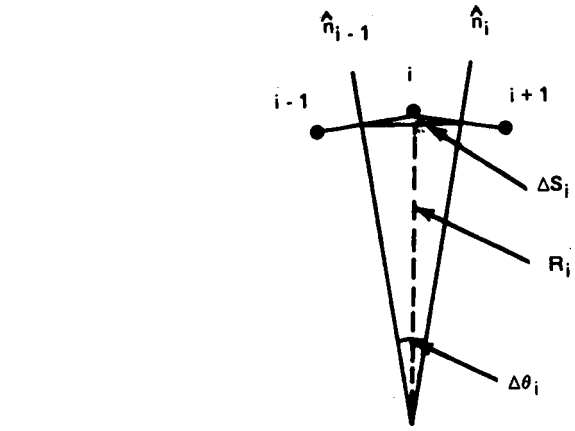

a) Flow in x-y Plane

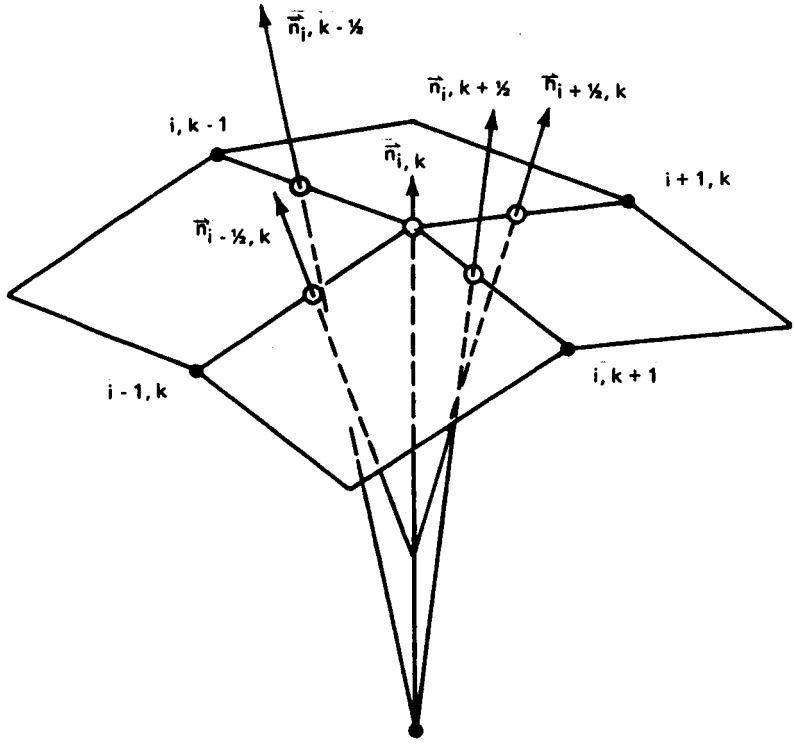

b) General Flow

Fig. 6 Wake Curvature Calculation

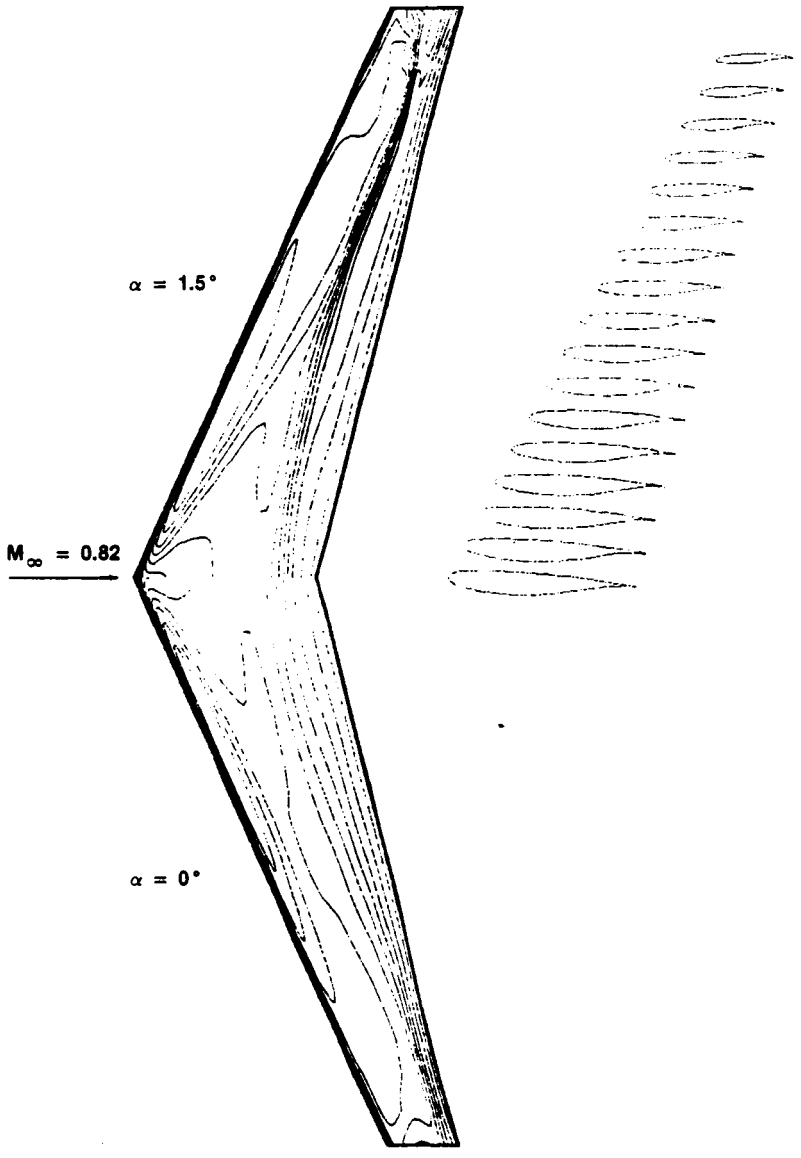

a) Surface Isobars

Fig. 7 Study of Lockheed Wing A Results, M_∞ = .82 (Sheet 1 of 2)

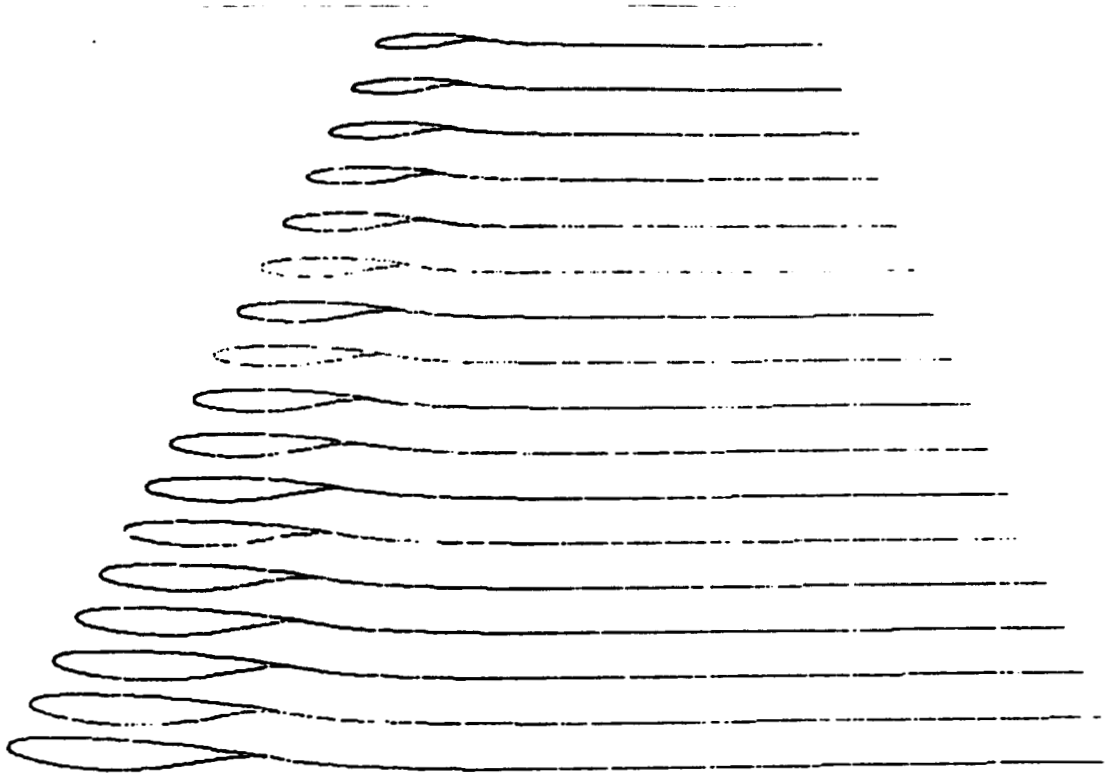

b) Fit Trailing Wake α = 1.5

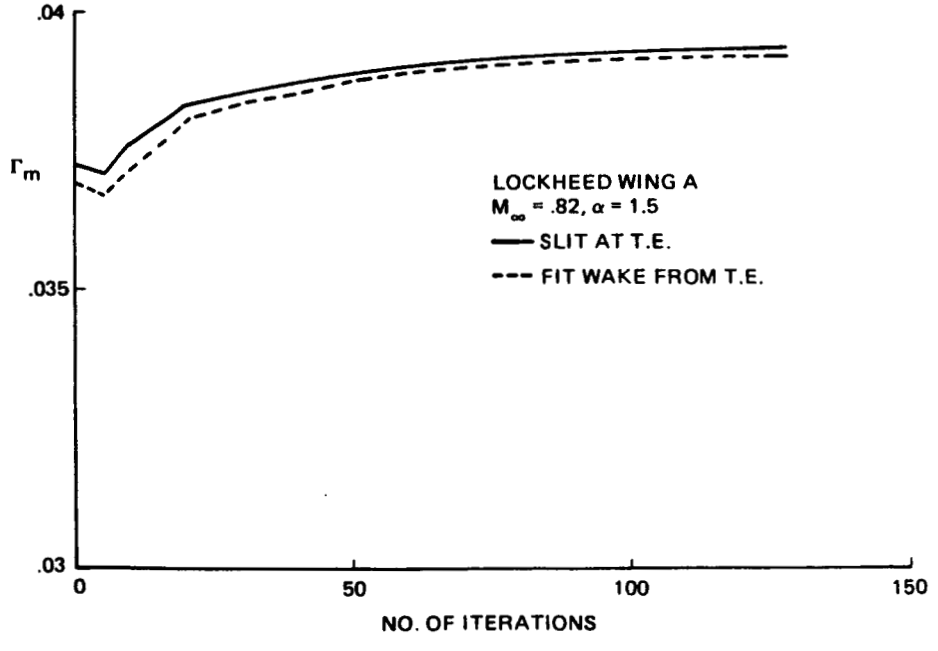

c) Comparison of Lift Convergence (Γ = Circulation at Mid-Span Sections)

Fig. 7 Study of Lockheed Wing A Results, M_∞ = .82 (Sheet 2 of 2)

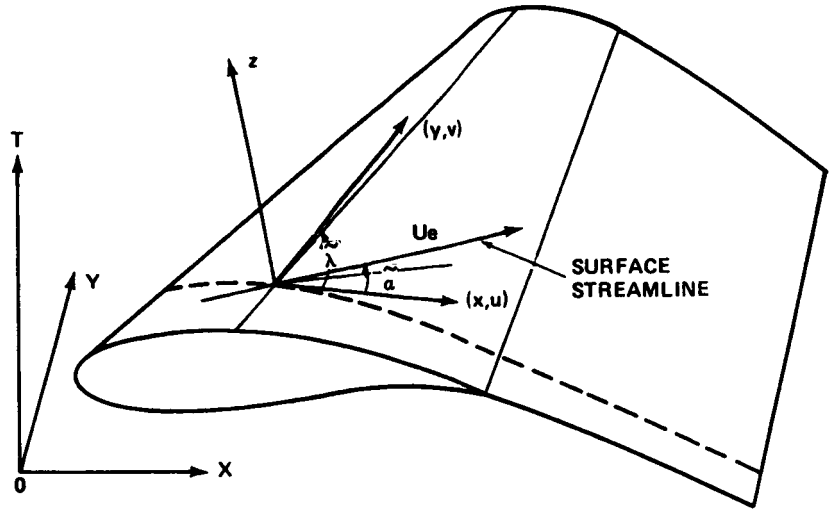

Fig. 8 Coordinate System for 3-D Boundary Layers

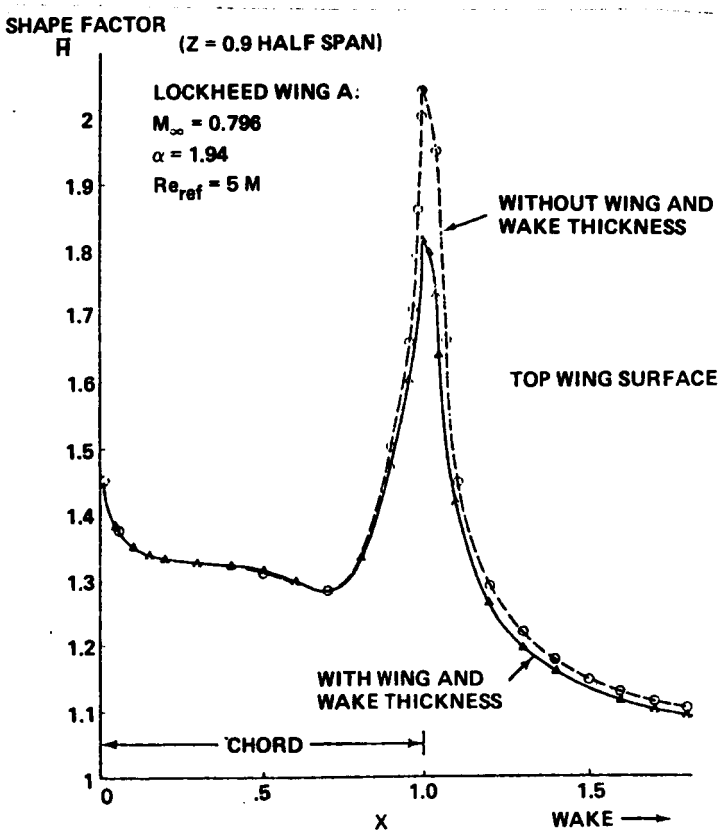

Fig. 9 Effect of Metric Coefficients on 3-D Boundary Layer and Wake Solution

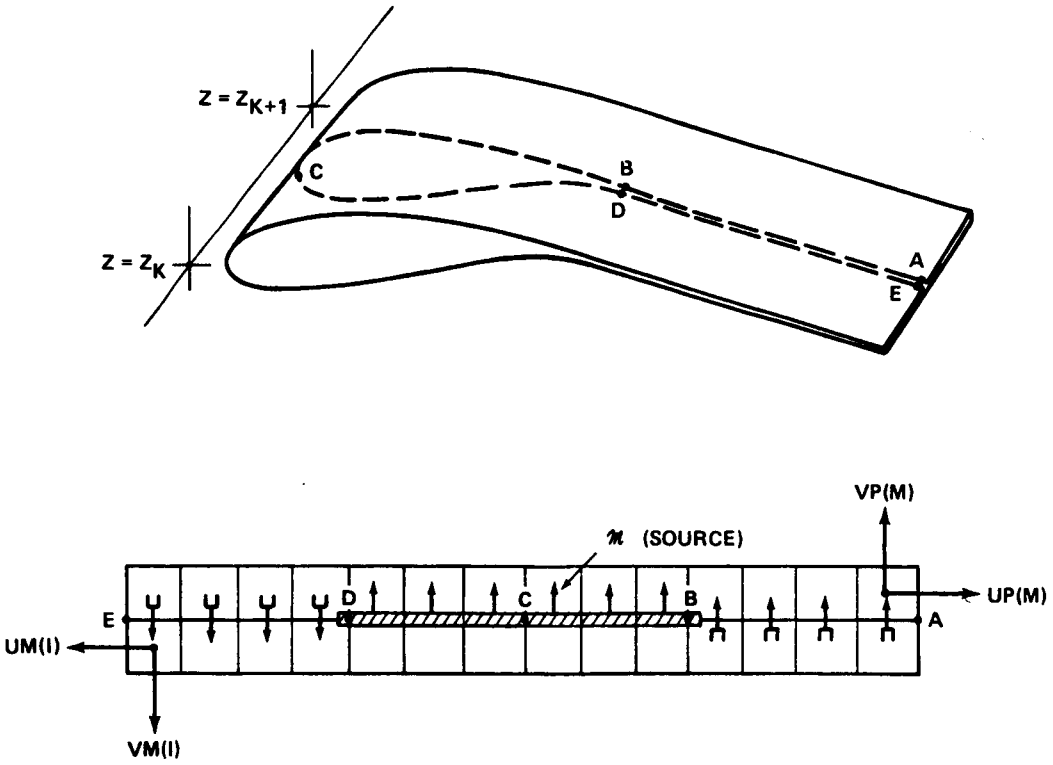

Fig. 10 Transpiration Boundary Conditions for Finite Volume Interaction Scheme

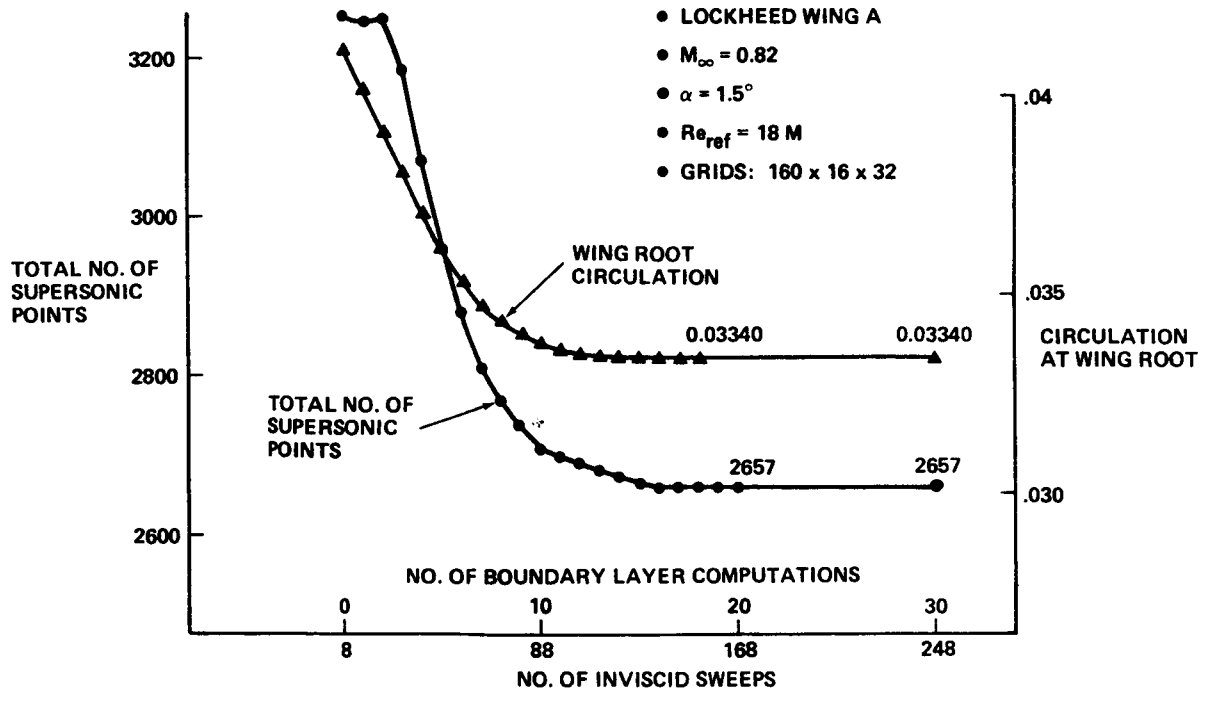

Fig. 11 Convergence History of No. of Supersonic Points & Wing Root Circulation

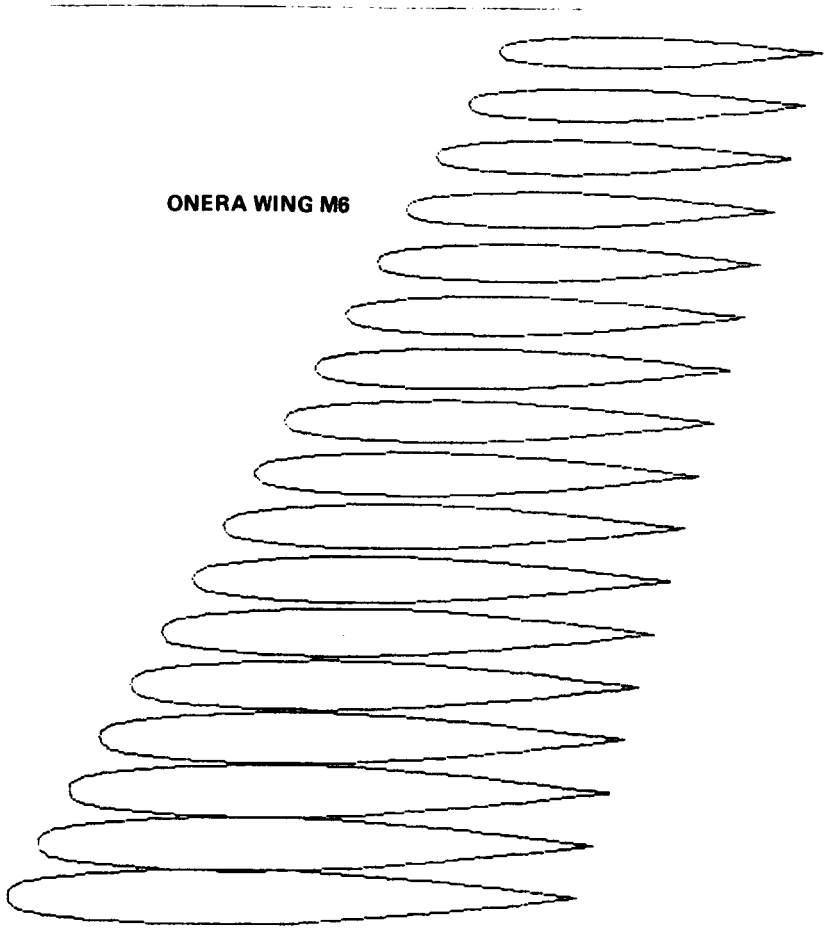

Fig. 12 View of Wing

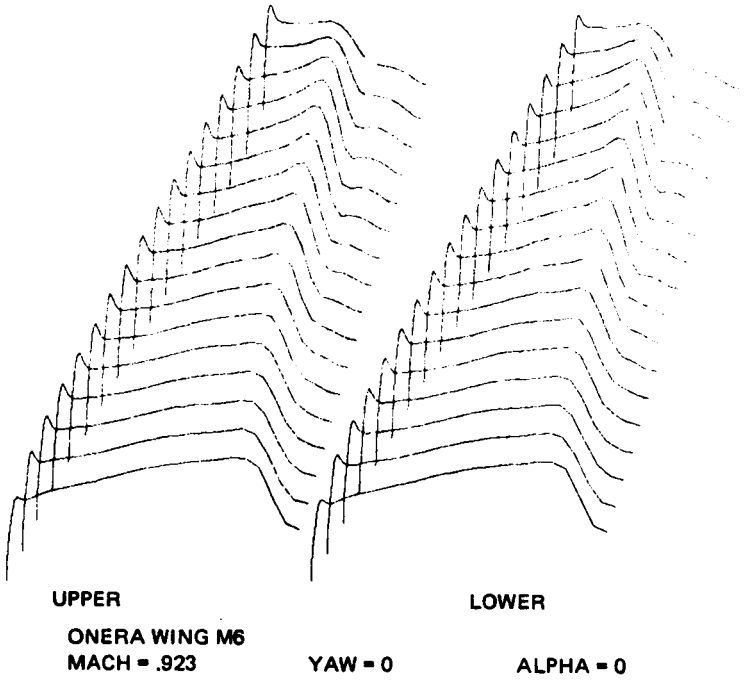

Fig. 13 Surface Pressures, Nonlifting Case

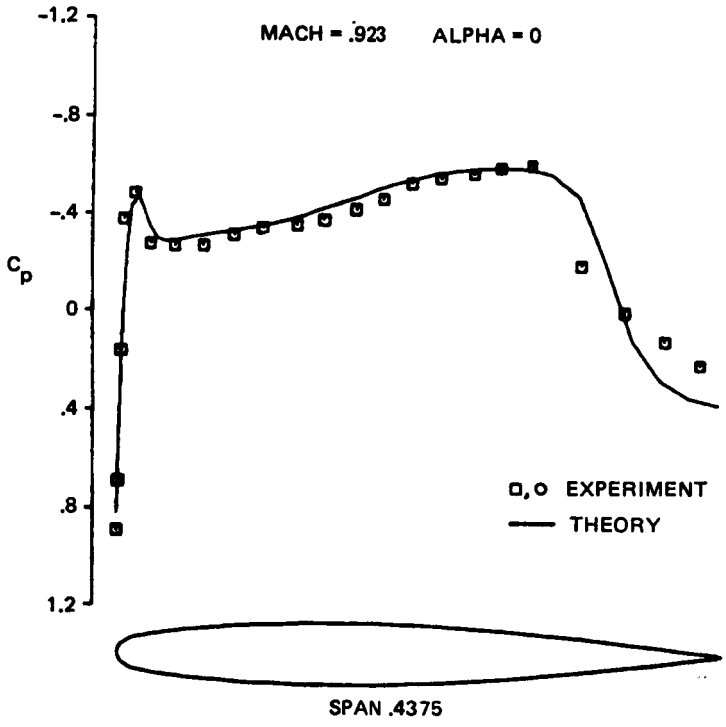

Fig. 14 Comparison with Experiment, Nonlifting Case

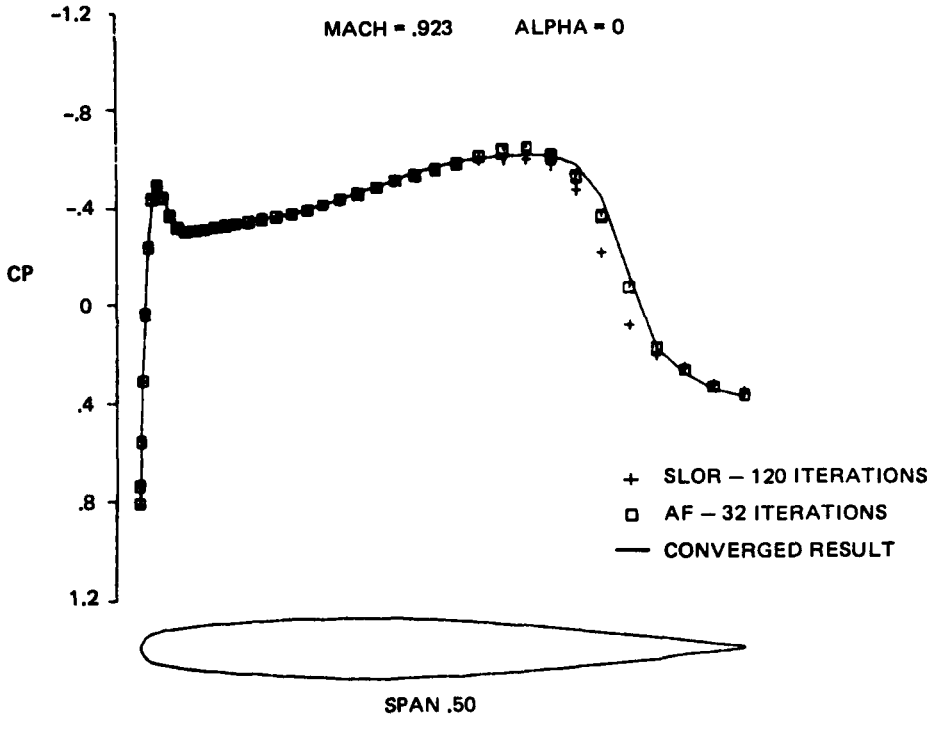

Fig. 15 Convergence Comparison: Surface Pressure, Nonlifting Case

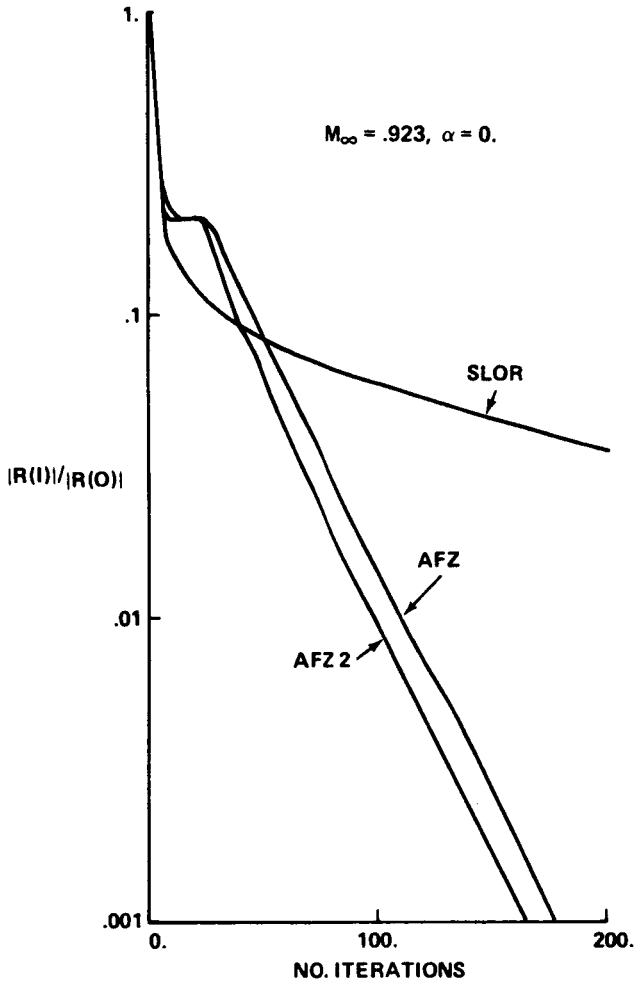

Fig. 16 Convergence Comparison: Average Residual, Nonlifting Case

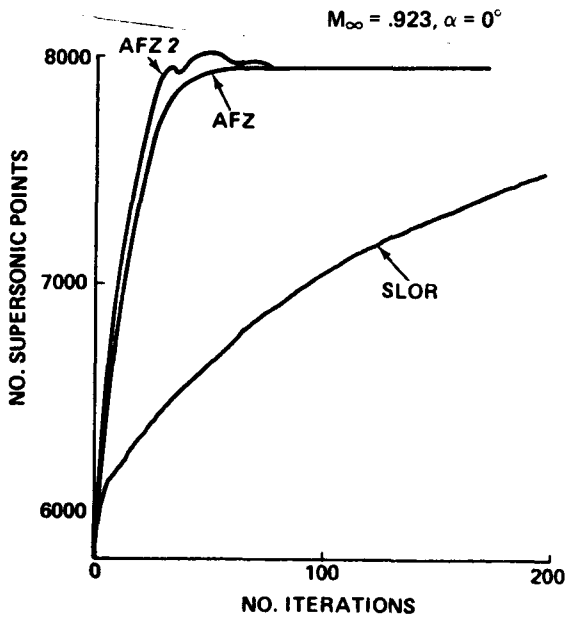

Fig. 17 Development of Supersonic Zone, Nonlifting Case

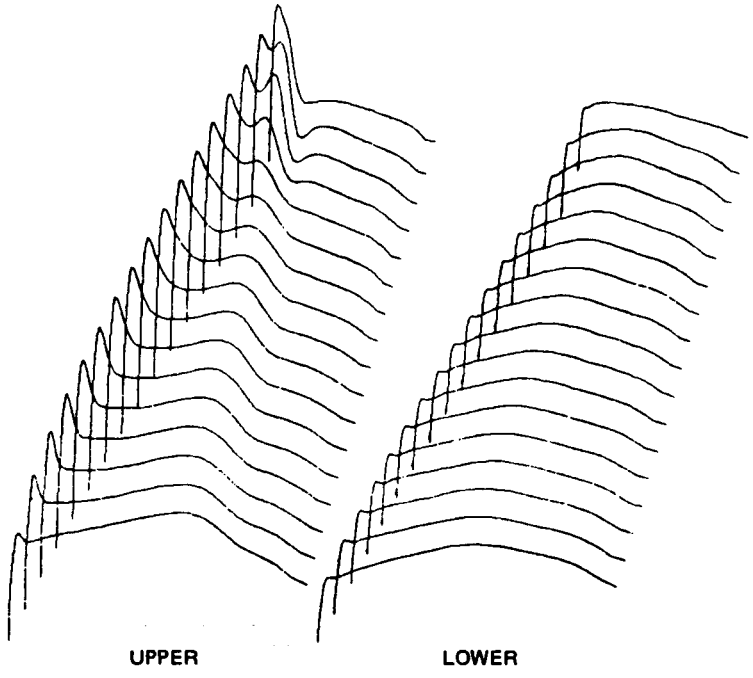

Fig. 18 Surface Pressures, Lifting Case

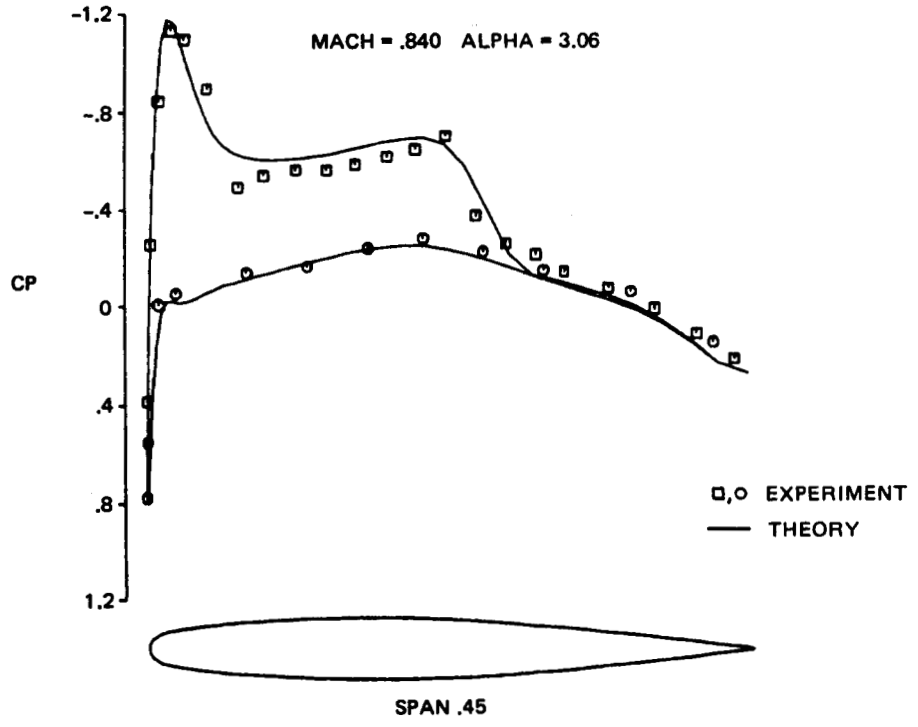

Fig. 19 Comparison with Experiment, Lifting Case

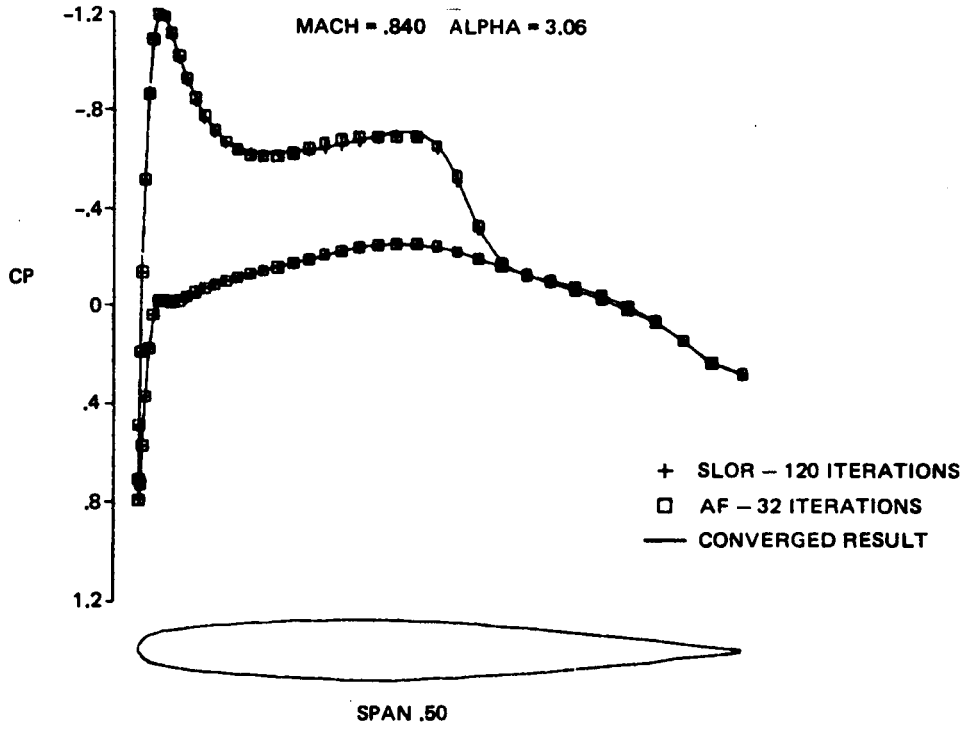

Fig. 20 Convergence Comparison: Surface Pressure, Lifting Case

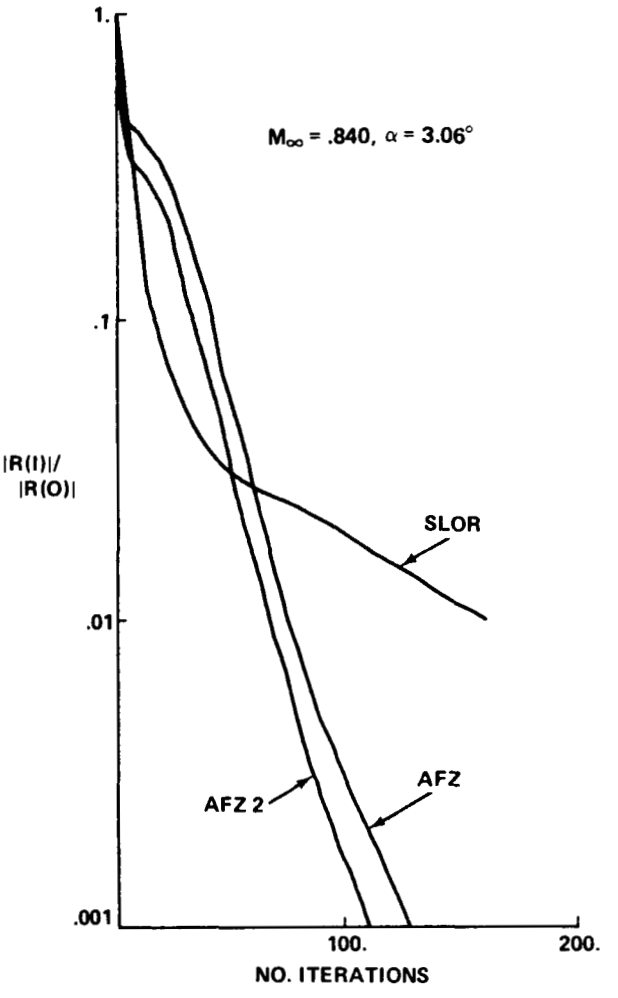

Fig. 21 Convergence Comparison: Average Residual, Lifting Case

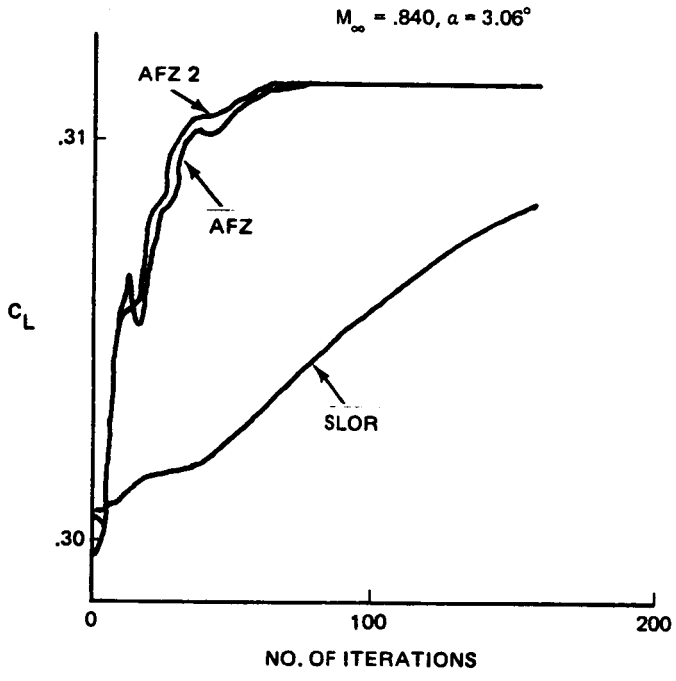

Fig. 22 Development of Lift Mid-span, Lifting Case

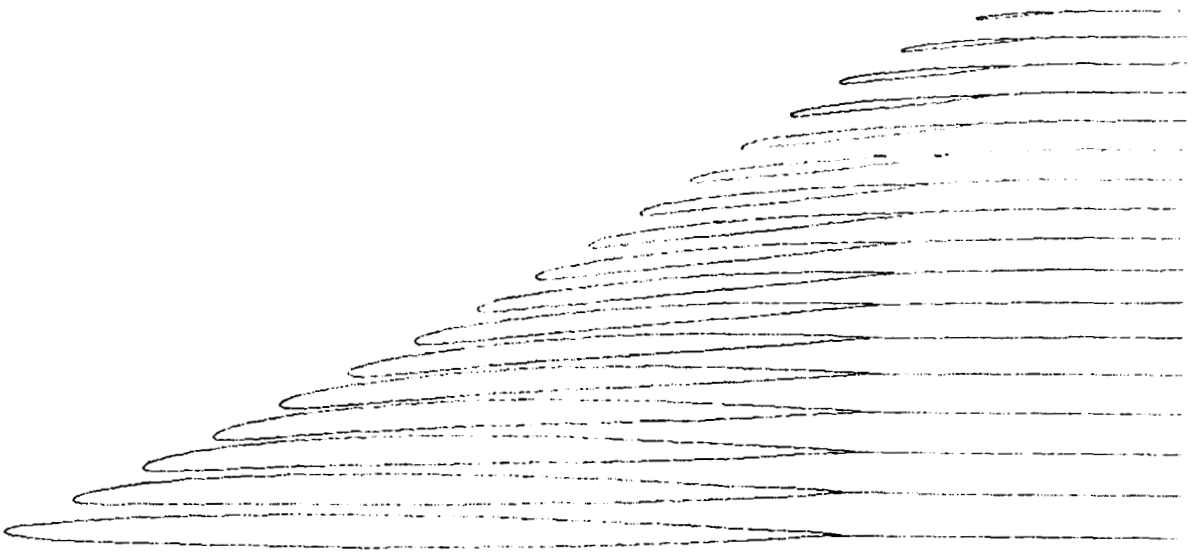

a) 3-D View of Wing

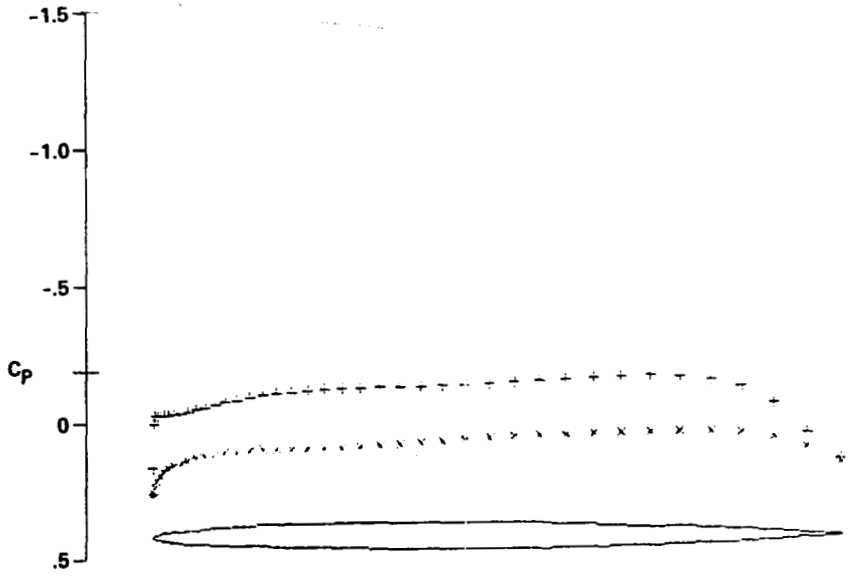

b) Root Section

Fig. 23 Sample Wing, $M_\infty = 0.9$, $\alpha = 8°$ (Sheet 1 of 2)

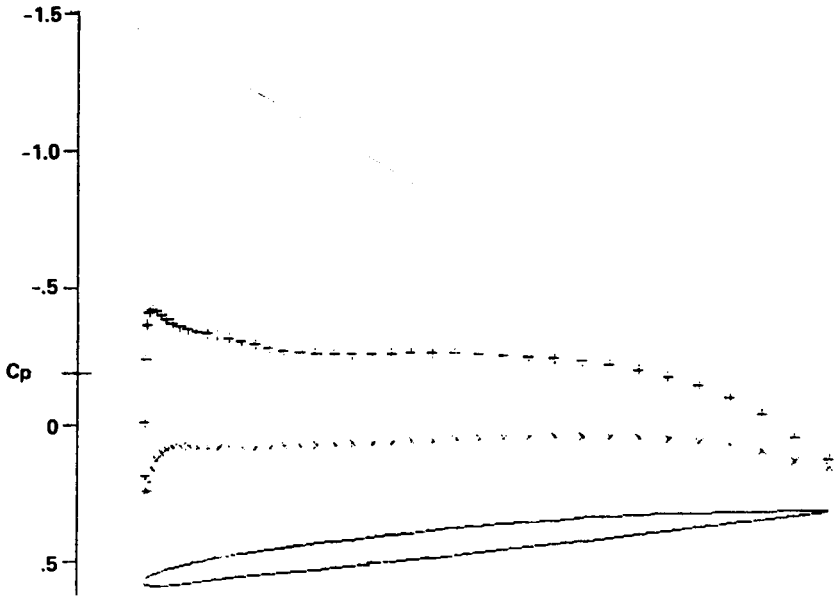

c) Midspan Section

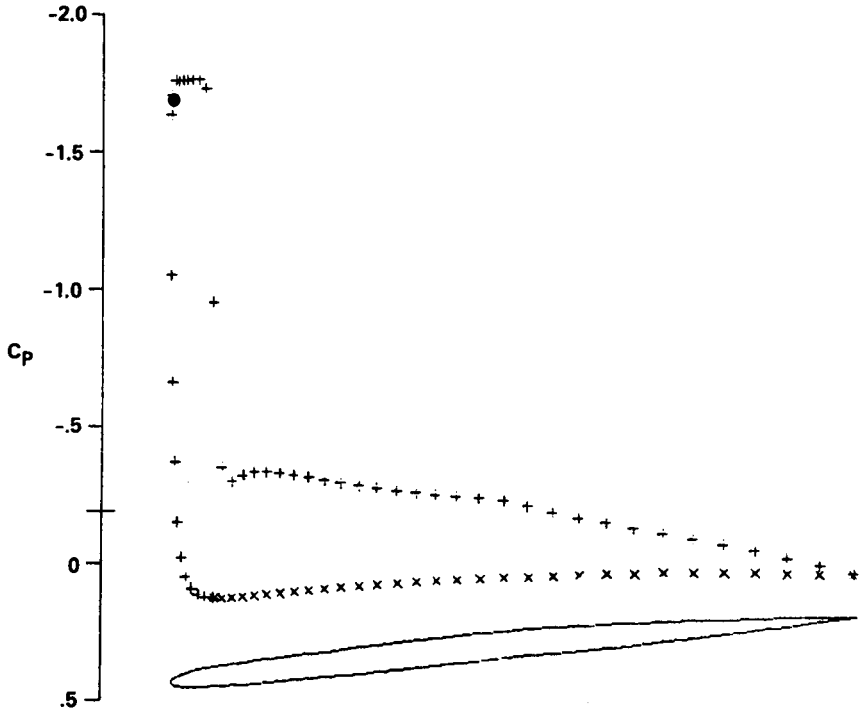

d) Tip Section

Fig. 23 Sample Wing, $M_\infty = 0.9$, $\alpha = 8°$ (Sheet 2 of 2)

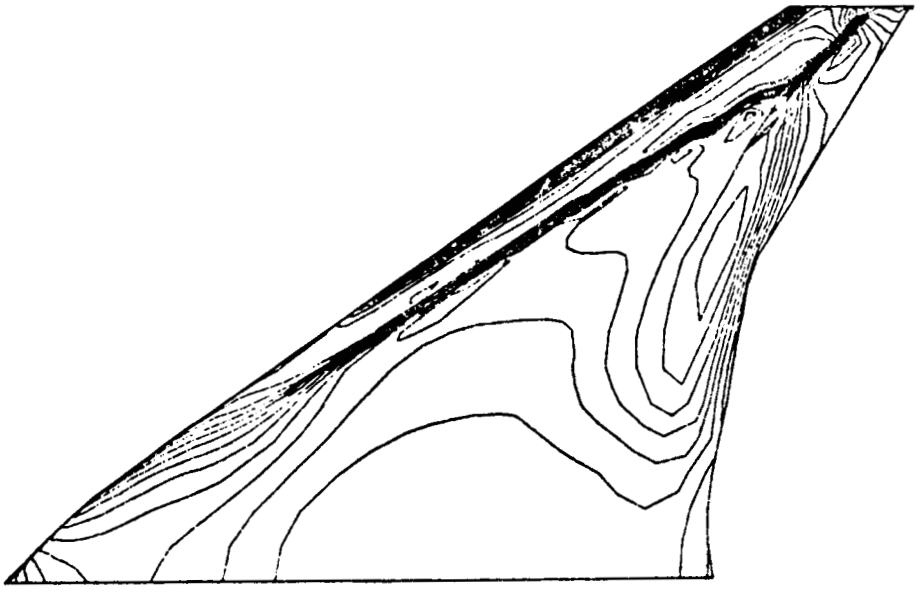

a) Planform & Isobars

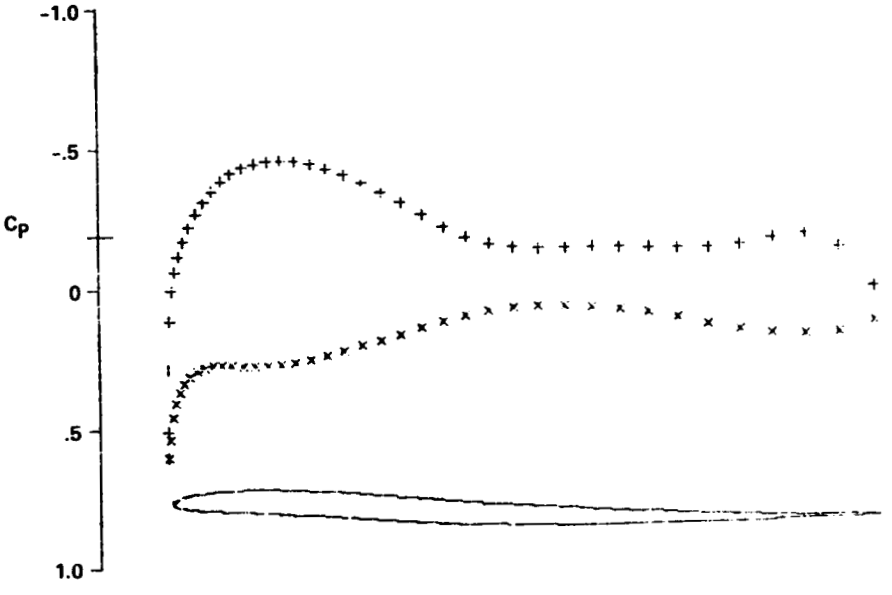

b) Root Section

Fig. 24 Sample Wing 2, M_∞ = 0.9, α = 8° (Sheet 1 of 2)

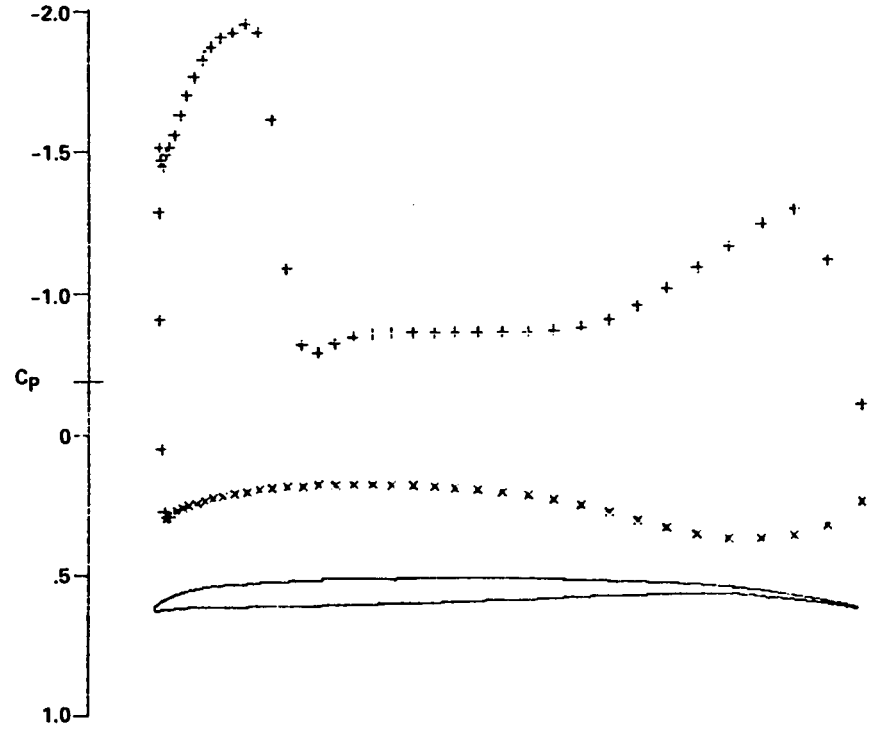

c) Midspan Section

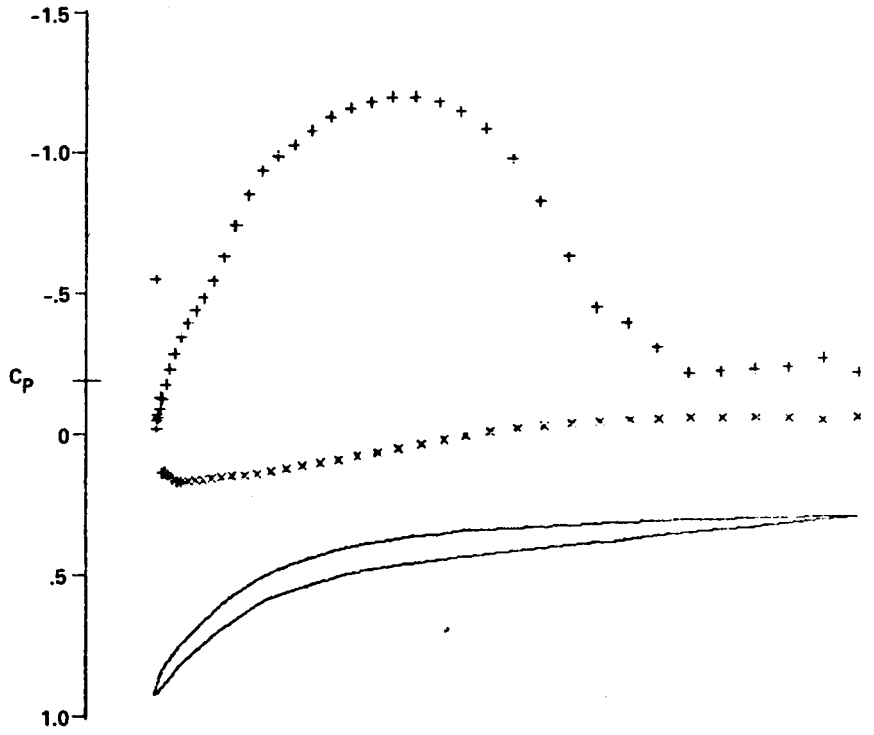

d) Tip Section

Fig. 24 Sample Wing 2, $M_\infty = 0.9$, $\alpha = 8°$ (Sheet 2 of 2)

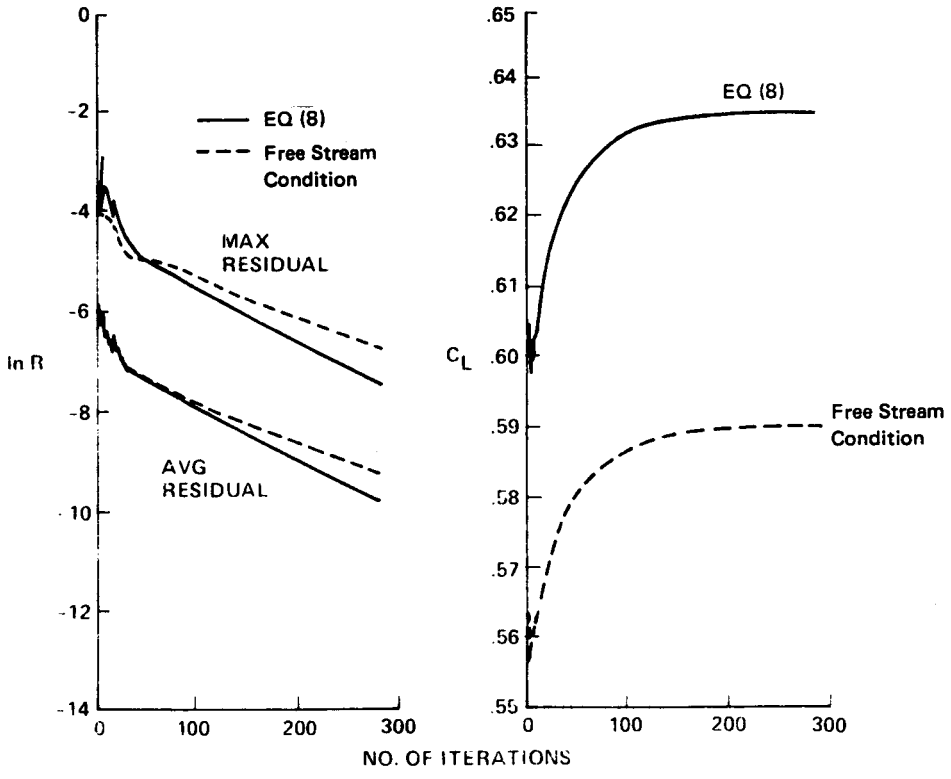

a) Residual b) Lift

Fig. 25 Comparison of Far Field Boundary Conditions Lockheed Wing A, $M_\infty = 0.82$, $\alpha = 1.5°$

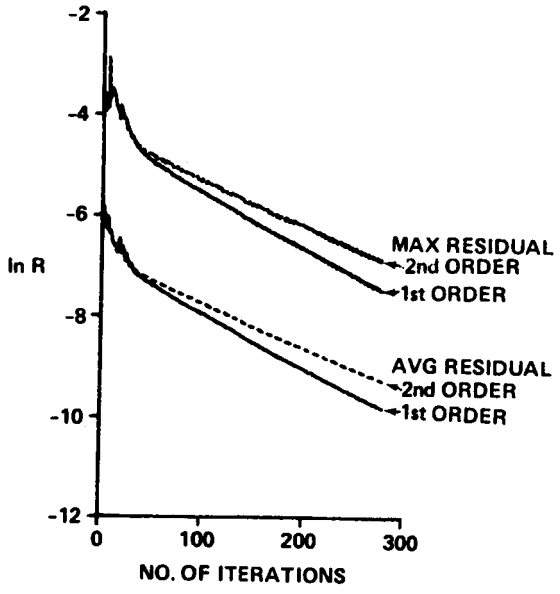

a) Residual

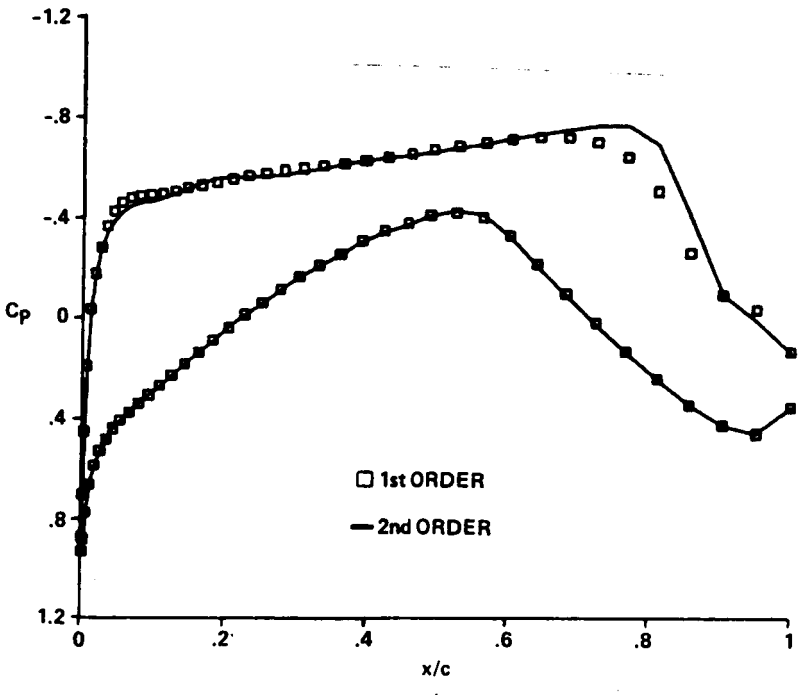

b) Z = 0

Fig. 26 Comparison of 1st and 2nd Order Artificial Viscosity Lockheed Wing A, $M_\infty = 0.82$, $\alpha = 1.5°$ (Sheet 1 of 5)

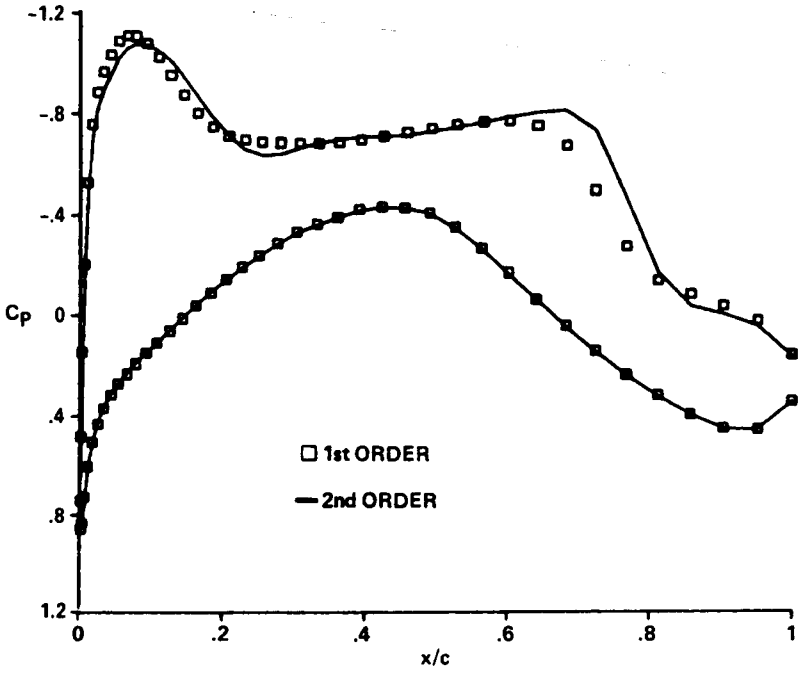

c) Z = 2.25

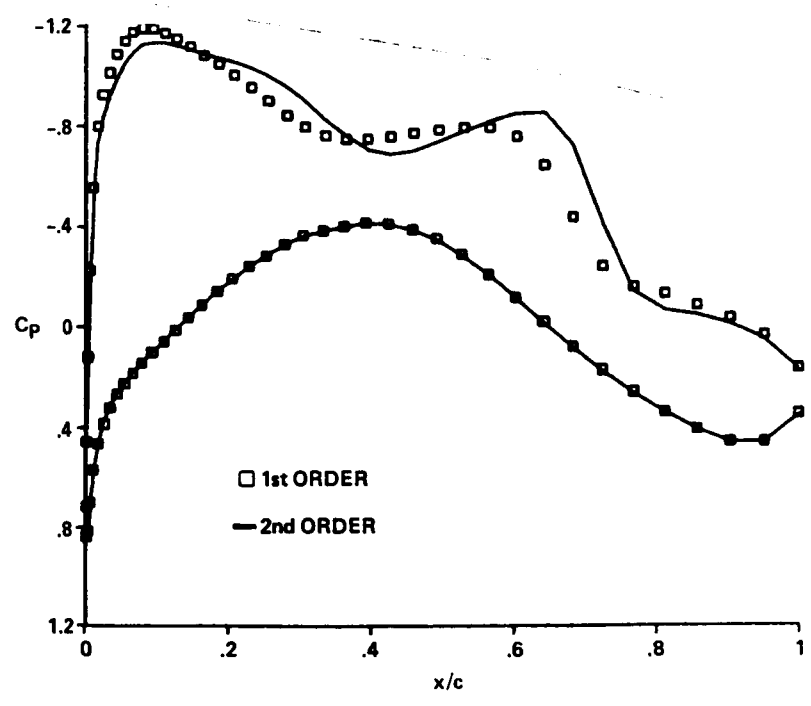

d) Z = 4.5

Fig. 26 Comparison of 1st and 2nd Order Artificial Viscosity Lockheed Wing A, $M_\infty = 0.82$, $\alpha = 1.5°$ (Sheet 2 of 5)

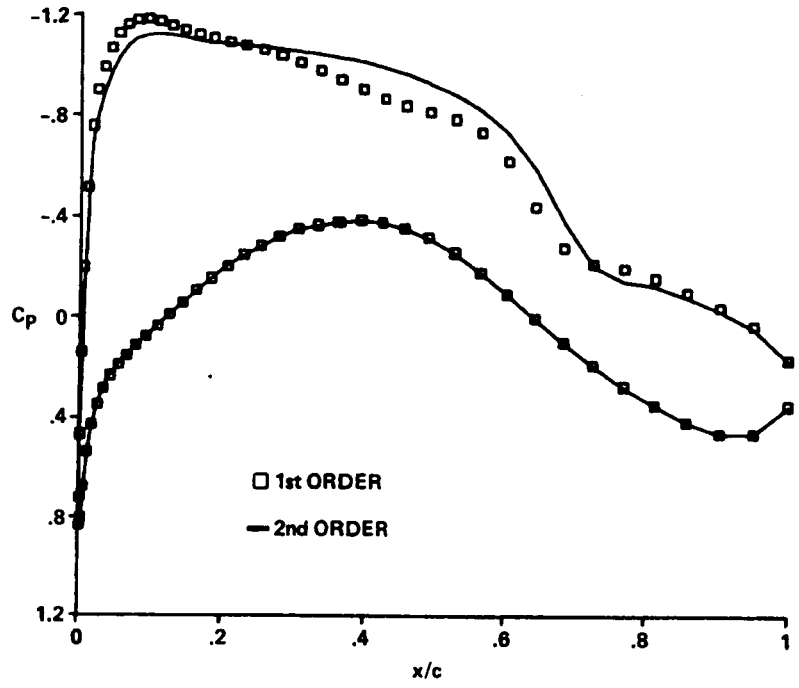

e) Z = 6.75

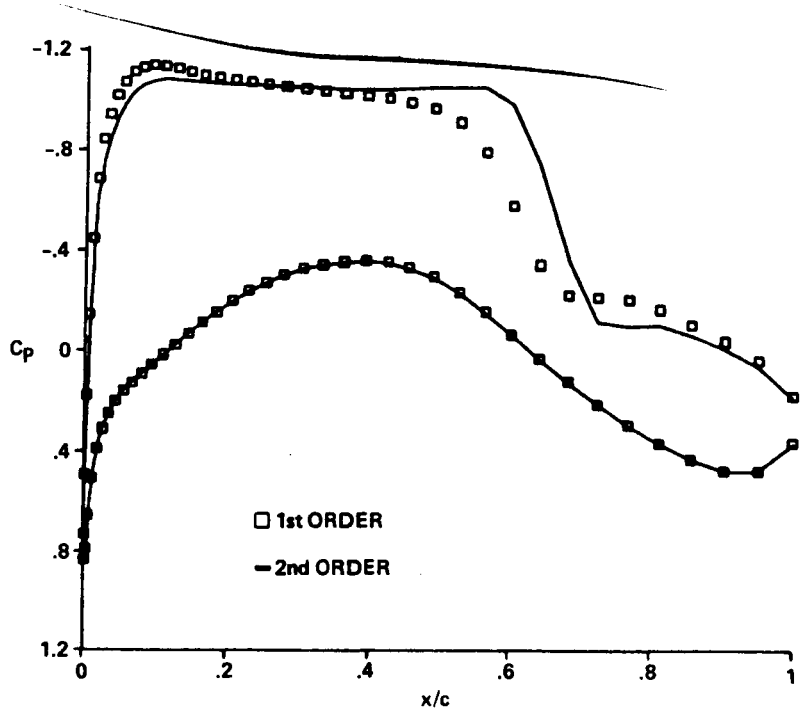

f) Z = 9.0

Fig. 26 Comparison of 1st and 2nd Order Artificial Viscosity Lockheed Wing A, M_∞ = 0.82, α = 1.5° (Sheet 3 of 5)

C-2

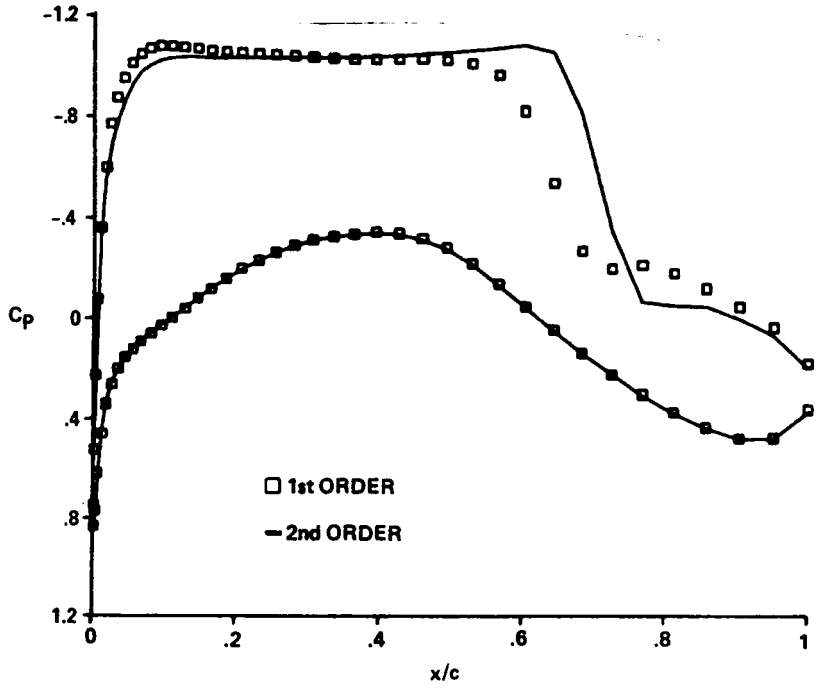

g) Z = 11.25

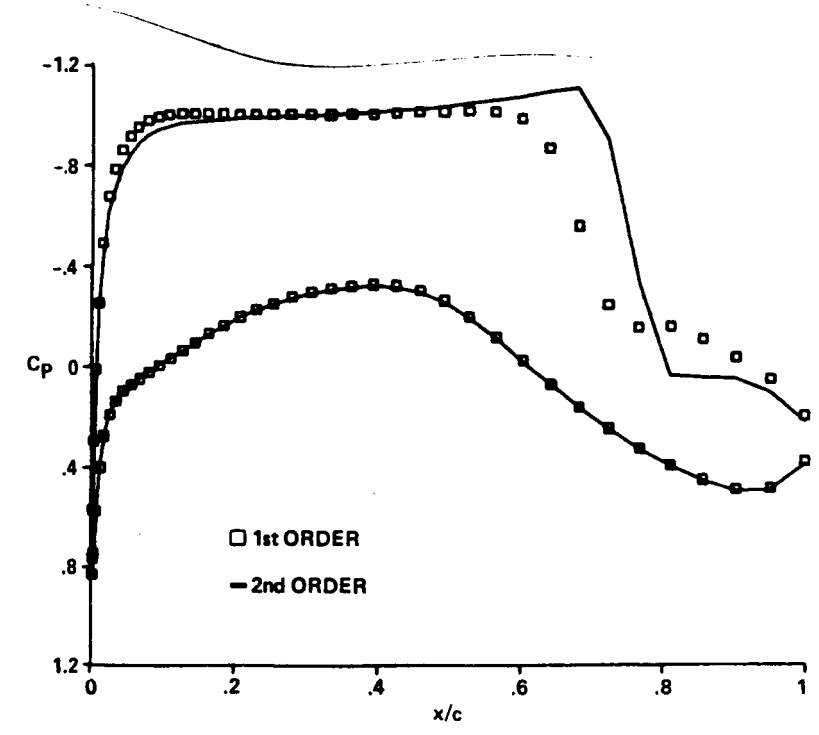

h) Z = 13.5

Fig. 26 Comparison of 1st and 2nd Order Artificial Viscosity Lockheed Wing A, $M_\infty = 0.82$, $\alpha = 1.5°$ (Sheet 4 of 5)

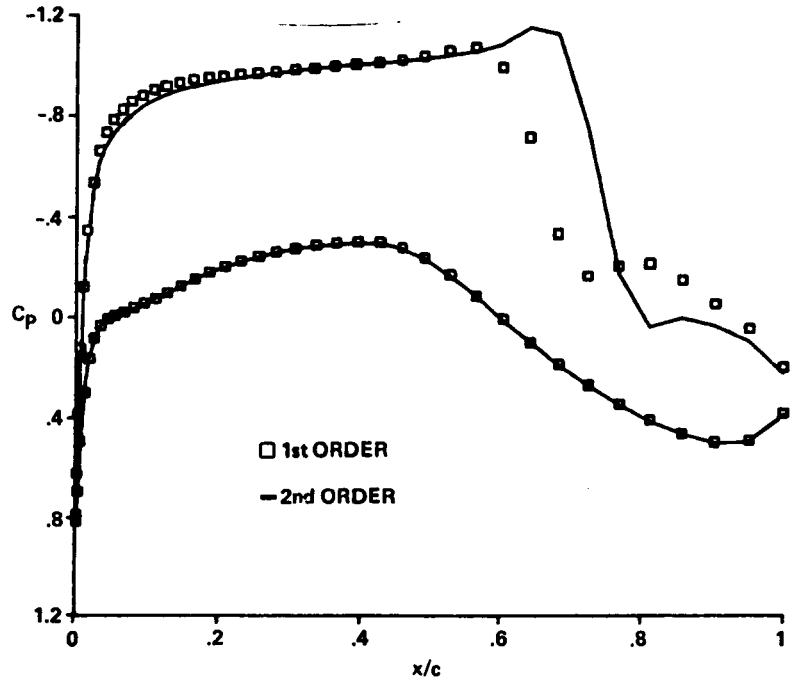

i) Z = 13.75

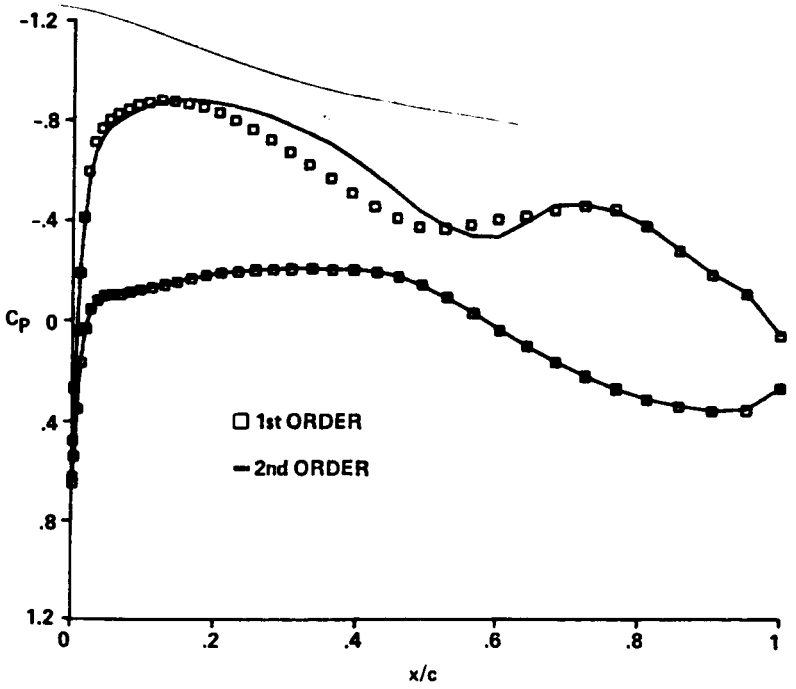

j) Z = 18.0

Fig. 26 Comparison of 1st and 2nd Order Artificial Viscosity Lockheed Wing A, M_∞ = 0.82, α = 1.5° (Sheet 5 of 5)

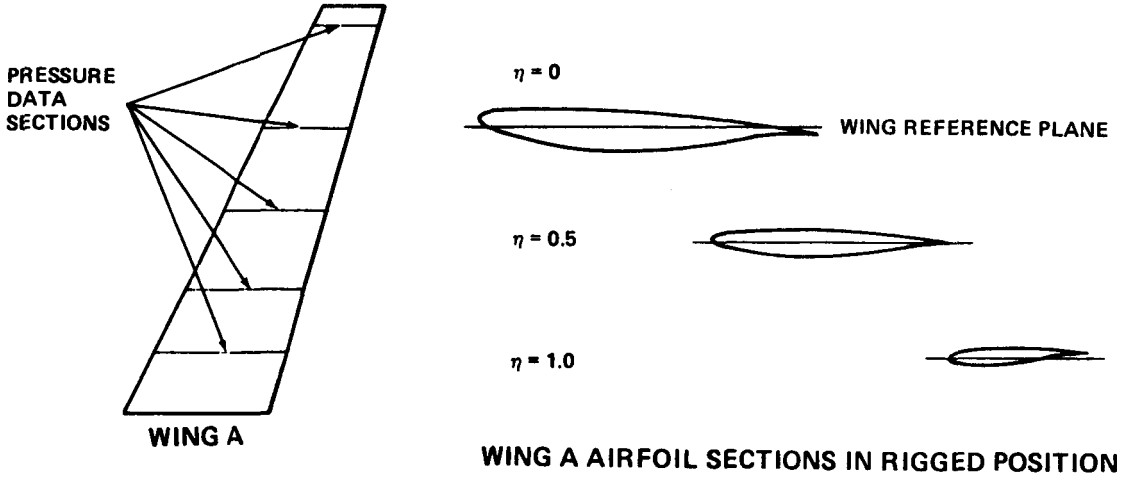

Fig. 27 Lockheed Wing A

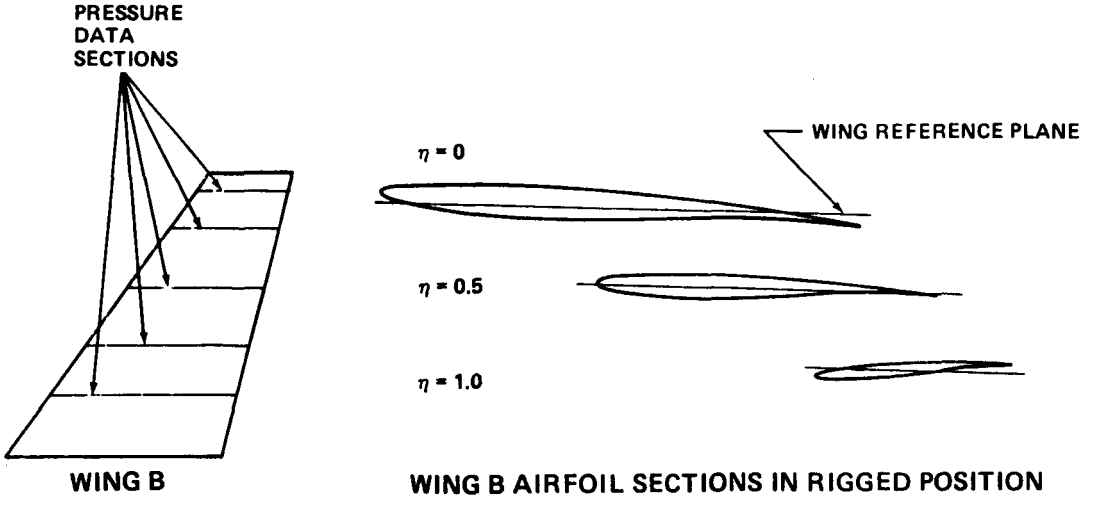

Fig. 28 Lockheed Wing B

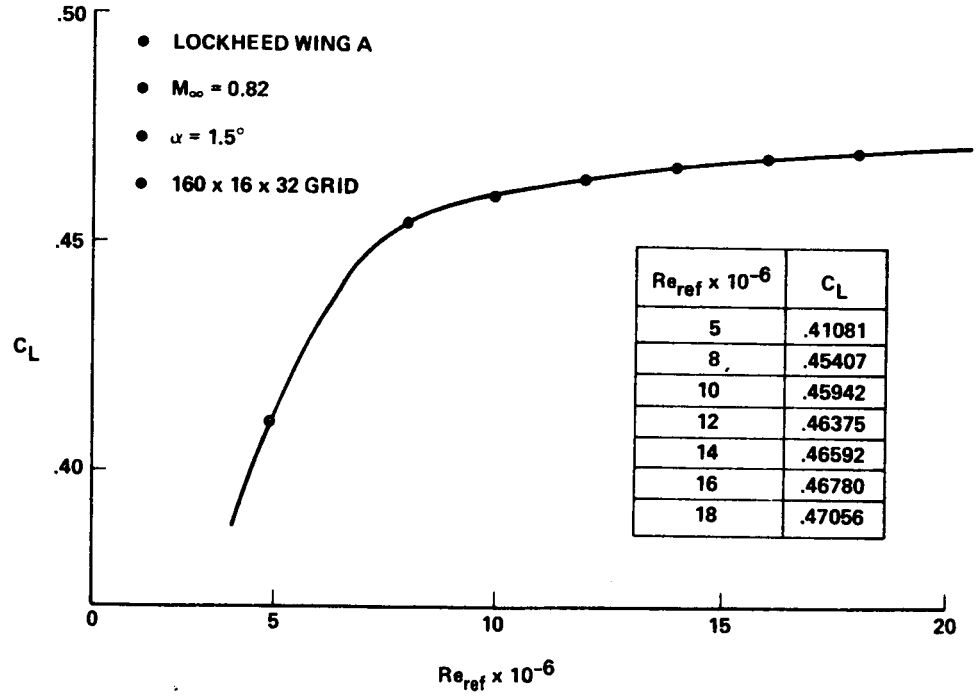

Fig. 29 Reynolds Number Dependence of Viscous Wing Solution

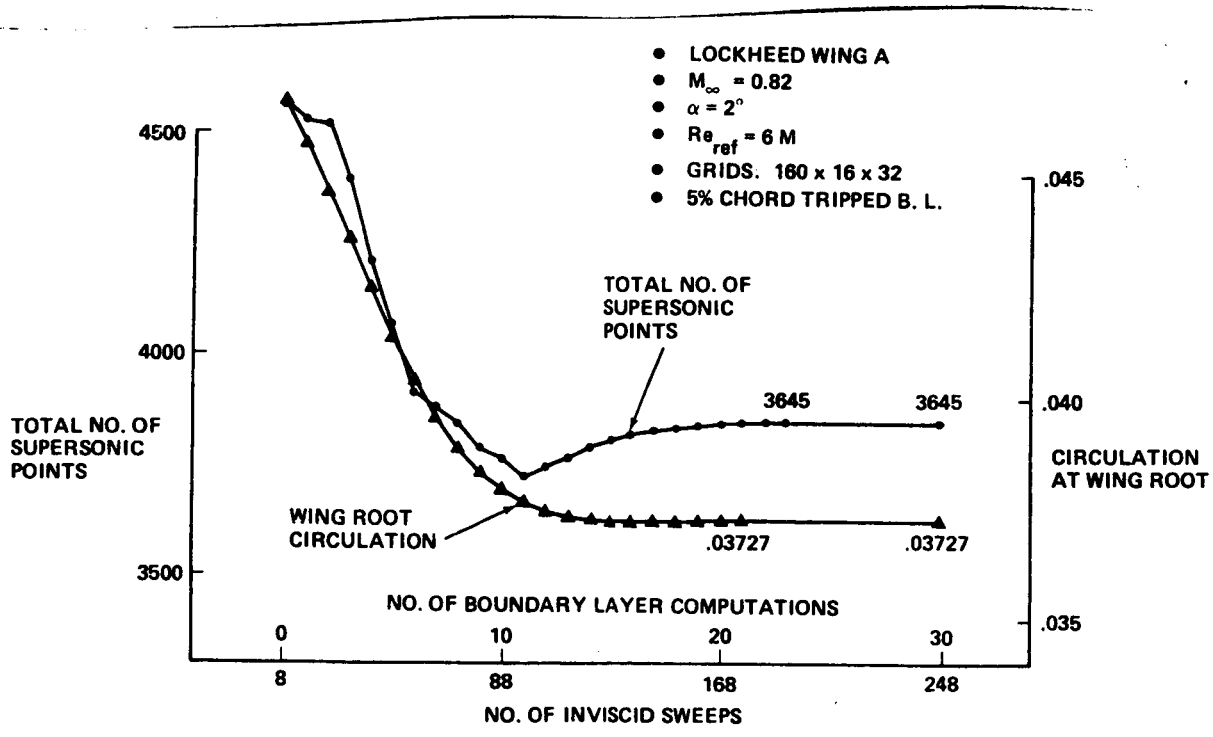

Fig. 30 Convergence History of No. of Supersonic Points & Wing Root Circulation

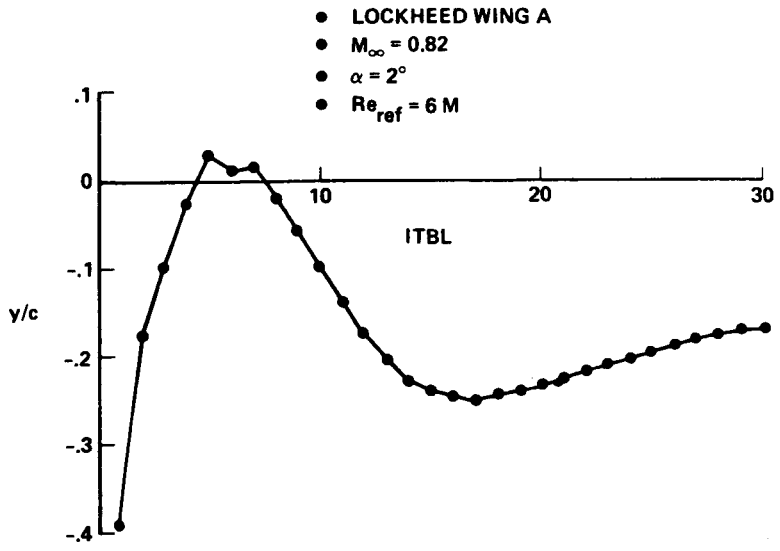

Fig. 31 Convergence History of Last Viscous Floating Wake Point at Wing Root Section

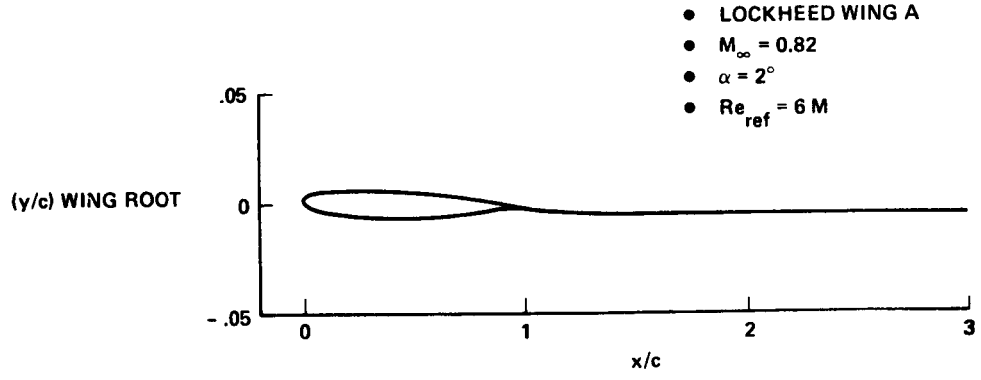

Fig. 32 Converged Floating Wake at Wing Root Section

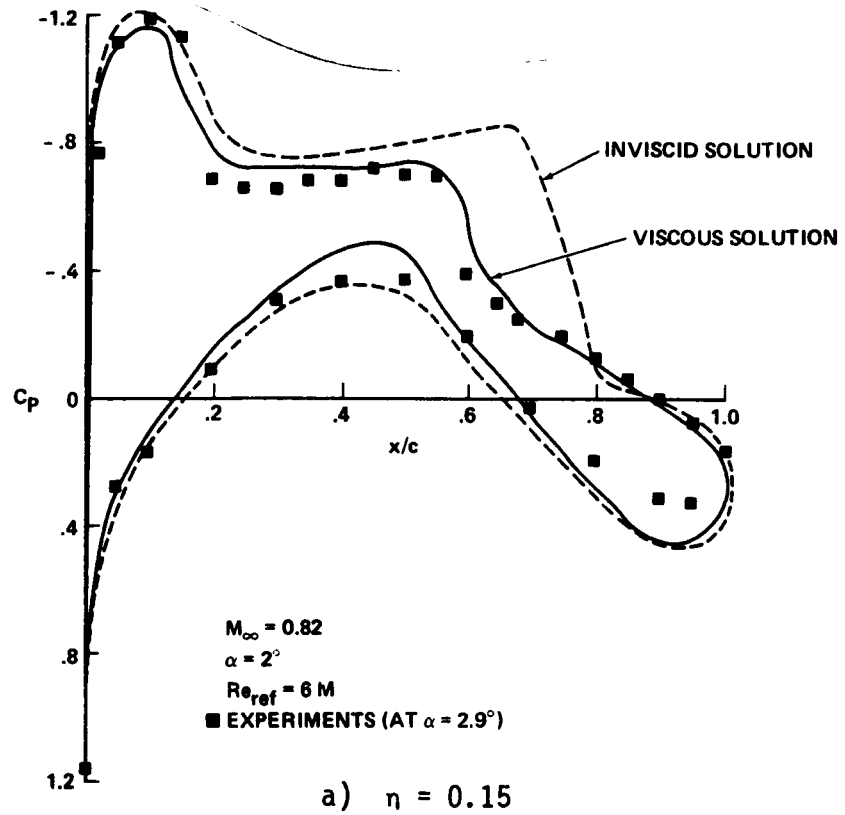

a) η = 0.15

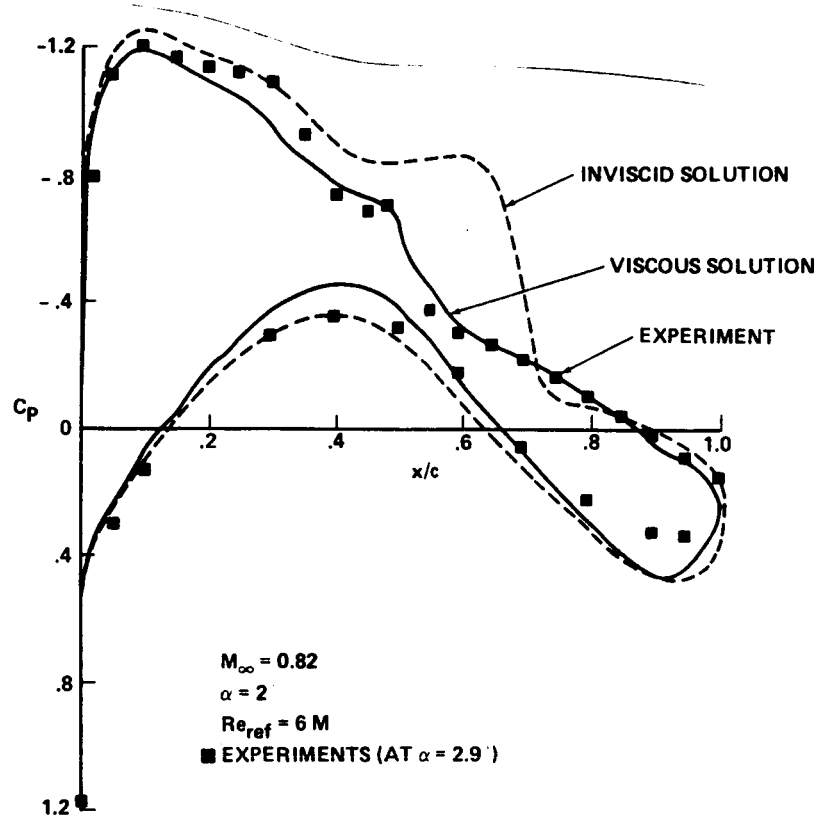

b) η = 0.30

Fig. 33 Comparisons of Sectional Pressure Distributions for Lockheed Wing A (Sheet 1 of 3)

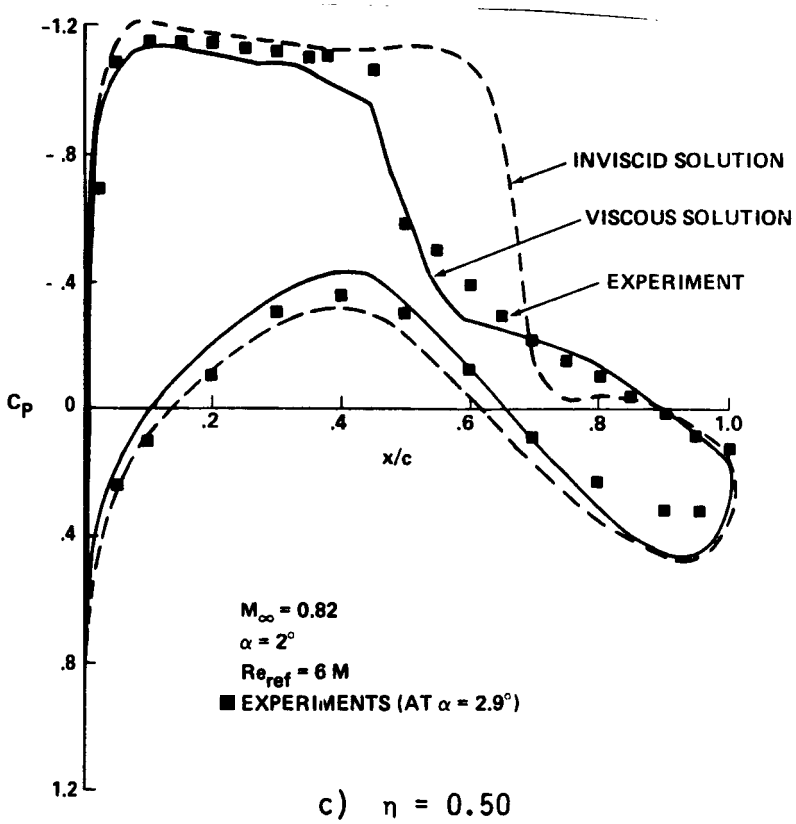

c) η = 0.50

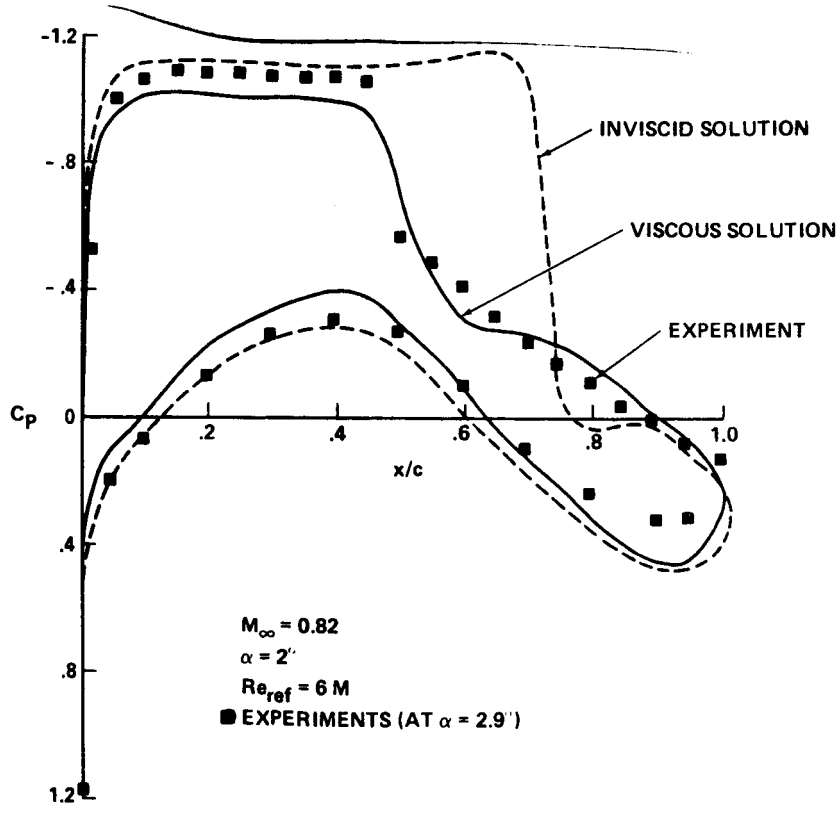

d) η = 0.70

Fig. 33 Comparisons of Sectional Pressure Distributions for Lockheed Wing A (Sheet 2 of 3)

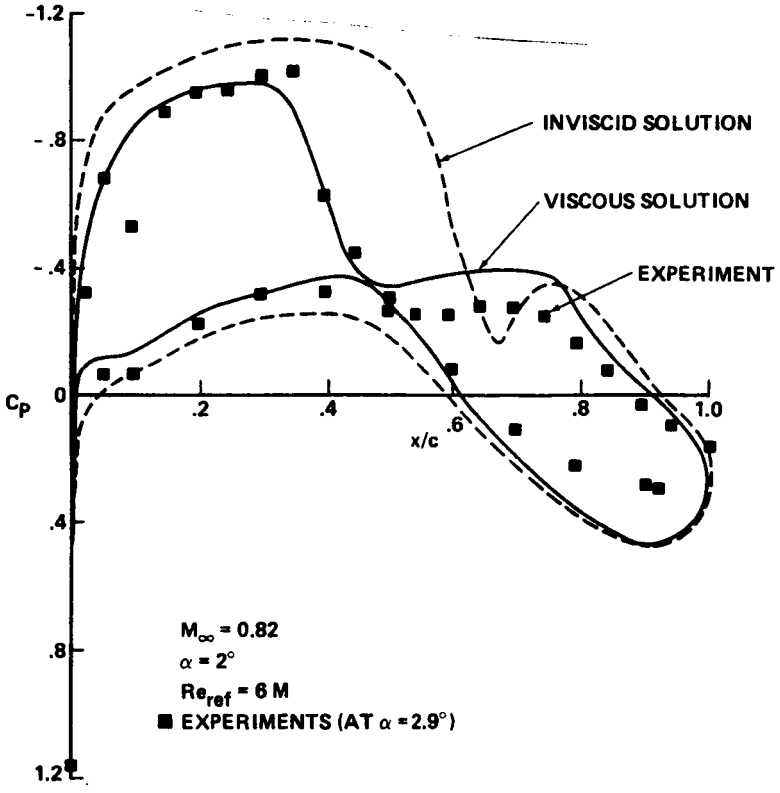

e) $\eta = 0.95$

Fig. 33 Comparisons of Sectional Pressure Distributions for Lockheed Wing A (Sheet 3 of 3)

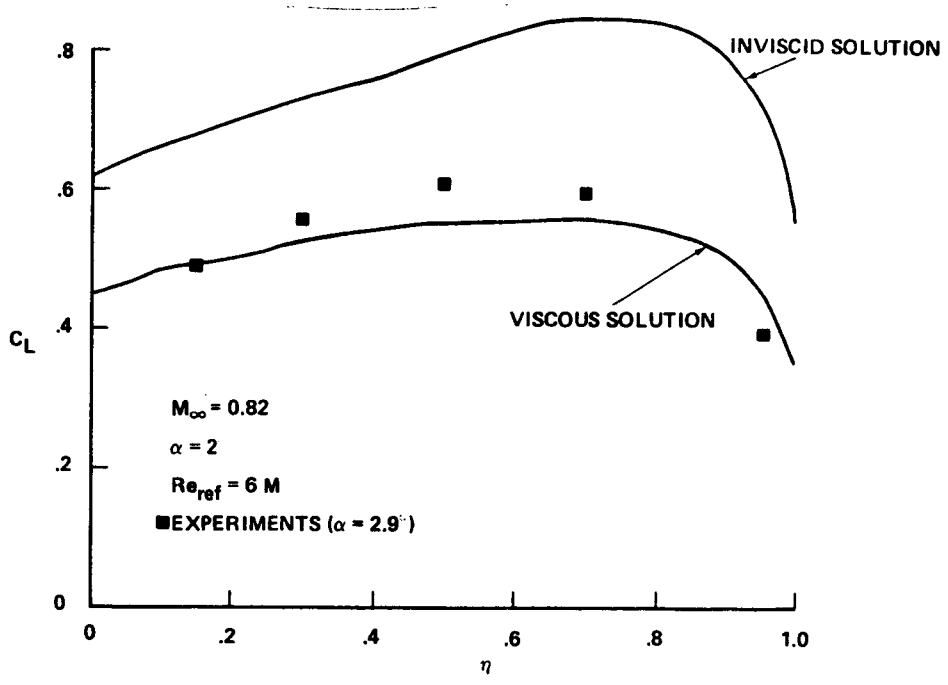

Fig. 34 Comparisons of Span Load Distribution for Lockheed Wing A

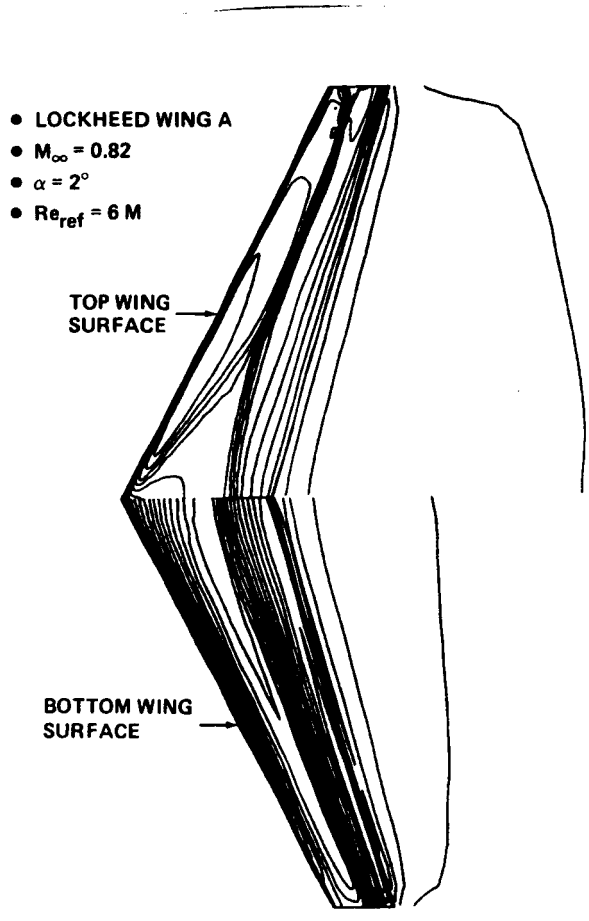

Fig. 35 Converged Viscous Wing Solution - Surface Isobars

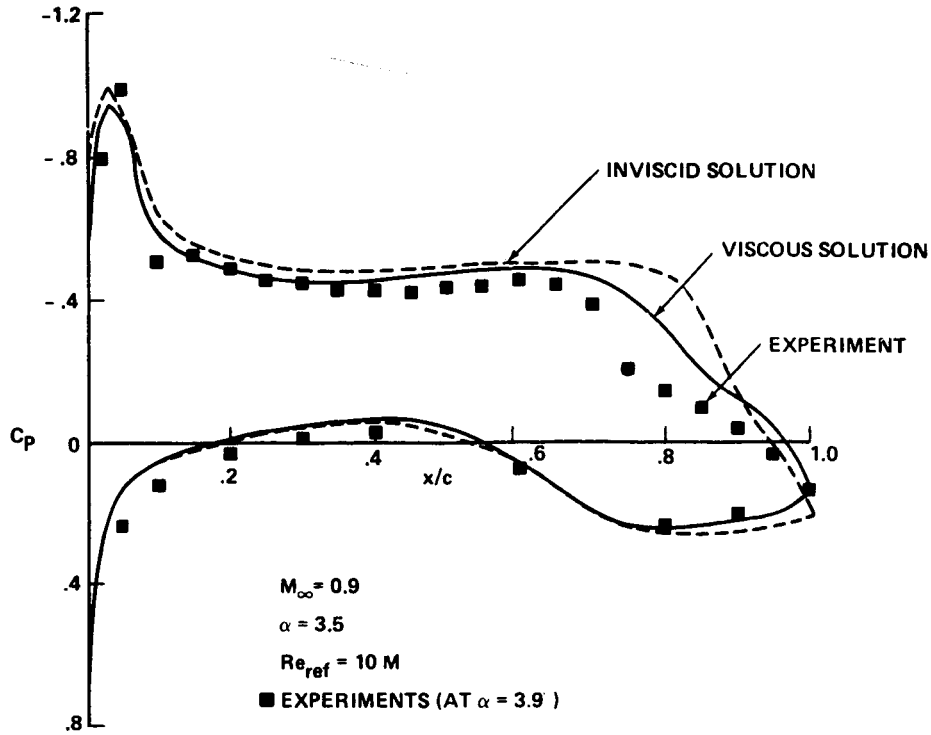

a) η = 0.2 (Theory)
η = 0.22 (Experiments)

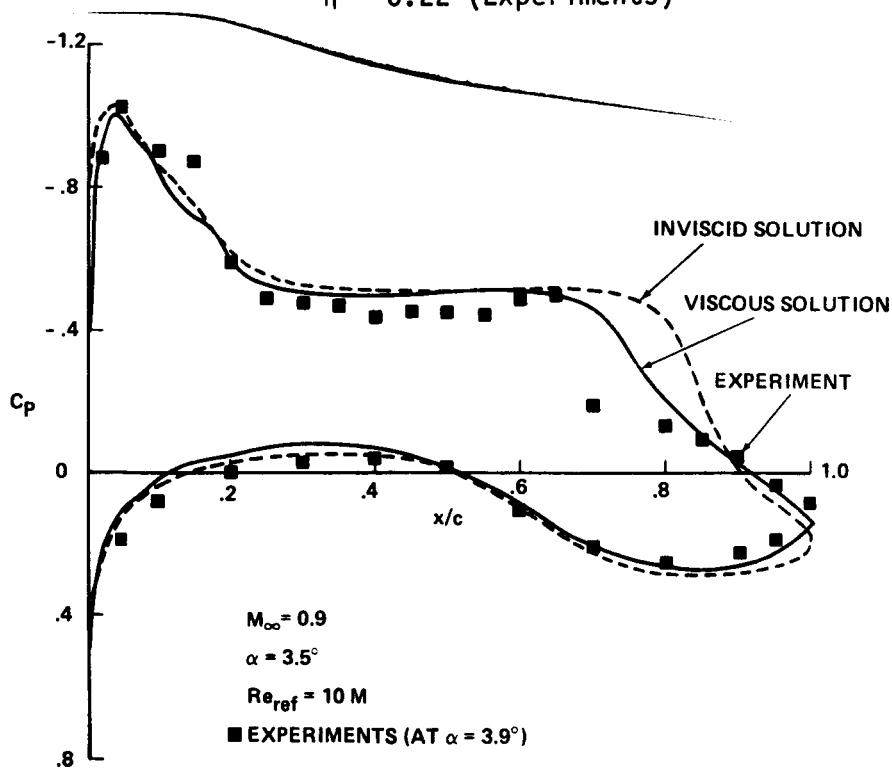

b) η = 0.40

Fig. 36 Comparisons of Sectional Pressure Distributions for Lockheed Wing B (Sheet 1 of 3)

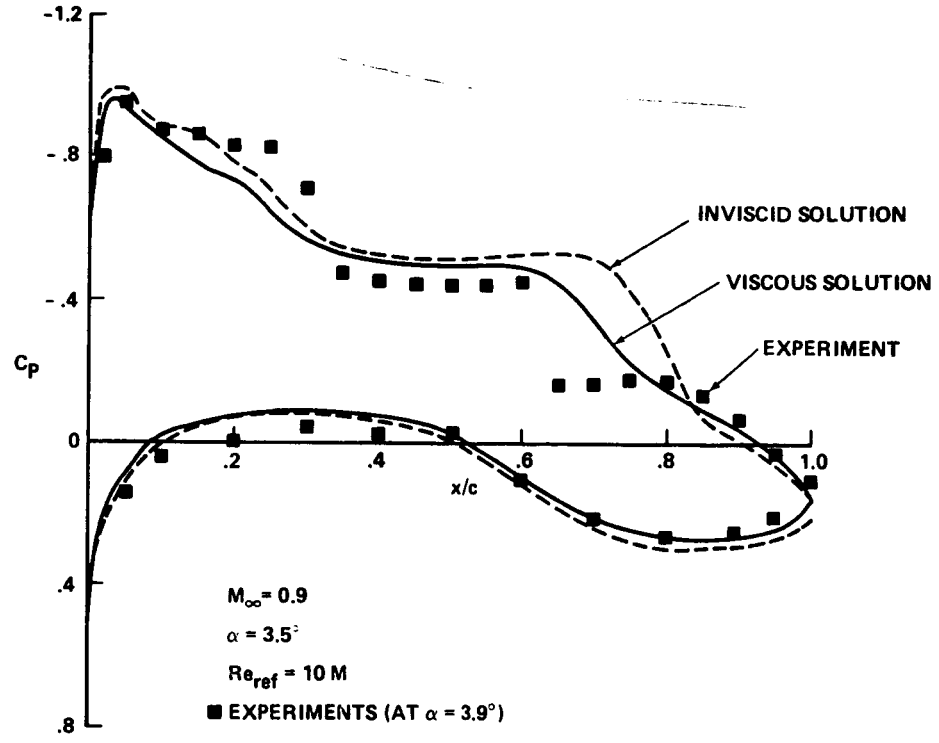

c) η = 0.60

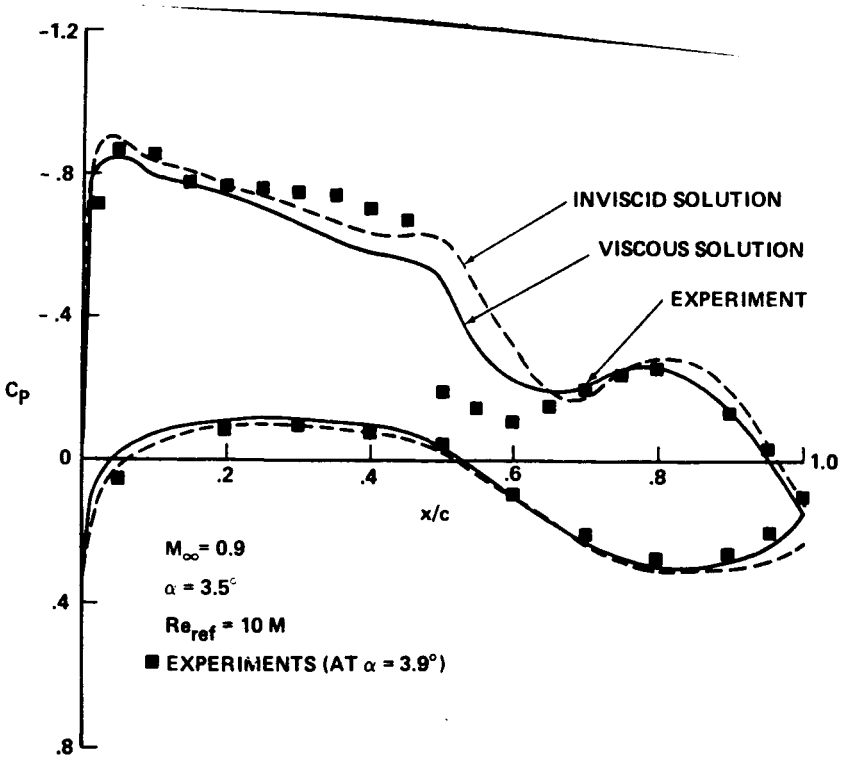

d) η = 0.80

Fig. 36 Comparisons of Sectional Pressure Distributions for Lockheed Wing B (Sheet 2 of 3)

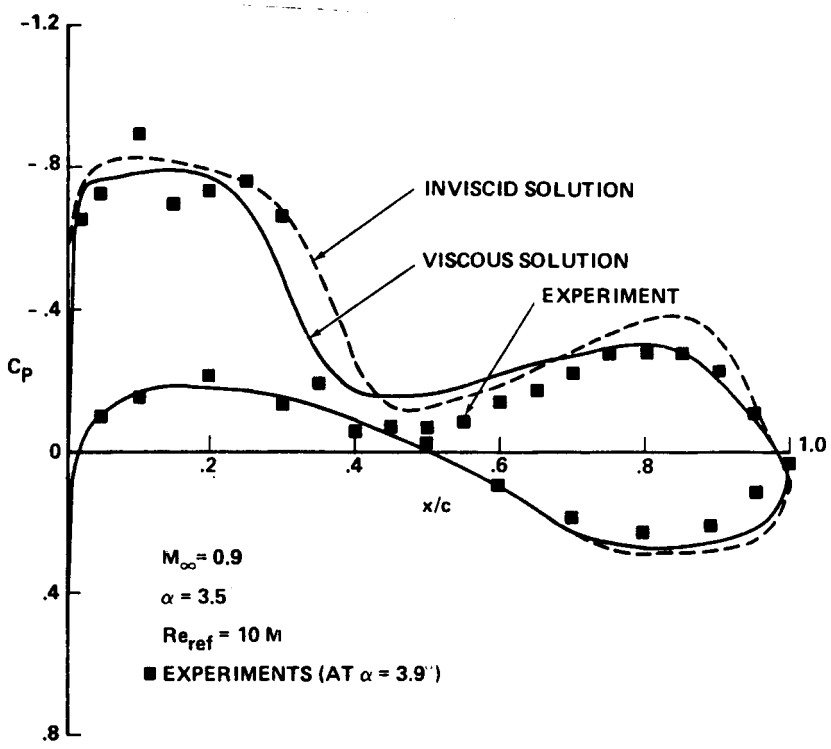

e) η = 0.95

Fig. 36 Comparisons of Sectional Pressure Distributions for Lockheed Wing B (Sheet 3 of 3)

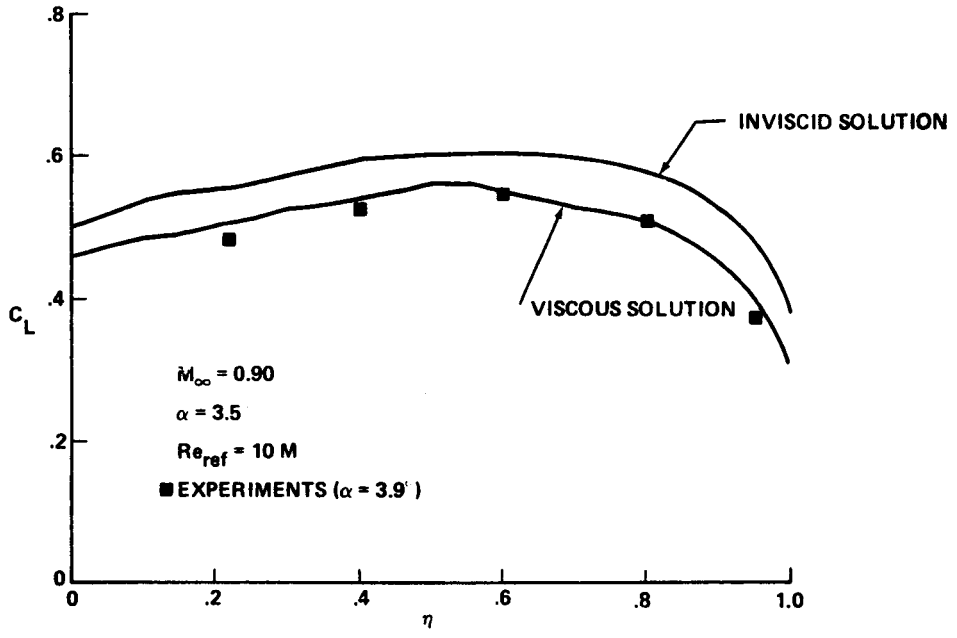

Fig. 37 Comparisons of Span Load Distribution for Lockheed Wing B

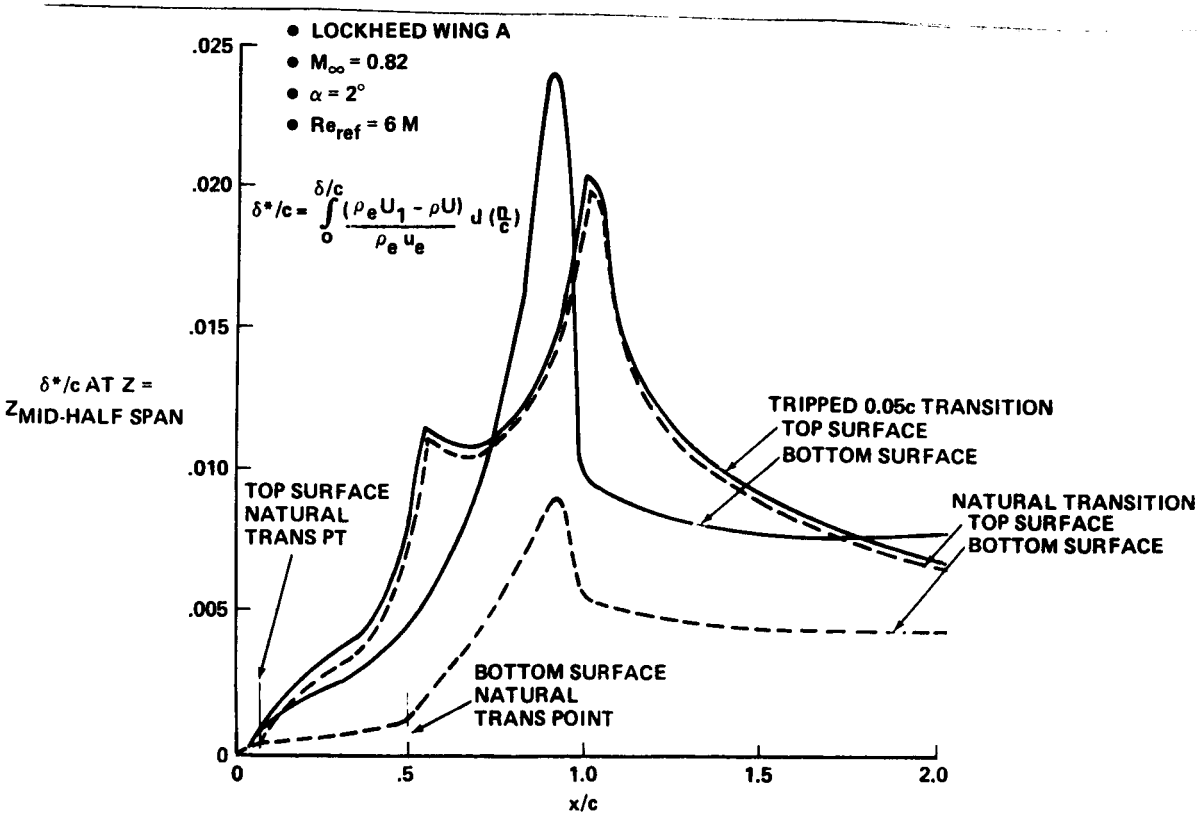

Fig. 38 Displacement Thickness Distribution at Mid-Half-Span Station

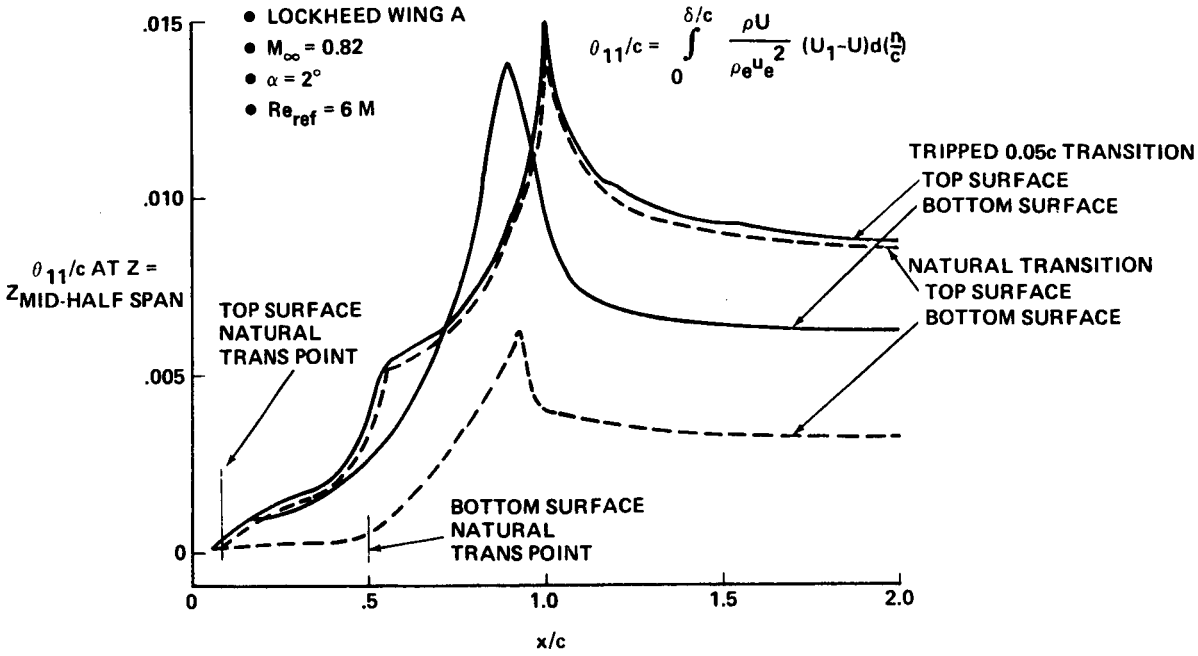

Fig. 39 Momentum Thickness Distribution at Mid-Half-Span Station

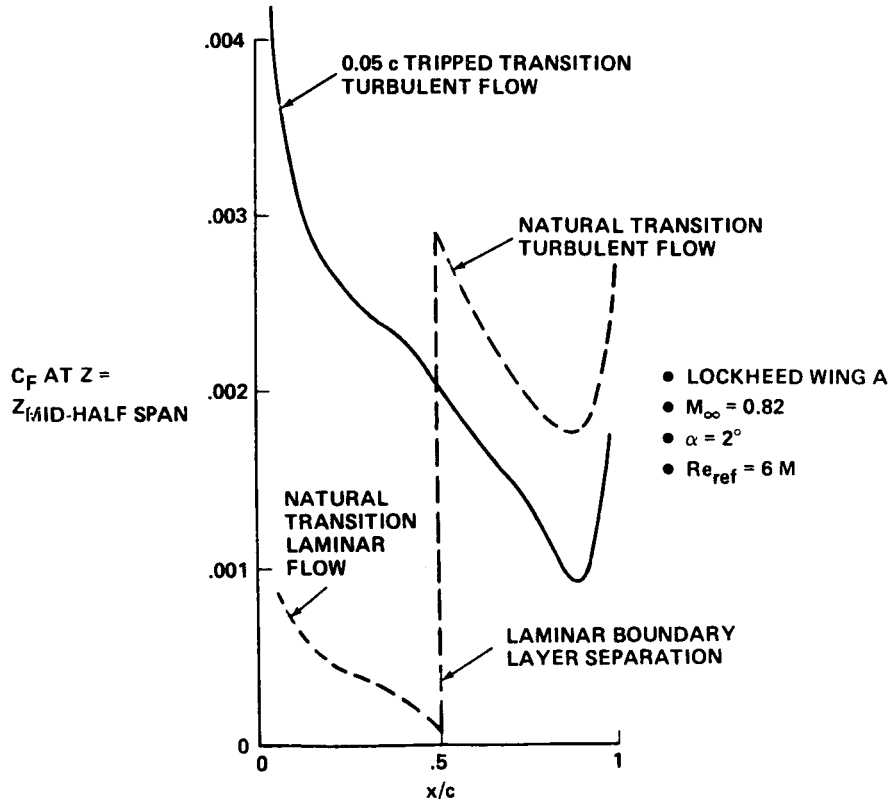

Fig. 40 Lower Wing Surface Skin Friction Distribution at Mid-Half-Span Section

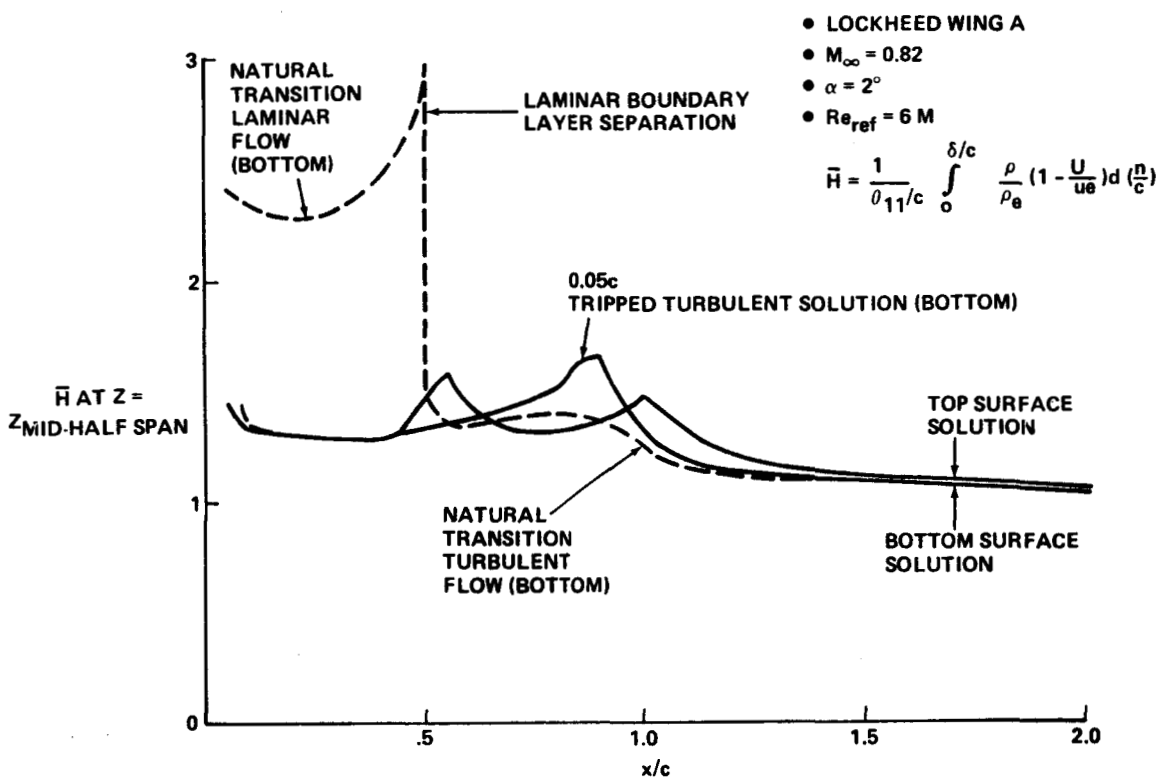

Fig. 41 Shape Factor ($\bar{H}$) Distribution at Mid-Half-Span Section

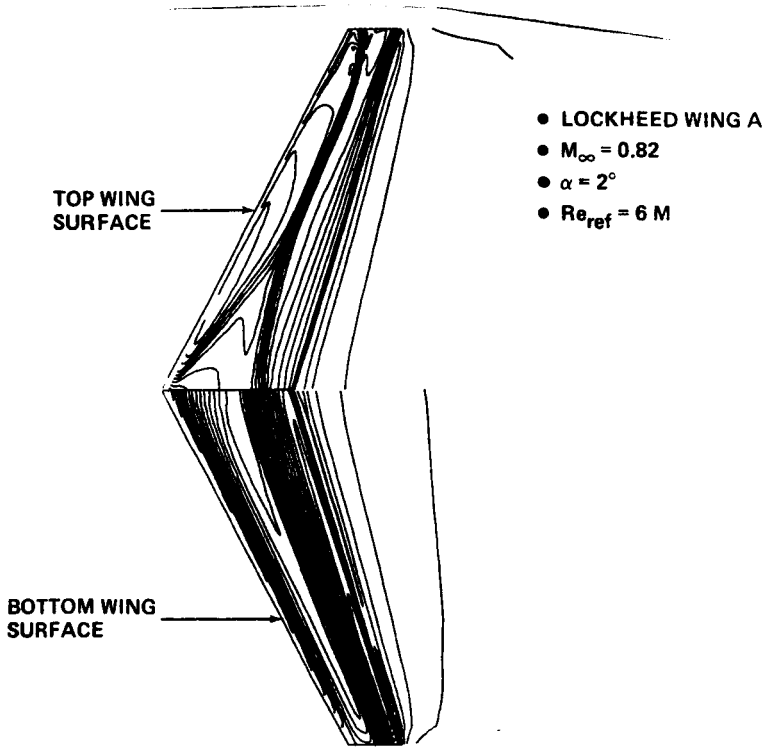

a) Surface Velocity

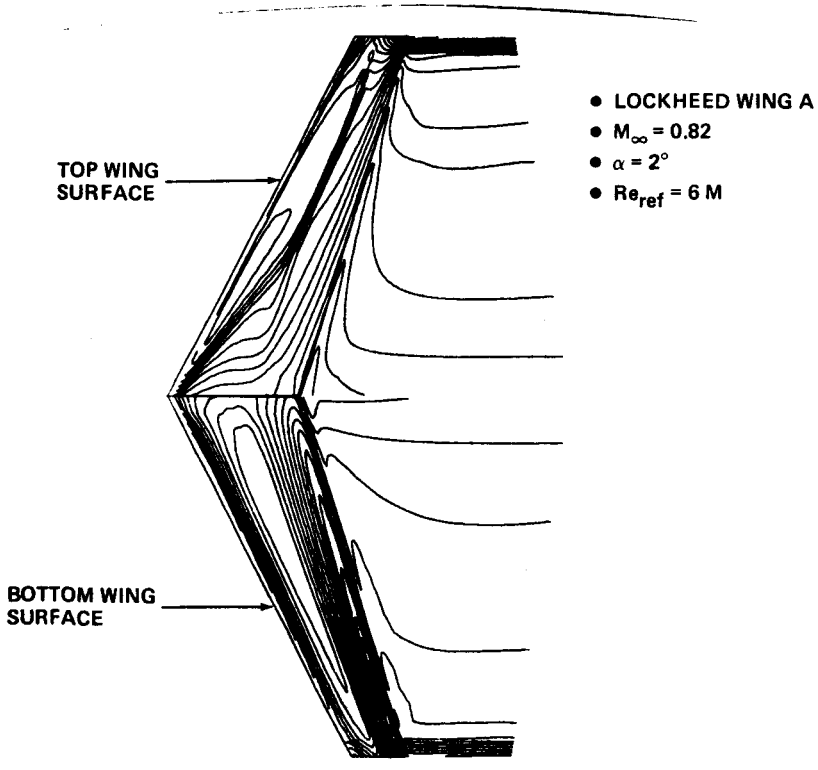

b) Surface Velocity Angle Alpha

Fig. 42 Converged Isoclines for Viscous Wing Solution (Sheet 1 of 3)

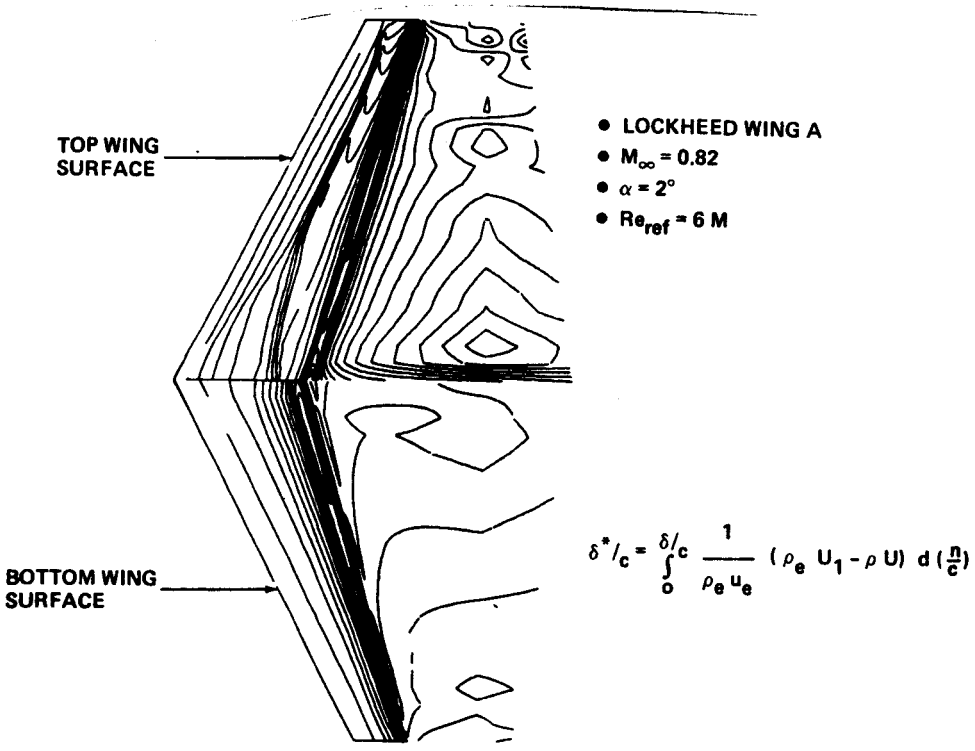

c) Displacement Thickness

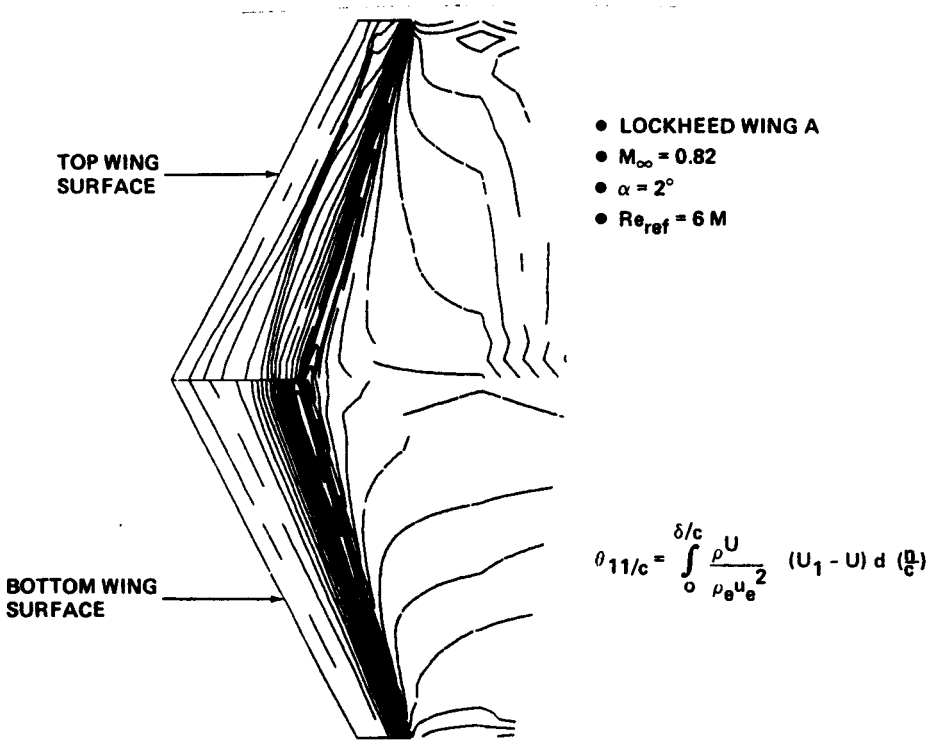

d) Momentum Thickness

Fig. 42 Converged Isoclines for Viscous Wing Solution (Sheet 2 of 3)

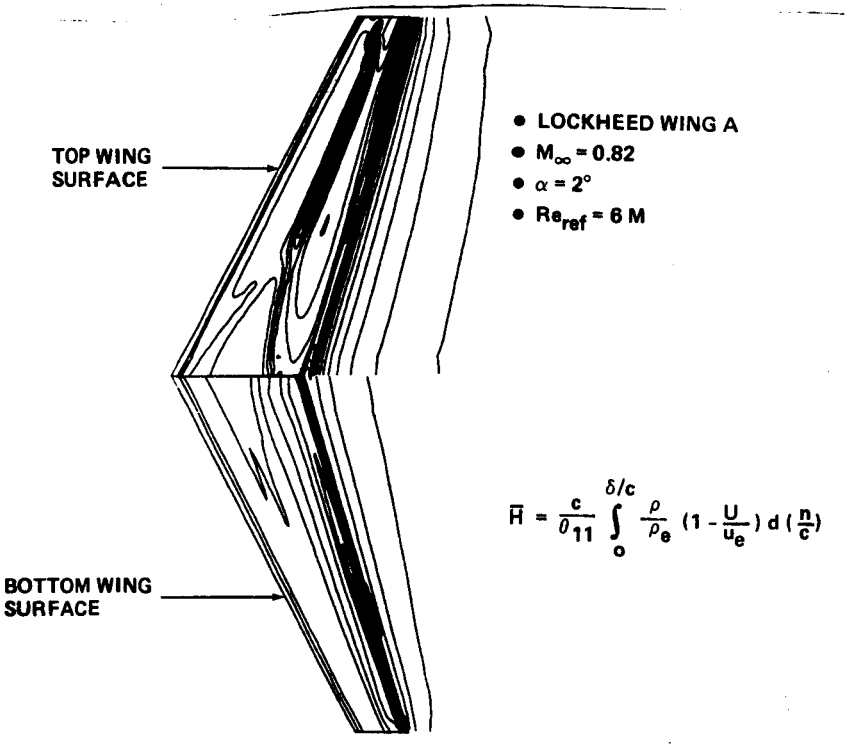

e) Shape Factor

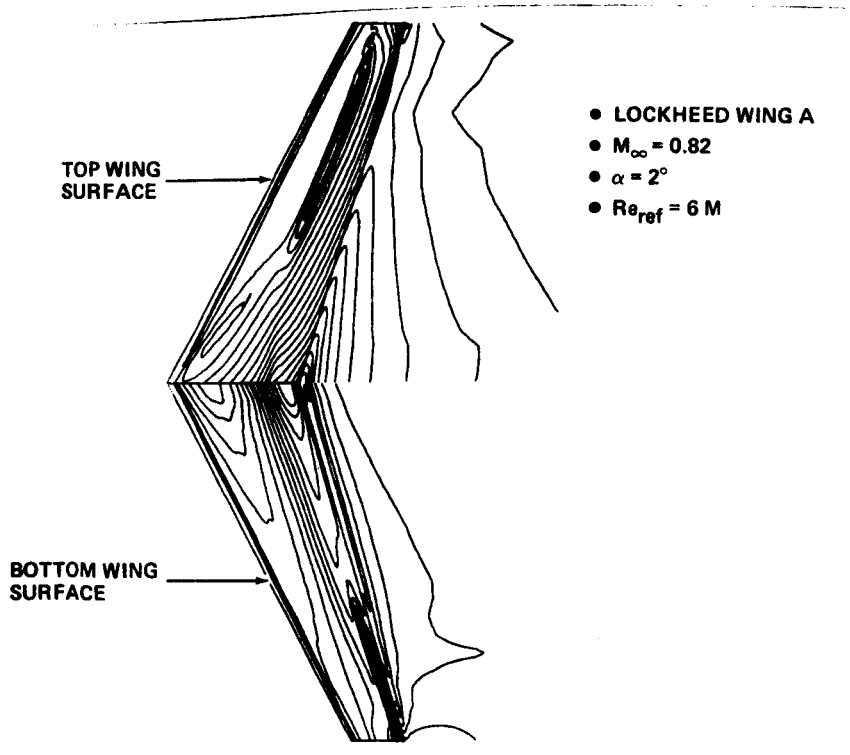

f) Limiting Wall Streamline Angle β

Fig. 42 Converged Isoclines for Viscous Wing Solution (Sheet 3 of 3)

TABLE 1 TRANSITION RUN RESULTS USING LOCKHEED WING A

Assigned Transition Location, % Chord	Actual Transition Location, % Chord		Turbulent Boundary Layer Separation (x) Boundary Layer Iteration									
			6th		7th		8th		9th		10th	
Top & Bottom Surfaces	Top	Bottom	T	B	T	B	T	B	T	B	T	B
0	0	0		x		x		x		x		x
2.5	2.5	2.5		x		x		x		x		x
5.0	5.0	5.0				x		x		x		x
7.5	7.5	7.5				x		x		x		x
10.0	8.2*	10.0						x				x

M_∞ = .82
α = 1°
Re_{ref} = 5 x 10^6
Grid = 160 x 16 x 32

T = Top Wing Surface
B = Bottom Wing Surface
* = Transition Triggered by Laminar Boundary Layer Separation

TABLE 2 TRANSITION RUN RESULTS USING LOCKHEED WING A

Assigned Transition Location, % Chord		Laminar Separation Location, % Chord		Actual Transition Point Location, % Chord		Turbulent Separation		Converged Forces After 20 ITBL	
Top	Bottom	Top	Bottom	Top	Bottom	Top	Bottom	C_L	C_D Pressure Drag
10	20	8.2	NO	8.2	20.0	NO	88.2	0.37323	0.00800
10	40	8.2	NO	8.2	40.0	NO	NO	0.38026	0.00842
10	60	8.2	47.8	8.2	47.8	NO	NO	0.38034	0.00855
10	80	8.2	47.8	8.2	47.8	NO	NO	0.38034	0.00855

$M_\infty = 0.82$ $\alpha = 1°$ $Re_{ref} = 5\ 10^6$ Grid = 160 x 16 x 32

TABLE 3 COMPUTED FORCES RESULTS FOR LOCKHEED WING A

		Assigned Transition		Actual Transition			
	α	Top	Bottom	Top	Bottom	C_L	C_D Pressure Drag
Viscous Run I	2°	0.1C	0.8C	0.081C	0.500C	0.53622	0.01743
Viscous Run II	2°	0.05C	0.05C	0.05C	0.05C	0.52215	0.01647
Inviscid	2°					0.74917	0.02929
Experiment	2.9°			0.05C	0.05C	0.53	

$M_\infty = .82$ $Re_{ref} = 6 \times 10^6$ Grid = 160 x 16 x 32

TABLE 4 COMPUTED FORCES RESULTS FOR LOCKEED WING B

	Section Lift C_L				
	Viscous Solution		Inviscid Solution		Experiment
η	$\alpha = 3°$	3.5°	3°	3.5°	3.9°
0.2	0.4516	0.5024	0.4966	0.5539	0.48 (η =.22)
.4	0.4738	0.5301	0.5252	0.5882	0.52
.6	0.4753	0.5351	0.5339	0.6001	0.55
.8	0.4458	0.5037	0.5116	0.5746	0.51
.95	0.3588	0.4056	0.4229	0.4771	0.38

	WING LOADING			
	C_l		C_D Pressure Drag	
	Viscous	Inviscid	Viscous	Inviscid
$\alpha = 3°$	0.4483	0.5006	0.0190	0.0217
$\alpha = 3.5°$	0.5020	0.5605	0.0242	0.0280
α = 3.9(EXPERIMENT)	0.49		----	

$M_\infty = 0.9$ $Re_{ref} = 10$ M Ak(1) = Ak(2) = 0.05 Grid = 128 x 16 x 32

1. Report No.	2. Government Accession No.	3. Recipient's Catalog No.
NASA CR-178156		

4. Title and Subtitle	5. Report Date
Viscous Wing Theory Development, Volume I - Analysis, Method and Results	October 1986
	6. Performing Organization Code

7. Author(s)	8. Performing Organization Report No.
R.R. Chow, R.E. Melnik, F. Marconi,	RE-725
	10. Work Unit No.

9. Performing Organization Name and Address	11. Contract or Grant No.
Grumman Aerospace Corporation R&D Center, Mail Stop A08-35 Bethpage, New York 11714	NAS1-16858
	13. Type of Report and Period Covered
12. Sponsoring Agency Name and Address National Aeronautics and Space Administration Washington, D.C. 20546	Contractor Report
	14. Sponsoring Agency Code 505-60-01-01

15. Supplementary Notes
Langley Technical Monitor: Craig L. Streett
Final Report

16. Abstract

Viscous transonic flows at large Reynolds numbers over 3-D wings were analyzed using a zonal viscid-inviscid interaction approach. A new numerical AFZ scheme was developed in conunction with the finite volume formulation for the solution of the inviscid full-potential equation. A special far-field asymptotic boundary condition was developed and a second-order artificial viscosity included for an improved inviscid solution methodology. The integral method was used for the laminar/turbulent boundary layer and 3-D viscous wake calculation. The interaction calculation included the coupling conditions of the source flux due to the wing surface boundary layer, the flux jump due to the viscous wake, and the wake curvature effect. A method was also devised incorporating the 2-D trailing edge strong interaction solution for the normal pressure correction near the trailing edge region. A fully automated computer program was developed to perform the proposed method with one scalar version to be used on an IBM-3081 and two vectorized versions on Cray-1 and Cyber-205 computers.

17. Key Words (Suggested by Author(s))	18. Distribution Statement
Viscid/Inviscid Interaction, 3-D Transonic Flow, Wings, Turbulent Flow	Unclassified - Unlimited Subject Category 02

19. Security Classif. (of this report)	20. Security Classif. (of this page)	21. No. of Pages	22. Price
Unclassified	Unclassified	122	